NATIONAL POLAR-ORBITING OPERATIONAL ENVIRONMENTAL SATELLITE SYSTEM (NPOESS)

CLOUD EFFECTIVE PARTICLE SIZE AND CLOUD OPTICAL THICKNESS ALGORITHM THEORETICAL BASIS DOCUMENT (ATBD) (D43750 Rev A)

CDRL No. A032

Northrop Grumman Space & Mission Systems Corporation
One Space Park
Redondo Beach, California 90278

Copyright © 2004-2010
Northrop Grumman Corporation and Raytheon Company
Unpublished Work
ALL RIGHTS RESERVED

This document has been identified per the NPOESS Common Data Format Control Book – External Volume 5 Metadata, D34862-05, Appendix B as a document to be provided to the NOAA Comprehensive Large Array-data Stewardship System (CLASS) via the delivery of NPOESS Document Release Packages to CLASS.

The information provided herein does not contain technical data as defined in the International Traffic in Arms Regulations (ITAR) 22 CFR 120.10.

This document has been approved by the Unites States Government for public release in accordance with NOAA NPOESS Integrated Program Office.

Distribution: Statement A: Approved for public release; distribution is unlimited.

NATIONAL POLAR-ORBITING OPERATIONAL ENVIRONMENTAL SATELLITE SYSTEM (NPOESS)

CLOUD EFFECTIVE PARTICLE SIZE AND CLOUD OPTICAL THICKNESS ALGORITHM THEORETICAL BASIS DOCUMENT (ATBD) (D43750 Rev A)

ELECTRONIC APPROVAL SIGNATURES:

_____
Roy Tsugawa   Date
Algorithm & Data Processing IPT Lead &
Algorithm Change Control Board Chairperson

_____
Ben James   Date
Operations & Support IPT Lead

The following individuals are recognized for their contributions to the current or previous versions of this document.

    Glenn J. Higgins
    Kuo-Nan Liou
    Szu-Cheng Ou
    Richard L. Slonaker
    Yoshihide Takano
    Eric Wong

	NP ESS Northrop Grumman Raytheon DOC • DoD NASA		
Revision/Change Record		**Document Number**	D43750

Revision	Document Date	Revision/Change Description	Pages Affected
---	1/23/2007	Initial PCIM Release to bring document into Matrix Accountability. Reference original document number: Y2393 delivered in 2006	All
A	7/24 /2008	Delete MTF statements per SPCR ALG 1314	91 and 117
		Incorporated ECR A-163. Approved for Public Release per Contracts Letter 100610-02.	

TABLE OF CONTENTS

LIST OF FIGURES

LIST OF TABLES

GLOSSARY OF ACRONYMS

ARM	Atmospheric Radiation Measurement
ATBD	Algorithm Theoretical Basis Document
AVHRR	Advanced Very-High-Resolution Radiometer
BBR	Band-to-Band Registration
CBH	Cloud Base Height
CCL	Cloud Cover/Layers
Ci	Cirrus
CKD	Correlated K-Distribution
CLASS	Cross-chain LORAN Atmospheric Sounding System
COT	Cloud Optical Thickness
COP	Cloud Optical Properties
Cs	Cirrostratus
CSSM	Cloud Scene Simulation Model
CTH	Cloud Top Height
CTP	Cloud Top Parameters
CTT	Cloud Top Temperature
DAAC	Distributed Active Archive Center
DISORT	Discrete Ordinate Radiative Transfer Model
DMSP	Defense Meteorological Satellite Program
DOC	Department of Commerce
DoD	Department of Defense
EB	Error Budget
EDR	Environmental Data Record
EOS	Earth Observation System
EPS	Effective Particle Size
FASCOD	Fast Atmosphere Signature Code
FDTD	Finite-Difference Time Domain Method
FIRE	First ISCCP Regional Experiment
GOM2	Geometric-Optics/integral-equation hybrid Method
HCS	Horizontal Cell Size
HITRAN	High-Resolution Transmission Molecular Absorption Database
IFO	Intensive Field Observation
IOP	Intensive Observation Period

IP	Intermediate Product
IPT	Integrated Project Team
IR	Infrared
ISCCP	International Satellite Cloud Climatology Project
ITSS	Raytheon-Information Technology and Scientific Services
IWC	Ice Water Content
LBLE	Line-by-Line Equivalent Radiative Transfer Model
LOWTRAN	Low-Resolution Transmission Model
LUT	Look-Up Table
MAS	MODIS Airborne Simulator
MCR	Multi-spectral Cloud Radiometer
MD	MODTRAN-DISORT program
MODIS	Moderate Resolution Imaging Spectroradiometer
MODTRAN	Moderate-Resolution Atmospheric Transmittance and Radiance Model
MTF	Modulation Transfer Function
NCAR	National Center for Atmospheric Research
NOAA	National Oceanic and Atmospheric Administration
NPOESS	National Polar-orbiting Operational Environmental Satellite System
POES	Polar-orbiting Operational Environmental Satellite
RMS	Root Mean Square
SDR	Sensor Data Record
SGP	Southern Great Plains
SNR	Signal-to-Noise Ratio
SRD	Sensor Requirements Document
SUCCESS	Subsonic Aircraft Contrail and Cloud Effects Special Study
TASC	The Atmospheric Sciences Corporation
TBD	To Be Determined
TBR	To Be Resolved
TOA	Top Of Atmosphere
UCLA	University of California at Los Angeles
VIIRS	Visible/Infrared Imager/Radiometer Suite

ABSTRACT

This Algorithm Theoretical Basis Document (ATBD) describes the algorithms for retrieving the Cloud Optical Thickness (COT) and Effective Particle Size (EPS) using the Visible/Infrared Imager/Radiometer Suite (VIIRS) channel brightness temperatures and reflectances. Input parameters required by the algorithms also include other VIIRS derived quantities (cloud mask, surface albedo and surface type) and scenario parameters (e.g., sun-sensor geometry). The overall processing begins with the identification of cloud-contaminated pixels and the determination of the cloud phase associated with the cloudy pixel via the VIIRS cloud mask/phase program. Four basic retrieval techniques are developed: solar and infrared (IR) for both cirrus and water clouds. The solar approach uses the reflectance of VIIRS 0.672, 1.24 and 1.61μm channels and follows the two-channel correlation technique (Nakajima and King, 1990) to retrieve the COT and EPS during daytime. The IR approach utilizes the radiance of VIIRS 3.7, 8.55 10.7625μm, and 12.013 m channels and follows the two-channel cirrus technique (Ou *et al.* 1993) to infer the cloud top temperature and IR emissivity. The COT and EPS can then be determined on the basis of the theory and parameterizations of radiative transfer and cloud microphysics. A neighboring-scene technique and a smoothing routine have been added to determine clear radiances for overcast scenes. To carry out the algorithm sensitivity studies, we use a line-by-line equivalent (LBLE) radiative transfer model developed at the University of California at Los Angeles (UCLA) to generate radiance tables for various combinations of COT and EPS. Algorithm sensitivity studies are composed of signal-to-noise ratio (SNR) tests as well as the error budget (EB) studies. The SNR tests use the UCLA-LBLE-generated radiance tables covering measurement ranges of both COT and EPS. Randomly distributed noises are added to these radiances according to the system specification noise model. These simulated radiances are then applied to retrieval algorithms. For Error Budget (EB) studies, perturbation of the no-noise radiance tables for various error sources were carried out to simulate typical uncertainties in sensor parameters, surface characteristics, and atmospheric soundings. Using Litton-TASC's Cloud Scene Simulation Model (CSSM) along with the perturbed radiance tables, cloud optical depth and associated reflectance/radiance fields are generated for several defined scenes. Error budgets are developed by applying these reflectance/radiance fields to retrieval algorithms. The methodologies and results of algorithm sensitivity studies on the retrieval of COT and EPS are documented herein, along with relevant practical considerations.

1.0 INTRODUCTION

1.1 PURPOSE

On May 5, 1994, President Clinton directed that the meteorological satellite programs operated separately by the National Oceanic and Atmospheric Administration (NOAA), U.S. Department of Commerce (DOC) and the Department of Defense (DoD) be converged into a single satellite program. Currently, the operating NOAA satellite system belongs to the Polar-orbiting Operational Environmental Satellite (POES) program, and the operating DoD satellite system belongs to the Defense Meteorological Satellite Program (DMSP). The future converged system, the National Polar-orbiting Operational Environmental Satellite System (NPOESS), will provide a single national remote sensing capability to acquire, receive and disseminate global real-time weather data. The system will satisfy civil and national security operational requirements, and save more than $1 billion in government spending.

The Visible/Infrared Imager/Radiometer Suite (VIIRS) is being developed as part of the NPOESS platform to meet the operational requirements for the global remote sensing of atmospheric and surface properties. One of the prime applications of VIIRS channels is the remote sensing of cloud properties, including cloud cover/layers, cloud optical depth, cloud mean effective particle size, cloud top and base heights, cloud top temperature and pressure. These parameters are generally termed cloud Environmental Data Records (EDRs) in the NPOESS project.

This document is written to assist the sensor design and algorithm development particularly addressing the two NPOESS cloud EDRs: the Cloud Optical Thickness (COT) and Effective Particle Size (EPS). We present the theoretical basis for the solar and IR retrieval algorithms. We also describe the University of California at Los Angeles-Line-By-Line Equivalent (UCLA-LBLE) radiative transfer program that has been developed by our research group. LBLE was developed specifically for the purpose of simulating the clear and cloudy radiances for the algorithm development and sensitivity analyses using VIIRS channels.

1.2 SCOPE

This document covers the algorithm theoretical basis for the retrieval of the cloud optical thickness and effective particle size using VIIRS channel reflectances and radiances. Section 1 describes the purpose and scope of the document. Section 2 provides a scientific and historical background. The processing concept and algorithm description is presented in Section 3. Section 4 summarizes relevant assumptions and limitations. Finally, literature references used throughout the document are provided in Section 5.

1.3 VIIRS DOCUMENTS

VIIRS Sensor Requirement Document (SRD).

VIIRS System Specification Document (SS154640).

VIIRS Error Budget Document (Y3249.V3).

1.4 REVISIONS

Y2393, Version 5, Revision 1, Cloud Effective Particle Size and Cloud Optical Thickness ATBD, May 2002.

Y2393, Version 5, Revision 2, Cloud Effective Particle Size and Cloud Optical Thickness ATBD, February 2004.

Y2393, Version 5, Revision 3, Cloud Effective Particle Size and Cloud Optical Thickness ATBD, April, 2004Corrected erroneous equations, added missing algorithms, added omitted coefficients and added missing assumptions throughout ATBD. Added necessary detail for retrieval code implementation. Deleted Appendices E and F which contained error budgets.

Y2393, Version 5, Revision 4, Cloud Effective Particle Size and Cloud Optical Thickness ATBD – add detailed discussion of IR equations, closure issue in IR method, etc., August 2004

Y2393, Version 5, Revision 5, Cloud Effective Particle Size and Cloud Optical Thickness ATBD, add discussion of Quality Flags, June 2005

Y2393, Version 5, Revision 6, Cloud Effective Particle Size and Cloud Optical Thickness ATBD, add discussion of enhancement in IR algorithms in using M14 and M16 channels, March 2006

2.0 EXPERIMENT OVERVIEW

This section contains three major subsections. Subsection 2.1 describes the objectives of the cloud optical depth and effective particle size retrievals. Subsection 2.2 describes the characteristics of the VIIRS instrument. Subsection 2.3 addresses the cloud optical depth and effective particle size retrieval strategy.

2.1 OBJECTIVES OF CLOUD OPTICAL THICKNESS AND EFFECTIVE PARTICLE SIZE RETRIEVALS

Cloud optical thickness and effective particle size are two key NPOESS cloud EDRs. The objective of the cloud retrieval algorithms using the VIIRS cloud retrieval channels is to achieve comprehensive retrieval of the cloud optical thickness and effective particle size meeting the System Specification Requirements for these EDRs.

The importance of clouds in weather and climate processes has been recognized as a result of numerous observational and modeling studies. Cloud microphysics, phase, and particle shape and size distributions determine the cloud optical properties. These optical properties affect the emission, transmission, reflection and absorption of radiation by the cloud, and therefore modulate the balance of the atmospheric radiation budget. Clouds can be divided according to their particle phase into cirrus (ice) clouds and water (low) clouds. Both types of clouds are global in nature. Cirrus clouds occur primarily in the upper troposphere and the lower stratosphere, and are composed almost entirely of irregularly shaped, non-spherical ice crystals. Their global coverage is more than 30%. On the other hand, water clouds occur primarily in the middle and lower troposphere, and are composed of spherical water droplets. Their global coverage is more than 40%. Information on cirrus and water cloud parameters is critically important to the development of cloud forecast models, the upgrading of real-time global cloud analyses, the investigation of cloud feedbacks in global climate change, and the development of remote sensing of aerosols and surface parameters.

There are several well-documented and well-tested approaches to the satellite remote sensing of cloud optical thicknesses and effective particle sizes (e.g., King *et al*., 1996a, b; Minnis *et al*. 1998; Baum *et al*. 2000). All of these methods are based on the assumption of radiative transfer in plane-parallel clouds. These techniques exploit the spectral dependence of water and ice extinction of atmospheric radiation, using wavelengths at which absorption by water vapor and other gases is minimal, and at which the scattering and absorption by cloud particles are sensitive to the cloud particle size distribution. In the past, cirrus cloud parameters (optical depth, temperature, emissivity, etc.) have been inferred by using IR imaging and sounding channels (e.g., Szejwach, 1982; Arking and Child, 1985; Liou *et al.,* 1990).

In particular, Ou *et al*. (1993a) developed a physical retrieval scheme using radiance data from AVHRR $3.7\mu m$ and $10.9\mu m$ channels to infer nighttime cirrus cloud parameters, including cloud temperature, optical depth, and mean effective ice crystal size, based on the theory of radiative transfer and microphysics parameterizations. This retrieval scheme has

been applied to the nighttime AVHRR data collected during the First International Satellite Cloud Climatology Project Regional Experiment—Intensive Field Observation (FIRE-I IFO). Validation of the cirrus cloud parameters from this program has been carried out using co-located *in situ* ice crystal size distribution from 2-D probe measurements and balloon-borne replicator data (Ou *et al*., 1995; 1998). The balloon-borne replicator data can provide a nearly continuous vertical record of ice crystal size distributions in a Lagrangian sense. For validation purposes, an analytical method has also been developed to derive the optical depth and mean effective ice crystal size from the replicator data taking into account the effects of different shapes and sizes.

Ou *et al*. (1996) developed a multiple threshold test scheme to detect cloud phase and multi-layer cirrus cloud systems using AVHRR data, based on the physical properties of the AVHRR channel radiances. This scheme has been applied to the AVHRR data collected over the FIRE-II IFO area during nine overpasses within seven observational dates. Results from the cloud typing program have been verified using co-located and coincident ground-based radar and lidar return images (e.g., Clothiaux *et al*., 1995), balloon-borne replicator data and National Center for Atmospheric Research (NCAR) Cross-chain Loran Atmospheric Sounding System (CLASS) humidity soundings on a case-by-case basis. Subsequently, the daytime IR retrieval program was modified for the retrieval of cirrus cloud parameters in multi-layer cloud systems. Validation of the multilayer cirrus cloud retrieval has been performed for two dates during FIRE-II IFO.

A number of studies on the determination of water cloud optical thicknesses and effective droplet radius during daytime have also been carried out using radiances from airborne visible and near-IR radiometers on aircraft (e.g., Hansen and Pollack, 1970; Twomey and Cocks, 1982 and 1989; Nakajima and King, 1990). The underlying principle on which these techniques are based is the fact that the reflection function of clouds at a non-absorbing channel in the visible wavelength region is primarily a function of the cloud optical thickness, whereas the reflection function at a water (or ice) absorbing channel in the near-infrared (e.g., $1.61\mu m$ channel) is primarily a function of cloud particle size (King *et al*., 1996). These studies have demonstrated the applicability of remote sensing methods to the determination of cloud optical and microphysical properties for water clouds using visible and near-IR channel reflectances. The principle of this two-channel correlation technique is now being applied to the development of an algorithm for the determination of cirrus microphysical and optical properties using the MAS 0.657 and $1.609\mu m$ channel reflectances (e.g., Rolland *et al*., 2000). Though initial success has been achieved for the retrieval of cloud optical and microphysical parameters using both IR and solar approaches, further algorithm sensitivity and validation studies are required in order to assess the accuracy and precision of these methods when applied to measurements on a global scale.

The cloud optical depth and effective particle size retrieval algorithms, together with the prospective VIIRS sensor, are being developed to meet Specification requirements for the respective cloud EDRs. Under the VIIRS sensor/algorithm development concept, these requirements are "flowed down" to the design of the most cost-effective sensor/algorithm solution that meets these requirements. This is accomplished through a series of flowdown tests and error budget analyses, which effectively simulate sensor and algorithm

performance over a range of environmental and operational scenarios. The error budgets are briefly described in Sections 3.4 and 3.5. They are described in much more detail in the Raytheon VIIRS Error Budget, Version 3 (Y3249), and in Ou *et al.* (2003).

2.1.1 Cloud Optical Depth

The SRD provides the following definition for Cloud Optical Depth:

Cloud optical depth is defined as the extinction (scattering + absorption) vertical optical thickness of all cloud layers in a vertical column of the atmosphere. Optical thickness ( ) is related to transmittance (t) by t= exp (-). Optical thickness is wavelength dependent and is to be measured in at least two narrow bands centered at 450 nm (TBR) and 850 nm (TBR), with TBD nm bandwidth.

In the present retrieval algorithms, the retrieved cloud optical depth is defined as that at 0.55 m. Table A.1 in Appendix A summarizes the System Specification requirements for this parameter.

2.1.2 Cloud Effective Particle Size

The SRD provides the following definition for Cloud Effective Particle Size:

Effective cloud particle size is defined as the ratio of the third moment of the drop size distribution to the second moment, averaged over a layer of air within a cloud.

Table A.2 in Appendix A summarizes the System Specification requirements for this parameter.

2.2 BAND CHARACTERISTICS

VIIRS is currently being designed based on cost, NPOESS requirements of the sensor, and the specified threshold/objectives requirements. Table 1 lists the VIIRS bands and bandwidths. Bands used by the cloud EDR algorithms are marked with "x". Figure 1 shows the wavelength locations of seven VIIRS visible and near-IR channels. The atmospheric zenith transmittances from altitudes 10, 5 and 0 km to the top of atmosphere are calculated from the UCLA-LBLE model based on the U.S. Standard Atmosphere. The solar zenith angle is 32°. Note that all these channels, except the channel at $1.378\mu m$, are located at window wavelengths associated with very high atmospheric transmittance. During the period of the project, slightly shifted central wavelengths and band widths have been used for algorithm development and sensitivity studies. Because the differences for cloud and gaseous optical properties due to these band shifts are small, the results of algorithm studies using the shifted bands can be applicable to the bands specified in Table 1. Preliminary studies have been performed to verify this point. At present, VIIRS is designed to scan through nadir in a plane perpendicular to the velocity vector of the spacecraft, with the maximum scan extending up to 55° on either side with respect to the spacecraft nadir. At a nominal orbital altitude for the NPOESS platform of about 833km, this yields a swath width of 3000km centered on the satellite nadir ground track. Three of the VIIRS reflective

channels (0.672, 1.24 and 1.61μm) will be used in our solar cloud retrieval algorithm. One mid-wave IR channel (3.7μm) and one long-wave IR channel (8.55, 10.7625 and 12.013μm) will be used in the IR retrieval algorithm. Both the solar and IR channels are located in water vapor window regions.

Table 1. VIIRS Baseline Bands and Bandwidths for the Cloud EDRs (indicated with "x").

VIIRS BAND	(μm)	Bandwidth (μm)	Cloud Effective Particle Size	Cloud Optical Depth
M1	0.412	0.020		
M2	0.445	0.018		
M3	0.488	0.020		
M4	0.555	0.020		
I1	0.640	0.080		
M5	0.672	0.020	x	x
M6	0.746	0.015		
I2	0.865	0.039		
M7	0.865	0.039		
M8	1.240	0.020	x	x
M9	1.378	0.015		
I3	1.610	0.060		
M10	1.610	0.060	x	x
M11	2.250	0.050		
I4	3.740	0.380		
M12	3.700	0.180	x	x
M13	4.050	0.155		
M14	8.550	0.300	x	x
M15	10.7625	1.000	x	x
I5	11.450	1.900		
M16	12.0125	0.950	x	x

US1976 Standard Atmosphere, $\theta_0 = 32^o$, $A_s = 0.0$
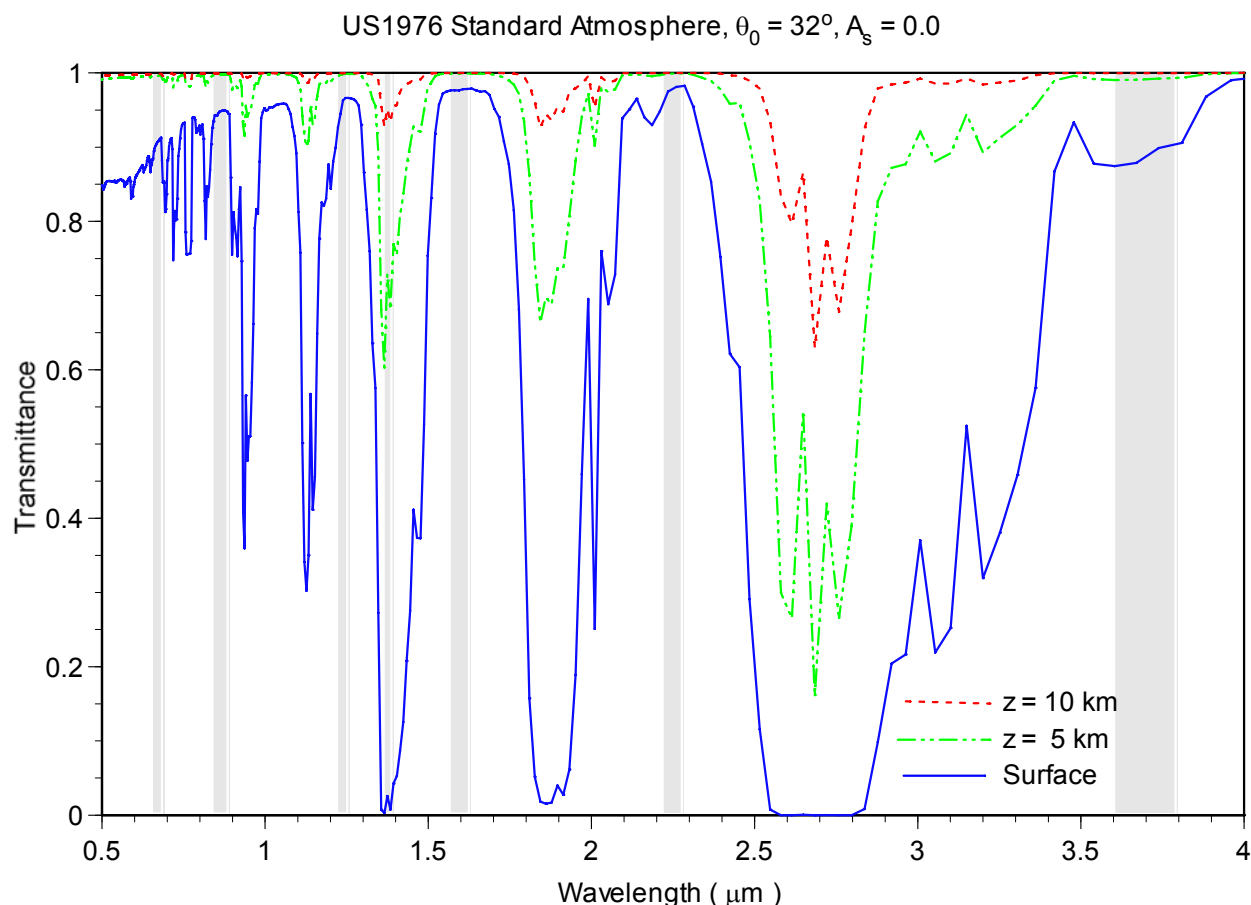
Figure 1. Transmittance Characteristics of Seven VIIRS Solar Channels centered at 0.672, 0.865, 1.24, 1.378, 1.61, 2.25 and 3.7μm. The atmospheric zenith transmittances are calculated from the LBLE model for three levels at 10 km, 5 km and the surface based on the US Standard Atmosphere at a 32° solar zenith angle.

2.3 RETRIEVAL STRATEGY

A high-level flow diagram of the general approach to determining the COT and EPS parameters is provided in Figure 2. Input parameters required by these algorithms include other VIIRS derived quantities (e.g., cloud mask), VIIRS radiances and scenario parameters (e.g., sun/sensor geometry). The overall processing begins with the detection of cloud-contaminated pixels and the determination of their associated phase via the VIIRS cloud mask program. For each cloud phase, the retrieval algorithms contain two basic approaches: solar and infrared (IR). The solar approach uses the reflectances of the 1.61μm channel and either 0.672μm (non-snow/ice surface) or 1.24μm (snow/ice surface) channels for daytime retrieval of COT and EPS. It determines these cloud parameters by matching measured reflectances with those from the comprehensive radiance look-up tables (LUTs), which are to be constructed using pre-computed radiances from the LBLE for a wide range of scenarios. The IR approach utilizes radiances of the VIIRS 3.7, 8.55, 10.7625 and 12.013

μm channels to infer cloud temperature and IR emissivity, from which the COT and EPS can be determined on the basis of the theory of radiative transfer and parameterizations.
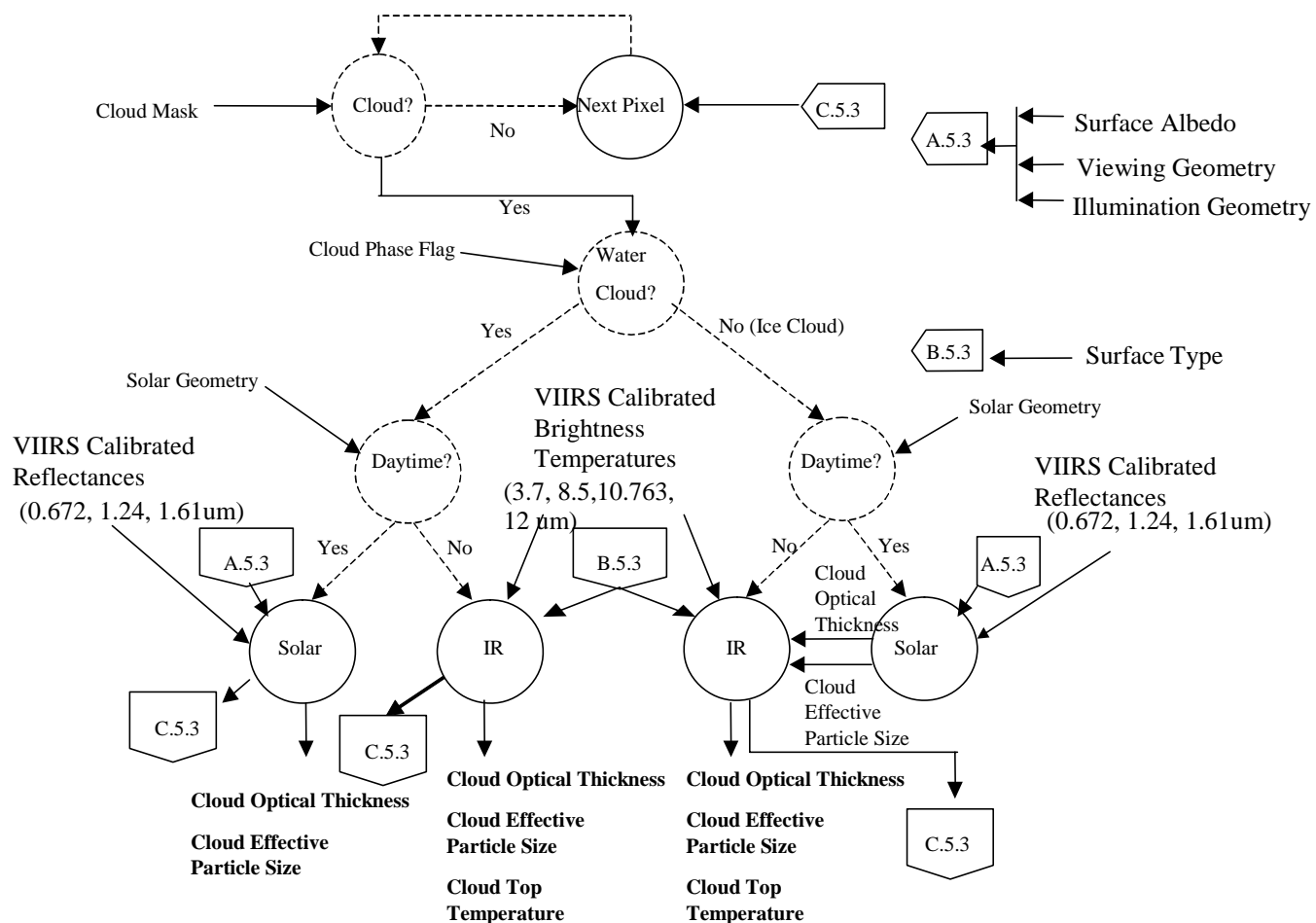
Figure 2. A High-Level Flow Chart describing the General Retrieval Strategy for Cloud Optical Thickness and Effective Particle Size.

3.0 ALGORITHM DESCRIPTION

3.1 PROCESSING OUTLINE

The development of algorithms for the retrieval of cloud optical thickness (or optical depth) and effective particle size using the VIIRS channel reflectances/radiances involves a series of processing steps. As shown in Figure 3, the first step in the process involves defining scenarios to be used in algorithm sensitivity tests. These scenarios form the basis for defining the input parameters required by the radiative transfer model. The input parameters include climatic (or sounding) atmospheric profiles, sun-sensor geometries, cloud phases, surface properties, gaseous absorption properties and cloud radiative properties. In the algorithm development and sensitivity studies for the retrieval of cirrus and water cloud parameters, the LBLE radiative transfer model is used, which is described in section 3.3.1.7. The LBLE is the most advanced code for computing high spectral resolution radiance using a combination of the correlated-k distribution (CKD) method and the adding-doubling method. The results from the LBLE have been compared with those from MODTRAN, as described in section 3.3.1.7. It is shown that for larger cirrus cloud optical depths, the radiance from LBLE differs greatly from that of MODTRAN, mainly because MODTRAN assumes that the radiance is azimuthally independent.
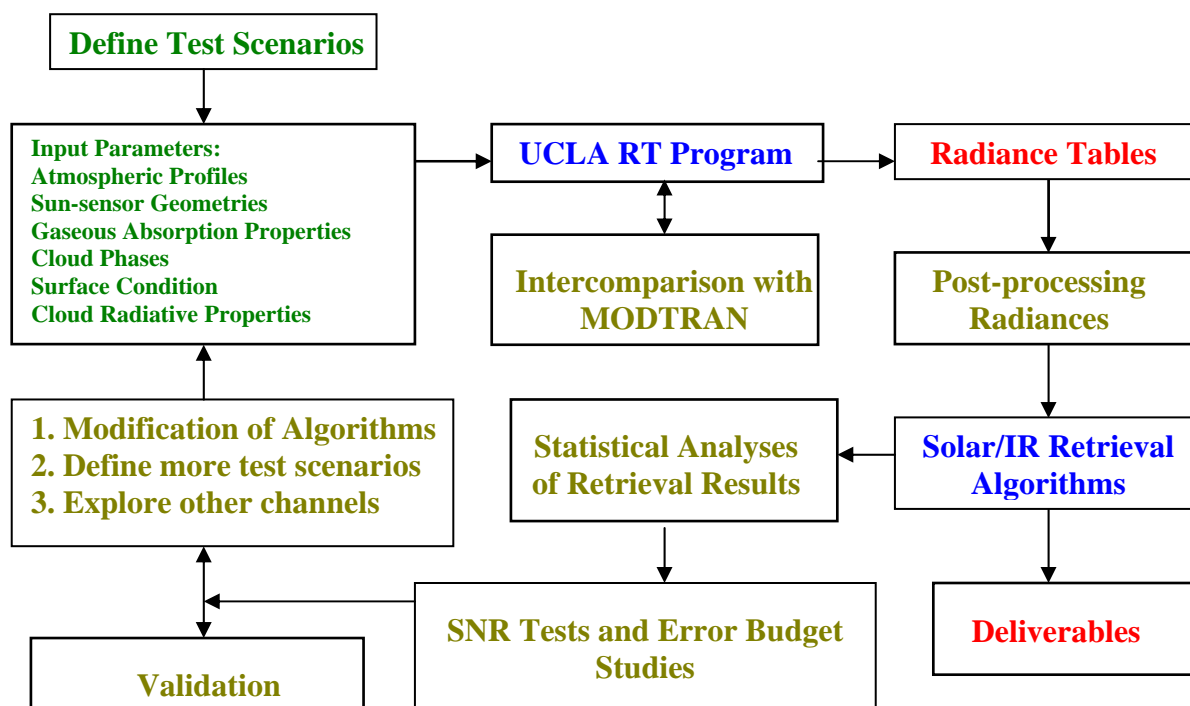
Figure 3. A High-Level Flow Diagram depicting the Processing Outline of the Data Flow of the VIIRS Channel Radiance in the Development of VIIRS Cloud EDR Retrieval Algorithms.

A given specification for a scenario includes an atmospheric profile, solar and sensor geometry, band parameters, cloud phase and cloud top height. For each scenario, the LBLE is executed over a wide range of optical thicknesses and effective particle sizes. Results for each scenario and for each spectral band are stored in the format of radiance tables. These radiance tables are used throughout the algorithm sensitivity studies. Post-processing procedures have been developed to convert the numbers in radiance tables into appropriate forms for the cloud parameter retrieval algorithms. For the solar algorithm, the radiance values are converted into reflectance using the solar spectral irradiance at the top of atmosphere. For the IR algorithm, the radiances are converted into spectrally averaged intensities and brightness temperatures. In the algorithm sensitivity studies, radiances are further processed to simulate instrument noises or calibration errors. For example, in the signal-to-noise (SNR) sensitivity analyses, noises are added to radiances according to the sensor noise model. Synthetic retrievals are carried out using the set of converted solar reflectances or IR intensities. The results of the retrieval processes are then statistically analyzed to compute the metrics described in the SRD (accuracy and precision errors, etc.). The metrics are then compared with specification requirements to determine if the retrieval algorithms meet these requirements.

If some part of the metrics fails the threshold/objective test, we perform an iterative process. There are three options. Modify the algorithm to improve the performance. Define more scenarios to search for the exact limit of application of the algorithms. Last of all, use additional channel data to improve the algorithm behavior. Finally, we validate retrieval algorithms by applying airborne (e.g., MAS) or satellite (e.g., AVHRR and MODIS) imagery data to the algorithms. The data have similar channel characteristics to those of VIIRS. We will compare retrieval results using imagery data collected during various field campaigns with collocated *in situ* microphysical and ground-based radiation measurements.

3.2 ALGORITHM INPUT

The required input parameters for the retrieval of cloud optical thickness and effective particle size come from VIIRS and non-VIIRS sources and are summarized individually in the following paragraphs. The VIIRS data either come directly from the VIIRS processing stream or are generated from the radiative transfer model.

3.2.1 VIIRS Data

3.2.1.1   VIIRS Calibrated Brightness Temperatures and Reflectances

Brightness temperatures and reflectances are required for input into the IR and solar algorithms respectively.

3.2.1.2   VIIRS
Illumination and Viewing Geometry Parameters

These include solar and sensor-viewing zenith and azimuthal angles with respect to the target normal. Information on the solar zenith angle determines whether daytime or nighttime algorithms will be used.

3.2.1.3   VIIRS
Cloud Mask IP

The identification of cloudy/clear pixels and associated cloud phases may be obtained from the VIIRS cloud mask product. Cloud/clear information will be used to filter out clear pixels.

3.2.1.4   VIIRS
Surface Albedo IP

These data are required for proper use of the solar reflectance LUTs. However, surface albedo is determined from an internally stored table with given the surface type from the VIIRS Cloud Mask. The VIIRS surface type IP may be added however, as future enhancement.

3.2.1.5   VIIRS
Surface Type IP

This information determines whether the solar algorithm will use M5 ($0.672\mu m$) reflectances (non-snow/ice surfaces) or M8 ($1.24\mu m$) reflectances (snow/ice surfaces). In addition, surface albedo is derived from knowledge of the surface type. However, VIIRS surface type IP currently is not a required input to the COP code. Instead, surface type is taken from the VIIRS Cloud Mask.

3.2.2 Off-line Data

These data are necessary for pre-processing but are not required operationally.

3.2.2.1
Atmospheric Sounding

In the construction of reflectance LUTs, it is necessary to define the atmosphere using temperature, pressure and moisture profiles to compute the clear and cloudy radiances.

3.2.2.2   Spectral
Library

This library contains spectral reflection and emission properties for various surface types and is used for the creation of the solar reflectance LUTs. These are the internally stored table described in Section 3.2.1.4 and 3.2.1.5.

3.2.2.3   Exo-Atmospheric Solar Spectral Irradiances

These are required to convert radiance to bi-directional reflectance factors for the reflectance LUT. The solar constant for each VIIRS cloud retrieval band is determined based on the solar irradiance spectrum used in MODTRAN V3.7.

3.2.2.4   VIIRS Band Parameters

These are required for the derivation of single-scattering properties of cloud particles and for the construction of reflectance LUTs.

3.2.2.5   Cloud Top Height

These are required for the construction of radiance LUTs for solar algorithms. The LUTs are generated by assuming cloud top heights at 10 km and cloud thickness of 1 km for ice and water clouds respectively.

3.3 THEORETICAL DESCRIPTION OF OPTICAL DEPTH AND EFFECTIVE PARTICLE SIZE RETRIEVALS

In section 3.3.1, we will discuss the physics of the problem, including the characteristics of cloud particle size distribution, radiative properties of clouds, the parameterization of atmospheric gaseous absorption, the modeling of radiative transfer within clouds and the inter-comparison of computed radiances from the LBLE and MODTRAN for both clear and cloudy atmospheres. In section 3.3.2, we focus on the mathematical description of the retrieval algorithms.

3.3.1 Physics of the Problem

Developing accurate and reliable cloud remote sensing programs requires that a detailed and accurate radiative transfer program be available for algorithm development and sensitivity studies. To simulate the atmospheric scattering/absorption effects accurately, it is essential that reliable phase functions and single-scattering properties for non-spherical ice crystals, spherical water droplets, molecules and aerosols be used. Single-scattering properties include the extinction coefficient (or efficiency), the single-scattering albedo and the asymmetry factor. It is also important to incorporate an efficient and accurate parameterization program for computing atmospheric gaseous absorption/emission coefficients. Section 3.3.1.1 presents the derivation of typical optical properties of cirrus clouds. We establish representative ice crystal size distributions by analyzing the observed ice crystal size distributions that have become available from field experiments in the mid-latitude region (e.g., FIRE-I IFO). The objective is to characterize the ice crystal size distribution in terms of sizes and shapes that are representative of cirrus for remote sensing applications. Also in section 3.3.1.1, we discuss the calculation of the scattering and absorption properties of ice crystals of various sizes and shapes based on the geometric-

optics/integral-equation and finite-difference time domain methods. In sections 3.3.1.2, 3.3.1.3 and 3.3.1.4, we address the determination of optical properties of water droplets, molecules and aerosols, respectively. In section 3.3.1.5, we describe the parameterization of atmospheric gaseous absorption by way of the correlated-*k* distribution approach. Finally, in section 3.3.1.6, we explain how the single-scattering properties for combined cloud particles and gases are derived.

The LBLE radiative transfer model is employed to carry out the algorithm development and sensitivity studies. In Section 3.3.1.7, we describe the physical principles and model structure of the LBLE. We also present results of an inter-comparison between LBLE and MODTRAN-DISORT (MD). It is shown that, in general, the MD radiance for optically thick clouds differs from the LBLE radiance by more than 10 percent. This difference increases with increasing optical depths. The present retrieval program is closely coupled with the LBLE. If simulated VIIRS radiances were generated using the MD or other program with a similar philosophy for modeling multiple scattering, it is expected that the retrieved cloud EDRs would not meet the EDR specification requirements.

3.3.1.1
Microphysical and Radiative Properties of Cirrus Clouds

Analysis of the observed ice crystal size distributions

Development of the remote sensing algorithms for ubiquitous cirrus clouds requires comprehensive knowledge of two fundamental ice microphysics parameters: ice crystal size distribution and ice crystal shape. Both vary in space and time, and are associated with microphysical processes, including diffusional growth/shrinkage by water vapor deposition/sublimation, and aggregation by collision and coalescence between ice crystals. It is necessary to define representative ice crystal size distributions and shapes for the calculations of phase functions and other relevant single-scattering properties used in satellite remote sensing applications. In conjunction with our ongoing radiative transfer and satellite remote sensing studies involving cirrus clouds, we have analyzed six composite ice crystal size distributions that were obtained from aircraft observations presented by Heymsfield and Platt (1984), Takano and Liou (1989) and the FIRE-IFO microphysical data. They are denoted as cold Ci, -60° C, Cs, FIRE-I IFO 1 Nov, FIRE-I IFO 2 Nov, and Ci Uncinus. Figure 4 shows the six ice crystal size distributions. The ice crystal sizes span from about 5 to 2000μm with shapes ranging from bullet rosettes, solid and hollow columns, plates to aggregates. We define a mean effective size to characterize ice crystal size distribution in the form:

$$D_e = \int D^2 L \, n(L) \, dL \Big/ \int D L \, n(L) \, dL \qquad (1)$$

where D and L denote the width and the maximum dimension of a non-spherical ice crystal, respectively, and $n(L)$ is the size distribution in terms of L. The rationale for defining D_e to represent ice crystal size distribution is that the scattering of light is related to the geometric cross section, which is proportional to LD. The preceding definition of the mean effective size is applicable to irregular and complex ice crystal shape (Ou *et al.,* 1995). This definition

is consistent with that in the SRD. It is noted that the VIIRS EPS definition is for "water cloud droplets" only, because it mentioned "droplet size distribution". It does not specifically define the effective particle size for non-spherical ice crystal size distribution, although a similar definition for ice crystal is suggested. Therefore, for ice crystal, we interpret that the third and second moments of the ice crystal size distribution to be the integration of the ice crystal size distribution weighted by the 3rd and 2nd powers of the characteristic lengths of ice crystal, respectively.   Since the ice crystal is mostly in hexagonal columnal shape, this characteristic length can be either the maximum dimension (L) or the maximum width (D). Thus, referring to Eq. (1), the integral in the numerator is consistent with our interpretation of the third moment of the ice crystal size distribution, and the integral in the denominator is consistent with our interpretation of the second moment of the ice crystal size distribution. In the present algorithm development and sensitivity studies, effective particle size for ice crystals is defined as half of the mean effective size, because D_e is equivalent to a measure of diameter, while the effective particle size is equivalent to radius. At this point, sufficient information concerning ice crystal habit and percentage of individual habits for a given size distribution is not available. We propose ice crystal habit and associated aspect ratios on the basis of the *in situ* 2-D probe and replicator data. Following Takano and Liou (1989a), we have aggregated the size distributions into 5 bins: 10-30μm with bin-center at 20μm, 30-70μm with bin center at 50μm, 70–170μm with bin-center at 120μm, 170-430μm with bin-center at 300μm, and 430–1070 μm with bin center at 750μm. The aspect ratios, *L/D*, used are 20/20, 50/40, 120/60, 300/100, and 750/160 (in units μm/μm). These roughly correspond to the observations reported by Auer and Veal (1970). We have evaluated the mean effective ice crystal size for the six size distributions, which are presented in Table 2.
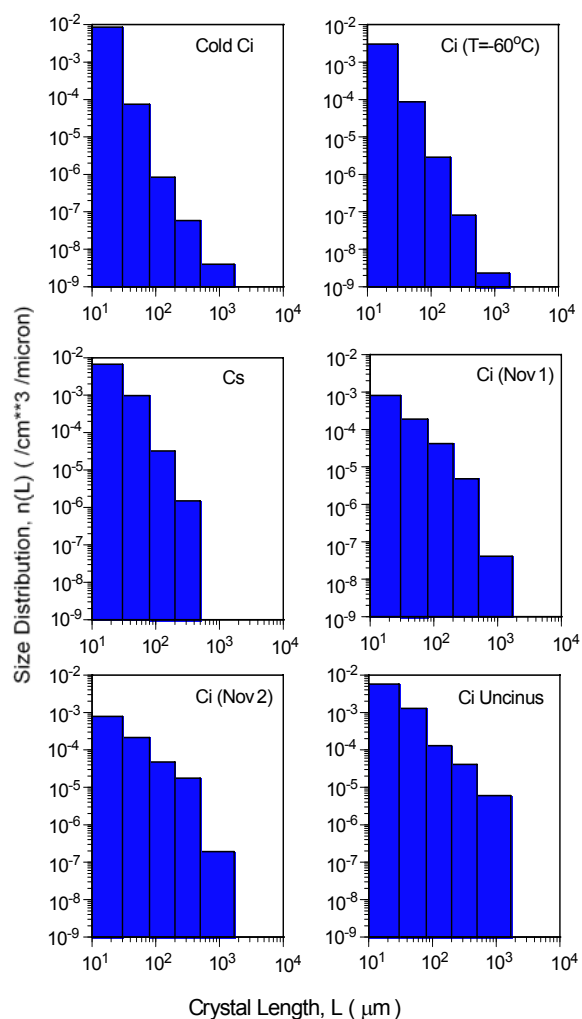
**Figure 4. The Six Discretized Ice Crystal Size Distributions
used in Generating Radiances and Algorithm Sensitivity Studies.**

**Table 2. Mean Effective Size of the Six Ice Crystal Size
Distributions.**

Ice crystal size distribution	Mean effective size (μm)
Cold Ci	23.9
T = -60 ^{o} C	30.4
Cs	41.5
FIRE-I Nov. 1	75.1
FIRE-I Nov. 2	93.0
Ci Uncinus	123.6

Single-scattering properties for ice crystals

Unlike the scattering of light by spherical water droplets, which can be solved by the exact Mie theory, an exact solution for the scattering of light by hexagonal ice crystals covering all shapes (habits) and sizes does not exist in practical terms. Although several numerical methods have been developed to solve the problem of light scattering by non-spherical particles, they are usually applicable to size parameters (*ka*, where *k* is the wavenumber and *a* is the semi-width of an ice crystal) smaller than approximately 20, as discussed by Liou and Takano (1994), Yang and Liou (1995) and the references cited therein. In the past two decades, significant research on solving light scattering by regular and complex ice crystals has been carried out by means of the geometric ray-tracing technique, commonly employed to identify the optical phenomena occurring in the atmosphere. In the limit of geometric optics, an incident wave may be considered as being composed of a bundle of rays that strike the ice crystal and undergo reflection and refraction along a straight line. The laws of geometric optics are applicable to the scattering of light by an ice crystal if its size is much larger than the incident wavelength. In those cases the geometric rays can be localized.

In recent years, we have developed a Monte Carlo/geometric ray-tracing method for the computation of the scattering, absorption and polarization properties of ice crystals with various regular and irregular structures. These structures include solid and hollow columns, single and double plates, dendrites, bullet rosettes and aggregates (Takano and Liou, 1995). The shape of these ice crystals are defined by appropriate geometric models and incident coordinate systems. The incident photons are traced with a hit-and-miss Monte Carlo method and followed by geometric reflection and refraction on the crystal boundary. Absorption can be accounted for by means of stochastic procedures. For some of the quasi-spherical ice particles, such as frozen droplets, we can approximate them by spheroids. In those cases, the scattering and absorption properties can be computed exactly (Takano *et al.,* 1992).

In the geometric optic method, the extinction efficiency is set as 2. Thus the extinction coefficient is equal to twice the total cross sectional area per unit volume and is spectrally independent for a given ice crystal size distribution. The single-scattering albedo is parameterized in terms of the absorption coefficient $k_i = 4\pi m_i/\lambda$ and the aspect ratio *L/D*:

$$\varpi = Q_s / Q_e = \sum_{n=0}^{4} b_n z^n \qquad \text{where} \qquad z = k_i a \frac{3\sqrt{3}(L/D)}{\sqrt{3} + 4(L/D)} \qquad (2)$$

The parameters Q_s and Q_e denote the scattering and extinction efficiencies, respectively. The scattering phase function is obtained from the phase matrix, which is determined using the Monte Carlo/Geometric ray-tracing method. We assume that ice crystals are randomly oriented.

For non-spherical ice crystals, the phase function contains a strong forward peak at 0° scattering angle. The forward scattered energy within 0°-5° scattering angle range produced by diffraction is four to five orders of magnitude greater than it is in the side and backscattered directions. To incorporate the forward peak contribution in multiple scattering,

we consider an adjusted absorption and scattering atmosphere, such that the fraction of scattered energy residing in the forward peak, is removed from the scattering parameters. These parameters include the optical depth, single-scattering albedo and asymmetry factor. Thus the phase function is expressed as

$$f_D = \frac{1}{2\varpi(1 - f_\delta)},$$

$$P(\Theta) = (1 - f_D)P_G(\Theta) + f_D P_D(\Theta), \quad \text{where} \tag{3}$$

and f_D is the ratio of the diffracted light to the entire scattered light.

Geometric ray-tracing requires the principle of localization in which the particle size must be larger than the incident wavelength. In addition, it is assumed that the energy attenuated by the scatterer may be decomposed into equal extinction from diffraction and Fresnelian rays so that the extinction efficiency is equal to 2 regardless of the particle size parameter. To circumvent a number of shortcomings in the geometric-optics approach, we have developed a novel improvement by mapping the equivalent tangential electric and magnetic currents on the particle surface, obtained from geometric reflection and refraction, to far-field by means of the basic electromagnetic wave theory in two-dimensional (2-D) space (Yang and Liou, 1995). We have further extended the improved geometric-optics method in the 2-D case to three-dimensional (3-D) space, allowing arbitrary and random orientations of the ice crystals (Yang and Liou, 1996a). The improved geometric ray-tracing method is referred to as the geometric-optics/integral-equation hybrid method (GOM2).

For verification of the limitations of the geometric optics, we have also developed a finite-difference time domain (FDTD) technique pioneered by electrical engineers for the identification of irregular objects. It is a numerical technique for the solution of the Maxwell equations using appropriate absorbing boundary conditions. It is considered to be the "exact" numerical solution for light scattering by particles, as verified by the exact Mie results for long circular cylinders and spheres (Yang and Liou, 1996b). Because of numerical instability and required computer time, the FDTD method can only be applied to size parameters smaller than about 20. We show that the GOM2 method converges to the conventional ray-tracing method for size parameters larger than about 200. The conventional method breaks down when the size parameters of ice crystals are smaller than about 40-100, depending on whether the computations are for the cross sections or phase matrix. Moreover, based on comparison with the results computed from the FDTD method, the GOM2 technique is shown to be applicable to ice crystal size parameters as small as 15-20.

As pointed out previously, an exact solution for the scattering of light by hexagonal ice crystals covering all shapes and sizes does not exist in practical terms. However, by combining the GOM2 (*ka* > 20) and FDTD (*ka* < 20) methods, we have developed a unified theory for light scattering by ice crystals essentially for all sizes and shapes.

At this point, we have the theoretical tools to provide the basic scattering and absorption data required for a reliable simulation of the single-scattering properties of ice clouds. The unified theory for light scattering, along with representative ice crystal size distributions and shapes discussed in Section 3.3.1.1 are used to compute the phase function and single-scattering properties for all VIIRS cloud retrieval wavelengths listed in Table 1. The computations are quite extensive and require a careful selection of sizes and shapes. The influence of the mean effective size and variance on the single-scattering properties can both be examined with respect to the potential remote sensing of these parameters. Shown in Figure 5 are the phase functions for the six size distributions and for five VIIRS channels obtained from the Monte Carlo/Geometric ray tracing method. For the solar channels, the overall feature of phase function is not sensitive to the variation of size distribution because of the negligible absorption involved. The 22° and the 46° halos produced by two refracted rays are well illustrated for the phase functions for 0.672, 1.61 and 2.25μm channels, in addition to the forward diffraction peak. The magnitude of the forward scattering associated with diffraction varies with size distribution due to strong absorption. For scattering angles between about 150° and 160°, there is another peak for all sizes produced by rays undergoing double internal reflections. The magnitude of the side-scattering is larger for smaller ice crystals. For the thermal channels, the halos and the backscattering peaks all disappear due to strong absorption effects. Figures 6(a) and 6(b) show the single-scattering albedos and asymmetry factors associated with the six ice crystal size distributions and five VIIRS channels. In general, the single-scattering albedo decreases with increasing wavelengths, while the asymmetry factor increases with increasing wavelengths. For the solar channels, the single-scattering albedo decreases with increasing D_e, and is larger than 0.8. For the 10.7625μm channel, the single-scattering albedo varies between 0.4 and 0.5 due to particle absorption effects and increases with increasing D_e. The asymmetry factor increases with increasing D_e, implying that as D_e increases, more light is scattered in the forward direction.

3.3.1.2   Water Cloud Optical Properties

Water cloud properties for VIIRS solar channels have been generated using the Mie scattering code for water droplets. For a single water droplet, the extinction and scattering efficien

$$Q_s = \frac{2}{x^2} \sum_{n=1}^{\infty} (2n+1)(|a_n|^2 + |b_n|^2),$$

(4)

$$Q_e = \frac{2}{x^2} \sum_{n=1}^{\infty} (2n+1)\, \mathrm{Re}\, (a_n + b_n),$$

(5)

where $x = 2\pi r/\lambda$ (the size parameter), and a_n and b_n are coefficients in the expansion for scattered waves. The phase function for a single water droplet is obtained from:

$$P(\Theta) = 4\pi[i_1(\Theta) + i_2(\Theta)] / 2k^2 \sigma_s$$

(6)

where i_1 and i_2 are the square of the magnitude of the scattering functions, k is the wave number $(2\pi/\lambda)$, and σ_s is the scattering cross section.

A gamma distribution is assumed for the droplet size distribution. Subsequently, the average extinction and scattering coefficients are obtained from:

$$\beta_{e,s} = \int_{r_1}^{r_2} Q_{e,s}\pi r^2 n(r)dr,$$

(7)

where $n(r)$ is the droplet size distribution in terms of radius r, and r_1 and r_2 are the minimum and maximum radius in the size distribution. The average single-scattering albedo is then obtained as:

$$\overline{\varpi} = \beta_s \Big/ \beta_e$$

(8)
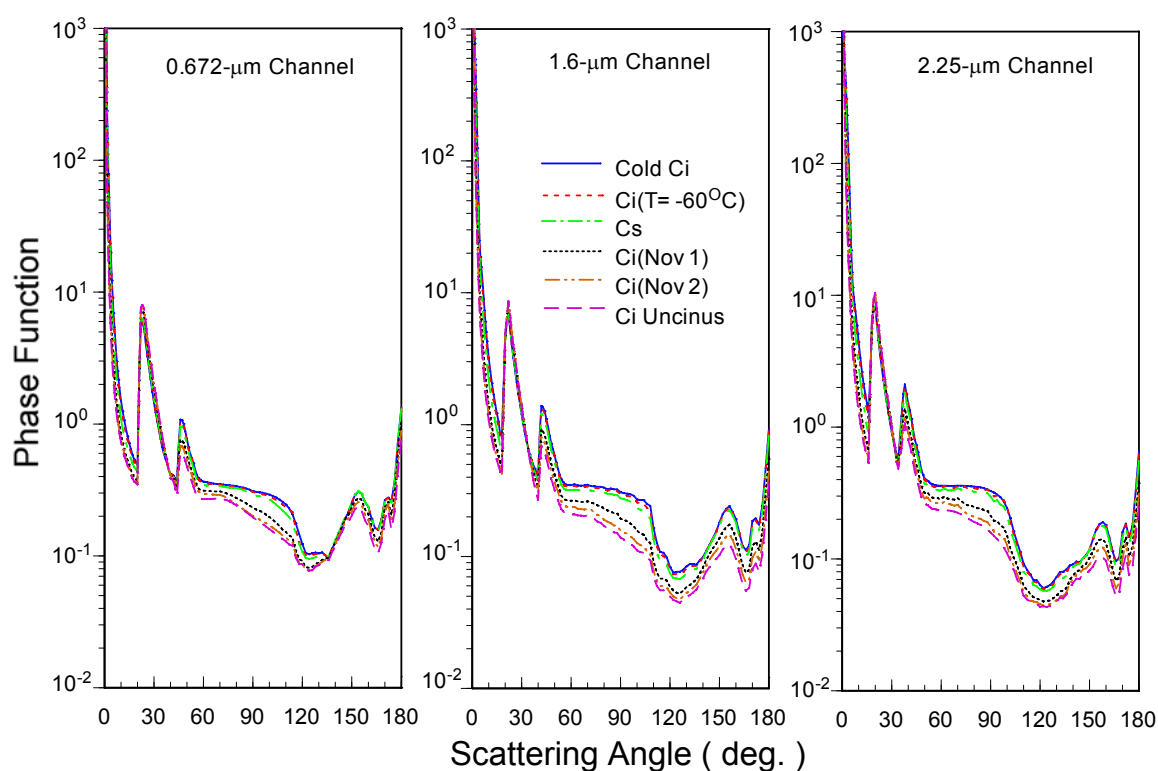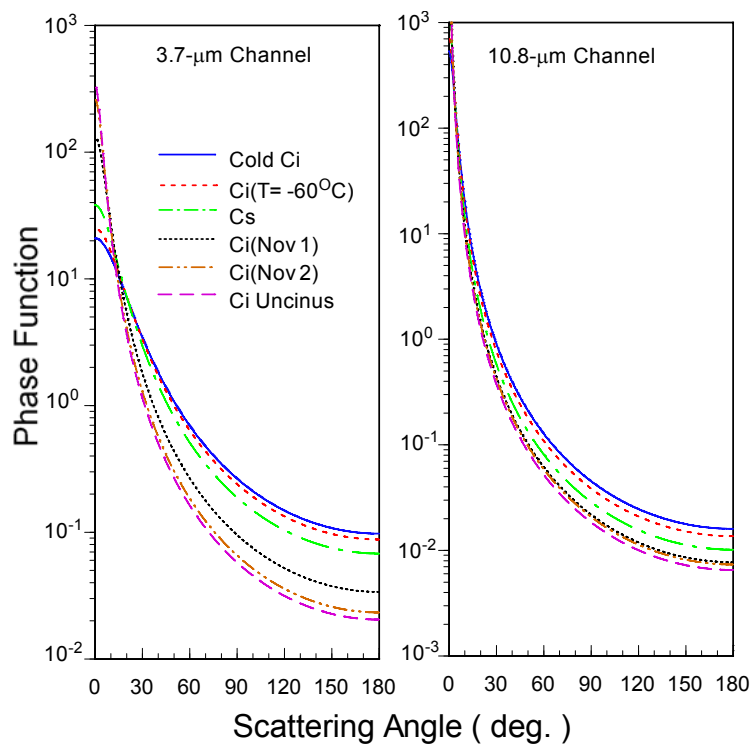
Figure 5. Phase Functions for the Six Ice Cloud Particle Size Distributions and for the Five VIIRS Channels.
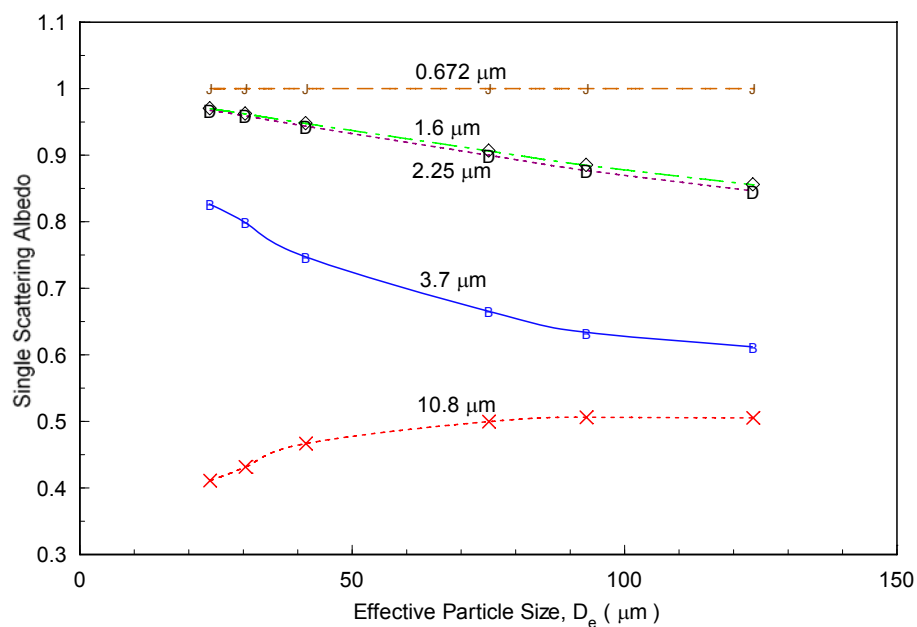
Figure 6a. Single-Scattering Albedos for the Six Ice Cloud Particle Size Distributions and for the Five VIIRS Channels.
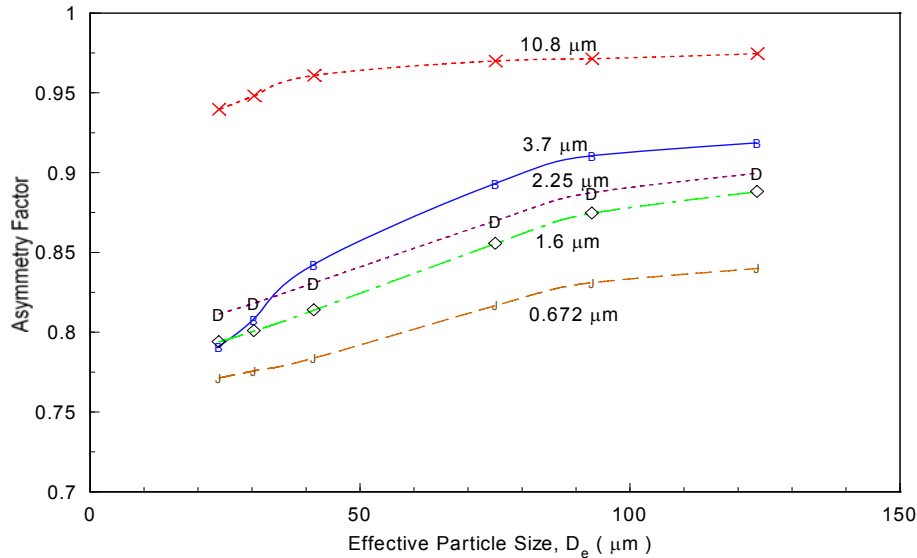
Figure 6b. Asymmetry Factors for the Six Ice Cloud Particle Size Distributions and for the Five VIIRS Channels.

Finally, the average phase function is obtained from

$$P(\Theta) = \frac{4\pi}{k^2 \beta_s} \int_{r_1}^{r_2} \frac{1}{2}[i_1(\Theta, r) + i_2(\Theta), r)]n(r)dr \, , \tag{9}$$

For VIIRS IR channels, we use an analytic approximation developed by Chylek *et al.* (1995) which is accurate to within a few percent when compared to exact Mie computations. Chylek's formulation is appropriate for wavelengths greater than 3μm. Comparing to Platnick's data (King *et al.,* 1996) at certain overlapping wavelengths, Chylek's formulation seems to be in good agreement.

3.3.1.3   Optical Properties for Rayleigh Scattering

For very small size parameters (<< 1), the effect of particle size is small, and the scattered intensity is inversely proportional to the fourth power of wavelength. This scattering regime is referred to as Rayleigh scattering. The scattering of solar radiation by air molecules falls within the Rayleigh scattering regime, which must be accounted in the calculation of visible radiance.

In the Rayleigh scattering regime, single–scattering albedo is set to 1 (conservative scattering). Following the classical solution by Rayleigh (1918), the phase function for incident un-polarized solar radiation is:

$$P(\Theta) = \frac{3}{4}(1 + \cos^2 \Theta). \tag{10}$$

The Rayleigh optical depth for the Earth's atmosphere is spectrally dependent, and can be computed according to the following parameterization (Hansen and Travis, 1974):

$$\tau = 0.008569\lambda^{-4}(1 + 0.0113\lambda^{-2} + 0.00013\lambda^{-4}), \tag{11}$$

where λ is the wavelength. The above equation is derived for standard surface pressure of 1013.25 mb. For λ=0.55μm, the optical depth is about 0.0973.

3.3.1.4 Aerosol Scattering

The averaged extinction coefficient, single-scattering albedo and asymmetry factor for individual aerosol particles are obtained in the same manner as those parameters for water droplets. However, we use the Henyey-Greenstein phase function (Liou, 1992) for approximation:

$$p_{HG}(\Theta) = \frac{(1-g^2)}{(1+g^2-2g\cos\Theta)^{3/2}}, \tag{12}$$

where g is the asymmetry factor.

3.3.1.5 Correlated-k Distribution Approach

The gaseous absorption coefficient is a function of wavenumber, pressure, and temperature, and can be written in terms of line strength $S_i(T)$ and line shape function $f_i(\ , p, T)$ in the form:

$$k(v, p, T) = \sum_i S_i(T) f_i(v, p, T) \tag{13}$$

For a given absorption gas and spectral interval, Δv, we introduce the k-distribution function $h(k)$, which is the probability density function such that $h(k)dk$ is the fraction of Δv within which the absorption coefficient is between k and $k + dk$. Thus the spectral-mean transmittance should depend on the k-distribution but is independent of the ordering of the absorption coefficients, $k(v)$, with respect to the wavenumber (Ambartzumian, 1936; Arking and Grossman, 1972). We may replace the wavenumber integration by integration over the k-space. Let the maximum and minimum absorption coefficient within Δv be k_{max} and k_{min}. Setting $k_{min} \rightarrow 0$ and $k_{max} \rightarrow \infty$ for mathematical convenience, the spectral-mean transmittance as a function of path length, u, may be expressed by:

$$T_{\bar{v}}(u) = \int_{\Delta v} e^{-k(v)u} \frac{dv}{\Delta v} = \int_0^\infty e^{-ku} h(k)dk \,, \tag{14}$$

where $h(k)$ is normalized to 1 in the domain $(0, \infty)$. Equation 14 defines the k-distribution approach, which is exact for the case of a homogeneous atmosphere. We may further define a cumulative probability function in the form:

$$g(k) = \int_0^k h(k)dk \,, \tag{15}$$

where $g(0) = 0$, $g(k \to \infty) = 1$, and $dg(k) = h(k)d(k)$. By definition, $g(k)$ is a monotonically increasing and smooth function in k space. It follows that the spectral-mean transmittance can now be expressed in terms of this cumulative probability function $g(k)$ in the form:

$$T_{\bar{v}}(u) = \int_{\Delta v} e^{-k(v)u} \frac{dv}{\Delta v} = \int_0^1 e^{-k(g)u} dg \,, \tag{16}$$

where $k(g)$ is referred to as the equivalent k function, which is the inverse function of $g(k)$. Since $g(k)$ is a smooth and monotonically increasing function in k space, $k(g)$ must also be a smooth and monotonically increasing function in g space.

In order to apply the k-distribution method to a nonhomogeneous atmosphere, we shall consider this atmosphere defined by two heights, z_1, and z_2. The spectral-mean transmittance can be written in the form:

$$T_{\bar{v}} = \int_{\Delta v} \exp[-\int_{z_1}^{z_2} k(v, p, T)\rho dz] \frac{dv}{\Delta v} \tag{17}$$

where ρ is the density of the absorber and we have introduced pressure and temperature dependence in the absorption coefficient. We wish to investigate the physical and mathematical conditions under which Equation 17 may be expressed in a form similar to Equation 16, namely:

$$T_{\bar{v}} = \int_0^1 \exp[-\int_{z_1}^{z_2} k(g, p, T)\rho dz] dg \tag{18}$$

The method for calculating spectral-mean transmittance based on Equation 18 is referred to as the Correlated K-Distribution method (CKD). In essence, the physical implication of CKD is that only one g exists for a given v at different heights.

Fu and Liou (1992) compared the distribution of the absorption coefficient in the wavenumber domain and in the cumulative probability (g) domain for the O_3 9.6μm band at p=25mb and T=220K. They show that the absorption coefficient is a high-frequency

oscillatory function of wavenumber but is smooth in the *g*-domain. Thus, the efficient integration in the *g*-domain replaces the cumbersome wavenumber integration, and the associated numerical integration can be carried out by evaluating the integral at only a few selected *g* values.

Evaluation of the spectral-mean transmittance in nonhomogeneous atmospheres requires coupled height and wavenumber integrations (Equation 17). Traditionally, these integrations have been separated by some approximations such that band models can be applied. In this sense, one-parameter scaling, two-parameter Curtis-Godson approximation (Liou, 1992) and three-parameter scaling are all based on the same philosophy. However, in the CKD approach, after transformation of the ν domain to the *g* domain, separate integrations of height and *g* are not necessary, because the height integration can be effectively carried out in *g* space under the correlated assumptions. The approach fundamentally differs from traditional band models and scaling approximations and appears to offer a direct solution to the intricate radiative transfer problem involving non-gray gaseous absorption.

3.3.1.6 Single-Scattering Properties for Combined Cloud and Aerosol Particles, Rayleigh Molecules and Gases

We divide a nonhomogeneous atmosphere into a number of layers, each of which is assumed to be homogeneous. For the case when attenuation by cloud particles, Rayleigh scattering and aerosols are occurring along with gaseous absorption, the total optical depth for each layer is:

$$\Delta\tau(g) = \Delta\tau^C + \Delta\tau^R + \Delta\tau^A + \Delta\tau^G(g), \tag{19}$$

where $\Delta\tau^C$, $\Delta\tau^R$ and $\Delta\tau^A$ represent the optical depths due to cloud particles, Rayleigh molecules and aerosols, respectively; $\Delta\tau^G(g)$ is the optical depth contributed by the gaseous absorption for a given *g* (the cumulative probability), which can be expressed by:

$$\Delta\tau^G(g) = k(g, p, T)\rho\Delta z \tag{20}$$

where $k(g,p,T)$ is the equivalent *k* function (Fu and Liou, 1992), ρ is the density of the absorber, and Δz is the geometric thickness of the layer. In this case, $\Delta\tau^C = \Delta\tau_s^C + \Delta\tau_a^C$, where $\Delta\tau_s^C$ and $\Delta\tau_a^C$ are cloud scattering and absorption optical depths, respectively. In the same manner, $\Delta\tau^A = \Delta\tau_s^A + \Delta\tau_a^A$, where $\Delta\tau_s^A$ and $\Delta\tau_a^A$ are aerosol scattering and absorption optical depths, respectively. Thus the combined single-scattering albedo can be obtained by:

$$\varpi(g) = \frac{\Delta\tau_s^C + \Delta\tau^R + \Delta\tau_s^A}{\Delta\tau^C + \Delta\tau^R + \Delta\tau^A + \Delta\tau^G(g)} \tag{21}$$

Similarly, when the phase function is applied to the radiative transfer program, it is expanded in the form:

$$P(\Theta) = \sum_{l=0}^{N} \varpi_l P_l(\cos\Theta) \qquad (22)$$

where $P_l(\cos\Theta)$ is the Legendre polynomial of order l, and ϖ_l is the expansion coefficient. The expansion coefficient for the composite phase function can be obtained by:

$$\varpi_l = \frac{\Delta\tau_s^C \varpi_l^C + \Delta\tau^R \varpi_l^R + \Delta\tau_s^A \varpi_l^A}{\Delta\tau_s^C + \Delta\tau^R + \Delta\tau_s^A} \qquad (23)$$

where ϖ_l^C, ϖ_l^R, and ϖ_l^A denote the expansion coefficients for the individual phase function for cloud particles, Rayleigh molecules and aerosols, respectively. Since the phase function is independent of gaseous absorption, the combined ϖ_l is constant over a given spectral absorption band. Once the single-scattering properties have been defined for a given g for each level, monochromatic radiative transfer calculations may be carried out, and the radiance for each spectral subinterval ($\Delta\nu = 50\text{cm}^{-1}$) can be obtained as the summation of the radiance component in the g-domain:

$$R = \sum_{i=1}^{30} R(g_i)\Delta g_i \qquad (24)$$

3.3.1.7 Radiative Transfer Model

Model structure and flow chart

The radiative transfer scheme is the adding-doubling method including full Stokes parameters developed by Takano and Liou (1989) for vertically inhomogeneous atmospheres. In an anisotropic medium, the single-scattering properties depend on the direction of the incoming light beam. Let the directions of the incoming and outgoing light beams be denoted by (μ', ϕ') and (μ, ϕ), respectively, where μ is the cosine of the zenith angle and ϕ the corresponding azimuthal angle. The scattering phase matrix $\boldsymbol{P}$ is a function of (μ, ϕ, μ', ϕ') and cannot be defined by the scattering angle Θ alone as in conventional radiative transfer. Moreover, the extinction and scattering cross sections vary with the direction of the incoming light beam (μ', ϕ').

Let the Stokes vector intensity $\boldsymbol{I}=(I, Q, U, V)$. Following Liou (1992), the general equation governing the transfer of diffuse solar intensity may be written in the form:

$$\mu\frac{d\boldsymbol{I}(\tau;\mu,\phi)}{d\tau} = \boldsymbol{I}(\tau;\mu,\phi) - \boldsymbol{J}(\tau;\mu,\phi) \qquad (25)$$

and the source function,

$$J(\tau;\mu,\phi) = \frac{1}{4\pi}\int_0^{2\pi}\int_{-1}^{1}P(\mu,\phi;\mu',\phi')I(\tau;\mu',\phi')d\mu'd\phi' \tag{26}$$

$$+\frac{1}{4\pi}\ P(\mu,\phi;-\mu_0,\phi_0)\times\pi F_0\exp[-k(-\mu_0)\tau/\mu_0]$$

In Equation 26, μ_0 is the cosine of the solar zenith angle, ϕ_0 the corresponding azimuthal angle, and -μ_0 denotes the downward solar incident direction. The first and second terms on the right-hand side represent contributions from multiple scattering and single scattering of the direct solar intensity, respectively.

The multiple scattering problem is solved by means of the adding-doubling principle for radiative transfer. We define the reflection matrix $R(\mu,\phi,\mu',\phi')$ and transmission matrix $T(\mu,\phi,\mu',\phi')$ for radiation from above in the forms:

$$I_{out,top}(\mu,\phi) = \frac{1}{\pi}\int_0^{2\pi}\int_0^{1}R(\mu,\phi;\mu'',\phi'')I_{in,top}(\mu'',\phi'')\mu''d\mu''d\phi'' \tag{27}$$

$$I_{out,bottom}(\mu,\phi) = \frac{1}{\pi}\int_0^{2\pi}\int_0^{1}T(\mu,\phi;\mu'',\phi'')I_{in,top}(\mu'',\phi'')\mu''d\mu''d\phi'' \tag{28}$$

Likewise, for radiation from below, the reflection and transmission matrices are defined by:

$$I_{out,bottom}(\mu,\phi) = \frac{1}{\pi}\int_0^{2\pi}\int_0^{1}R*(\mu,\phi;\mu'',\phi'')I_{in,bottom}(\mu'',\phi'')\mu''d\mu''d\phi' \tag{29}$$

$$I_{out,top}(\mu,\phi) = \frac{1}{\pi}\int_0^{2\pi}\int_0^{1}T*(\mu,\phi;\mu'',\phi'')I_{in,bottom}(\mu'',\phi'')\mu''d\mu''d\phi'' \tag{30}$$

To proceed with the adding principle for the radiative transfer in an anisotropic medium, we shall utilize the reflection and transmission matrices defined in Equations 27 through 30 and consider an infinitesimal layer with a very small optical depth $\Delta\tau$, say 10^{-8}. Since the optical depth is so small, only single scattering takes place within the layer. From the fundamental equations for radiative transfer, the analytic solutions for reflected and transmitted intensities undergoing single scattering may be derived. Subject to the condition that $\Delta\tau \to 0$, we find:

$$R(\mu,\phi;\mu',\phi') \approx \frac{\Delta\tau}{4\mu\mu'}\varpi P(-\mu,\phi;\mu',\phi') \tag{31}$$

$$T(\mu,\phi';\mu',\phi') \approx \frac{\Delta\tau}{4\mu\mu'}\varpi P(-\mu,\phi;-\mu',\phi') \tag{32}$$

$$R*(\mu,\phi;\mu',\phi') \approx \frac{\Delta\tau}{4\mu\mu'}\varpi P(\mu,\phi;-\mu',\phi') \tag{33}$$

$$T*(\mu,\phi;\mu',\phi') \approx \frac{\Delta\tau}{4\mu\mu'}\varpi P(\mu,\phi;\mu',\phi') \tag{34}$$

Consider now two layers denoted by subscripts *a* and *b*, where layer *a* is on top of layer *b*. Let their optical depths be τ_a and τ_b. Following the conventional adding principle for radiative transfer in an isotropic medium, but with modifications to account for the dependence of the optical properties on the incoming direction, the procedure for computing the reflection and transmission matrices for the composite layer may be described by the following equations:

$$Q_1 = R_a^* R_b \tag{35}$$

$$Q_n = Q_1 Q_{n-1} \tag{36}$$

$$S = \sum_{n=1}^{M} Q_n \tag{37}$$

$$D = T_a + S\exp[-\tau_a/\mu_0] + ST_a \tag{38}$$

$$U = R_b \exp[-\tau_a/\mu_a] + R_b D \tag{39}$$

$$R_{a,b} = R_a + \exp[-\tau_a/\mu]U + T_a^* U \tag{40}$$

$$T_{a,b} = \exp[-\tau_b/\mu]D + T_b \exp[-\tau_a/\mu_0] + T_b D \tag{41}$$

In these equations, the product of two functions implies an integration over the appropriate solid angle so that all possible multiple scattering contributions are accounted for. For example:

$$R_a^* R_b(\mu,\phi;\mu',\phi') = \frac{1}{\pi}\int_0^{2\pi}\int_0^1 R_a^*(\mu,\phi;\mu'',\phi'')R_b(\mu'',\phi'';\mu',\phi')\mu'' d\mu'' d\phi'' \tag{42}$$

The number *M* in Equation 37 is selected according to the convergence of the series, and varies from 5 to 12 in the present calculations. The exponential terms in the adding equations are the direct transmission through layer a or b without scattering. The total transmission for the combined layer is the sum of the diffuse transmission $T_{a,b}$ and the direct transmission $\exp[-(\tau_a+\tau_b)/\mu_0]$ in the direction of the solar zenith angle θ_0.

In numerical computations, it is economical to set $\tau_a = \tau_b$. This is referred to as the doubling method. We start with an optical depth $\tau \approx 10^{-8}$ and use Equations 31 through 34 to compute the reflection and transmission matrices. Equations 35 through 41 are subsequently employed to compute the reflection and transmission matrices for an optical depth of 2τ. The computations using these equations are repeated until the desired optical depth is obtained.

We divide the model vertical domain into 51 layers (Δp = 20mb for each layer except for the bottom layer, where Δp = 13mb). The doubling procedures are applied to each layer to obtain the layer reflection and transmission functions. Subsequently, the adding procedures are applied to the 51 layers to obtain the radiance at the top of atmosphere. For wavelengths between 3.5 and 5µm, we take into account the thermal emission contributions in the solar flux transfer by adding the emission part $(1 - \varpi)\pi B_\nu(T)$, to the adding/doubling method in a manner described in Takano and Liou (1993), where ϖ is the single-scattering albedo and $B_\nu(T)$ is the Planck function for a given layer temperature T. The thermal emission part, although small, has not been accounted for previously in broadband solar flux calculations and could be a significant energy source in the upper part of the atmosphere.

The input parameters required to drive the LBLE solar radiation model include the solar insolation; spectral band wavenumbers of interest; solar and viewing zenith angles; the relative azimuthal angle; spectral surface albedos and emissivities; atmospheric temperature, humidity; and aerosol profiles; cloud phase; and cloud top and base altitudes. Figure 7 shows the flow diagram of the radiative transfer model developed for application to cloud remote sensing using VIIRS channel radiances. We first compile the spectral solar constant for 0.672, 1.24, 1.61, 2.25 and 3.7µm VIIRS channels. The LBLE includes the options of using the detailed solar irradiance data given by Thekaekara (1976) (solar constant=1353 W/m^2), Kneizys *et al.,* (1988) (LOWTRAN 7 solar constant=1380 W/m^2) or Anderson *et al.* (1995) (MODTRAN solar constant) averaged over appropriate spectral resolutions. We then generate the gaseous absorption line parameters from the updated HITRAN-1996 database for 0.672, 1.61, 2.1, 3.7 and 10.7625µm VIIRS channels.

Radiative Transfer Flow Diagram For Remote Sensing Application
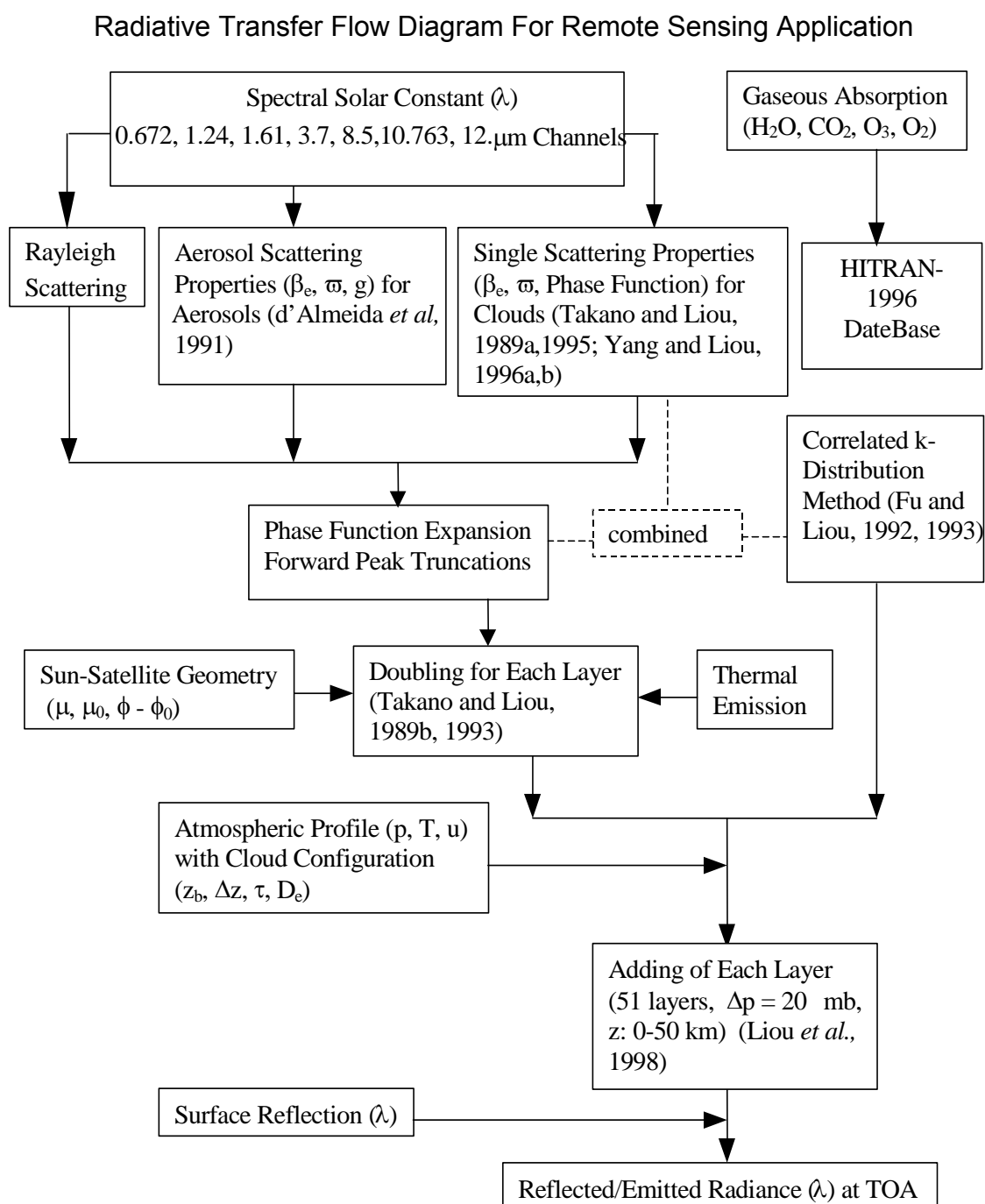
Figure 7. Flow Diagram of the Computation of TOA Radiance for Application to Cloud Remote Sensing using VIIRS Channels.

The correlated k-coefficients for H_2O covering the spectral region from 2,000 to 21,000cm^{-1} (0.5-5μm) are determined based on the methodology developed by Fu and Liou (1992) in which a number of temperatures and pressures are used. The correlated k-coefficients for the 2.0 and 2.7μm CO_2 bands are also derived, in which overlaps between H_2O and CO_2 lines are accounted for by using the multiplication rule. Absorption due to O_3 and O_2 bands is also included in the model based on Beer's Law (Liou, 1992). In addition, we have compiled the single-scattering properties of six typical aerosol types provided in d'Almeida *et al.* (1991) in connection with the LBLE model. In the present work, we use the rural aerosol model with 23 km visibility at the surface, which is the same as the default aerosol model in MODTRAN. At this point, the entire solar spectrum is divided into a total of 380 intervals, each of which is 50cm^{-1} wide. For each spectral interval, the inverse of the cumulative probability function $k(g)$ is evaluated at 30 g values, where $0<g<1$.

We then compute single-scattering parameters of air molecules, aerosol and cloud particles. We also construct the table of correlated-k coefficients. The resulting single-scattering parameters, cumulative k-distribution functions, phase functions and auxiliary data were combined as described in section 3.3.1.6 and input into the radiative transfer program.

Intercomparisons with results from MODTRAN

Over the years, a hierachy of fast radiative transfer models have been developed by the Air Force Research Laboratory (previously the Air Force Geophysics Laboratory), including LOWTRAN 5-7 (Kneizys *et al.*, 1988; Isaacs *et al.*, 1986, 1987), FASCODE and MODTRAN. At present, MODTRAN is the most advanced narrow-band radiative transfer program for computing transmittances in cloudless atmospheres. MODTRAN covers the spectral range from 0 to 50,000 cm^{-1} (~0.2-∞ μm) with flexible spectral resolution between 50cm^{-1} and 2cm^{-1} (Berk *et al.*, 1989). The latest version of MODTRAN (version 3.7) maintains the capability of the older versions. Several atmospheric temperature, humidity, ozone and aerosol (haze) profiles are built into the radiative transfer model. The default atmospheric profiles include tropical, mid-latitude summer, mid-latitude winter, sub-arctic summer, sub-arctic winter and the 1976 US Standard atmosphere. The default aerosol models include rural, maritime, urban , tropospheric (humidity dependent) and desert (wind dependent) models. Band model parameters based on HITRAN line data for twelve atmospheric molecular species (H_2O, CO_2, O_3, N_2O, CO, CH_4, O_2, NO, SO_2, NO_2, NH_3 and HNO_3) are included in the model (Kneizys *et al.,* 1988).

Larsen (1994) replaced the two-stream multiple scattering computations in MODTRAN with a modified version of the Discrete Ordinate Radiative Transfer (DISORT) Model. DISORT is a state-of-the-art, user-friendly discrete ordinate algorithm for radiative transfer in vertically inhomogeneous, non-isothermal, plane-parallel media (Stamnes *et al.*, 1988). It considers scattering, absorption, emission by particles as well as incident radiative sources at boundaries. Given cloud optical properties for each layer, DISORT can generate angular dependent radiance and radiative flux profiles within the cloud.

Although MODTRAN can produce spectrally high-resolution clear radiance with excellent accuracy and DISORT can generate reliable cloud radiance at any angle, the present

combination of MODTRAN with DISORT (MD) is less than ideal. In the original MODTRAN multiple scattering program, azimuthally independent source functions are computed by the two-stream method. These source functions are then substituted into the integrated form of the radiative transfer equation to obtain the radiance distribution. Thus the resulting radiance distribution is also azimuthally independent. The MD program still follows this approach. That is, instead of using source functions from the two-stream radiative transfer scheme built into the MODTRAN, MD uses DISORT-generated azimuthally independent source functions to compute azimuthally independent radiance distribution. Effects of this model artifact can be seen from the following comparison of clear and cloudy radiances from the LBLE and the MODTRAN/MD.

To compare the performance of the LBLE with the MD, we first compare the clear radiance generated by the two models. Figure 8 shows the geometry of the sun and the sensor with respect to the target along with the specification of angular parameters. In the planned NPOESS afternoon orbit, the sun is always to the west of the target, while the VIIRS sensor can be either to the east or to the west of the target. The angular parameters can be derived from simulated orbital information.

Sun-Satellite Geometry

θ_o = solar zenith angle
ϕ_o = solar azimuthal angle
θ = sensor zenith angle
ϕ = sensor azimuthal angle
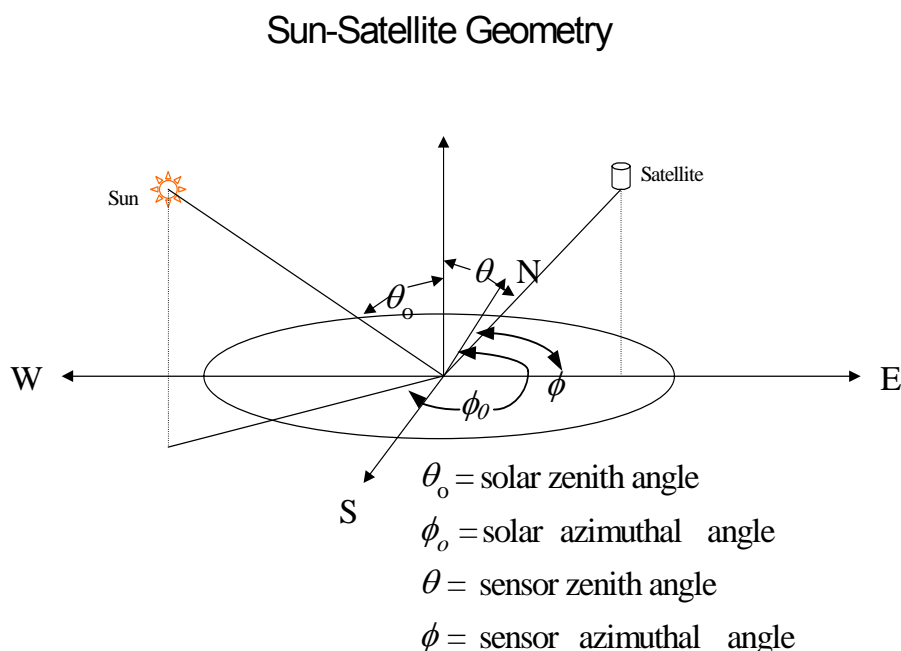
Figure 8. Sun Satellite Geometry.

Table 3 shows the comparison of 0.672μm clear and haze radiances from the LBLE model (denoted as UCLA) and from the MODTRAN/MD model for various sun-sensor geometries, including high-sun, low-sun, nadir-sensor, and off-nadir-sensor configurations. The terms "clear" and "haze" mean without and with the effects of background aerosols, respectively. In general, radiance from the LBLE model agrees with the MD radiance. For the high-sun cases (1, 3, 5), the differences are less than 10 percent. For the low-sun cases (2, 4, 6), the

differences are larger but are still less than 15 percent. When the sun is low, reflection due to aerosol scattering is stronger, so that the error in the azimuthally independent MD radiance increases. Similarly, for the same solar zenith angle, the differences for the off-nadir cases (3-6) are generally larger than those for the nadir case (1 and 2) due to errors caused by the assumption of azimuthally independent scattering in the MD calculations. For the off-nadir cases, the differences are smaller for the sensor at forward-scattering angles ($\Delta\phi > 90^o$) than at back-scattering angles ($\Delta\phi < 90^o$).

Table 3. Comparison of the 0.672 m Clear and Haze Radiances from the LBLE Model (UCLA) and the MODTRAN/MODTRAN-DISORT Model for Various Sun-Sensor Geometries including High-Sun, Low-Sun, Nadir-Sensor and Off-Nadir-Sensor

Case No.	Sky	Clear			Haze		
		UCLA	MODTRAN	% Diff.	UCLA	MODTRAN	% Diff.
1	$\theta_o = 32°$ $\theta = 0°$	1.44200	1.39506 (1.40846) † [1.34247] @	-3.25 (-2.33) [-6.90]	1.67600	1.67338 (1. 72751) [1.63477]	-0.16 (3.07) [-2.46]
2	$\theta_o = 75°$ $\theta = 0°$	0.51353	0.49331 (0.50555)	-3.94 (-1.55)	0.80821	0.72738 (0.79451)	-10.00 (-1.70)
3	$\theta_o = 32°$ $\theta = 40°$ $\cong \phi = 136°$	1.57441*	1.481337	-5.91	1.88152	1.92653	2.39
4	$\theta_o = 75°$ $\theta = 40°$ $\cong \phi = 168°$	0.735682	0.677275	-7.93	0.976508	1.059228	8.47
5	$\theta_o = 32°$ $\theta = 40°$ $\cong \phi = 0°$	1.36383	1.302619	-4.49	1.92005	1.756079	-8.54
6	$\theta_o = 75°$ $\theta = 40°$ $\cong \phi = 0°$	0.612285	0.596909	-2.51	1.67525	1.4494	-13.48

* : in $W/m^2/sr$; @: Numbers in brackets are based on MODTRAN results from TASC

†: Numbers in parentheses are based on DISORT 8-stream source functions

Configurations.

Table 4 shows the comparison of the 3.7μm clear and haze radiance from the LBLE and the MODTRAN/MD model for various sun-sensor geometries, including high-sun, low-sun, and nadir-sensor configurations. The differences in the solar component are less than 15 percent. Differences in the thermal IR component are less than 0.4 percent. For total radiance, the differences are less than 4 percent, because the IR component dominates the total radiance. In addition, since the fraction of the solar component in the total radiance decreases as the solar zenith angle increases, the total radiance differences are less for the low-sun case than for the high-sun case. Finally, Table 5 shows the comparison of 10.76μm

clear and haze radiances from the LBLE model and the MODTRAN/MD model for the nadir-sensor case. The differences are less than 5 percent for both clear and haze cases. Overall, it is demonstrated that the LBLE clear radiance compares reasonably well with the MD radiance, though small errors exist due to neglecting azimuthal dependence in the computation of the aerosol scattering component.

Table 4. Comparison of the 3.7μm Clear and Haze Radiances from the LBLE Model (UCLA) and the MODTRAN/MODTRAN-DISORT Model for Various Sun-Sensor Geometries including High-Sun, Low-Sun and Nadir-Sensor Configurations.

Component	Case No.	Sky	Clear			Haze		
			UCLA	MODTRAN	% Diff.	UCLA	MODTRAN	% Diff.
Solar	1	$\theta_o = 32°$ $\theta = 0°$	0.02327*	0.02140 (0.02140)†	-8.04 (-8.04)	0.02331	0.02170 (0.02610)	-6.91 11.97
	2	$\theta_o = 75°$ $\theta = 0°$	0.006321	0.005400 (0.00540)	-14.57 (-14.57)	0.006548	0.005600 (0.005600)	-14.48 -14.48
Thermal IR	3	$\theta_o = 32°$ $\theta = 0°$	0.04354	0.04340 (0.04350)	-0.32 (-0.09)	0.04344	0.04330 (0.04330) [0.04321]	-0.32 (-0.32) -0.53
	4	$\theta_o = 75°$ $\theta = 0°$	0.04354	0.04340 (0.04350)	-0.32 (-0.09)	0.04344	0.04330 (0.04330)	-0.32 (-0.32)
Total	5	$\theta_o = 32°$ $\theta = 0°$	0.06681	0.06480 (0.06490) [0.064469]	-3.01 -2.86 [-3.50]	0.06675	0.06500 (0.06940) [0.064429]	-2.62 3.97 [-3.48]
	6	$\theta_o = 75°$ $\theta = 0°$	0.04986	0.04940 (0.04890)	-0.92 (-1.93)	0.04999	0.04890 (0.04890)	-2.18 (-2.18)

* : in W/m^2/sr

†: Numbers in parentheses are based on DISORT 8-Stream source functions

Table 5. Comparison of the 10.76μm Clear and Haze Radiances from the LBLE Model (UCLA) and the MODTRAN/MODTRAN-DISORT Model for Various Sensor Geometries including Nadir-Sensor and Off-Nadir-Sensor Configurations.

Case No.	Clear			Haze		
	UCLA	MODTRAN	% Diff.	UCLA	MODTRAN	% Diff.
1 ($\theta = 0$ º)	7.90516	7.56000	-4.37	7.88450	7.5489	-4.26
2 ($\theta = 40$ º)	7.86735	----------	-------	7.83776	------------	--------

We then compare the cirrus cloudy radiance generated by the two models. The 1976 US Standard Atmosphere is assumed. A cirrus cloud is prescribed to be at 9-10km. Figure 9 shows the contour plot of 0.672μm reflectance and radiance for various combinations of cirrus cloud optical depths and mean effective sizes for a high-sun angle (θ_o=32º) and nadir viewing. It is obvious that the radiance/reflectance depends strongly on optical depth but weakly on the mean effective size. For optical depths between 0 and 8, the reflectance varies between 0 and 0.5, and the radiance varies between 0 and 12 $Wm^{-2}sr^{-1}$. The computed radiance range can help determine maximum and minimum values in the design of the VIIRS sensor measurement range. Figure 10 shows the contour plot of 3.7μm total (solar + thermal) reflectance and radiance for the same combination of cirrus cloud optical depths and mean effective sizes for a high-sun angle ($\theta_o = 32º$) and nadir viewing. For small mean effective sizes, the radiance/reflectance is virtually independent of optical depth, but for larger mean effective sizes, the radiance/reflectance is nearly independent of mean effective size. For mean effective size less than 40μm, the total radiance varies between 0.04 and 0.08 $Wm^{-2}sr^{-1}$. For mean effective size larger than 40μm, the total radiance varies between 0.01 and 0.06 $Wm^{-2}sr^{-1}$.

Figure 11 shows contour plots of the 0.672μm and 3.7μm radiance percentage differences between LBLE and MD results. For the 0.672μm radiance, differences are generally independent of mean effective sizes, but increase with increasing optical depth. For optical depths greater than 4, the differences exceed 40 percent. For the 3.7μm radiance, differences are less than 10 percent for optical depths less than 2. However, for mean effective size larger than 50 μm, the differences increase with the optical depth. Figure 12 shows contour plots of the 10.76 μm MD radiance and the differences between LBLE and MD radiance. The radiance decreases with increasing optical depth. There is a weak dependence on the mean effective size. As in the cases of 0.672 μm and 3.7 μm, for optical depths greater than 2, the differences increase with optical depth up to about 30 percent. In summary, the above inter-comparison results of cirrus cloudy radiance show that MD radiances for optically thick clouds differ from the LBLE radiances by more than 10 percent

in general. Although such inter-comparisons have been done only for one cirrus cloud scenario, we expect that similar patterns of differences between LBLE and MD radiance will show up for other cirrus and water cloud scenarios. The inherent problem of neglecting the azimuthal dependence of radiance will cause the resulting radiance for optically thick clouds to be in large error in every case.

The above intercomparison of LBLE and MD results leads to the following conclusions. The MD, or a program based on a similar philosophy of assuming azimuthally independent scattering, is not feasible to be used as the radiative transfer model for the development of retrieval algorithms for inferring cloud optical depth and effective particle size. This is simply because the MD is defective in the treatment of multiple scattering and has not been used in any previous algorithm development for the retrieval of cloud optical and microphysical parameters. In addition, because the development of the present retrieval programs is closely coupled with the physically based LBLE, retrievals of cloud optical depth and effective particle size are expected to meet the EDR specification requirements only if VIIRS radiances are realistic (i.e., simulated with the LBLE). In fact, having recognized that retrievals of the cloud parameters must be properly coupled with a reliable forward radiative transfer program, established cloud retrieval algorithm development teams (e.g., King *et al.* at NASA Goddard Space Flight Center, Minnis *et al.* at NASA Langley Research Center and Rossow *et al.* at NASA Goddard Institute of Space Science) all have developed their own radiative transfer programs based on sound physical principles for the purpose of algorithm development and sensitivity studies. Therefore, it appears both scientifically justified and commercially advantageous that the LBLE should be used as the only radiative transfer model for the development of retrieval algorithms for inferring cloud effective particle sizes and optical depths.
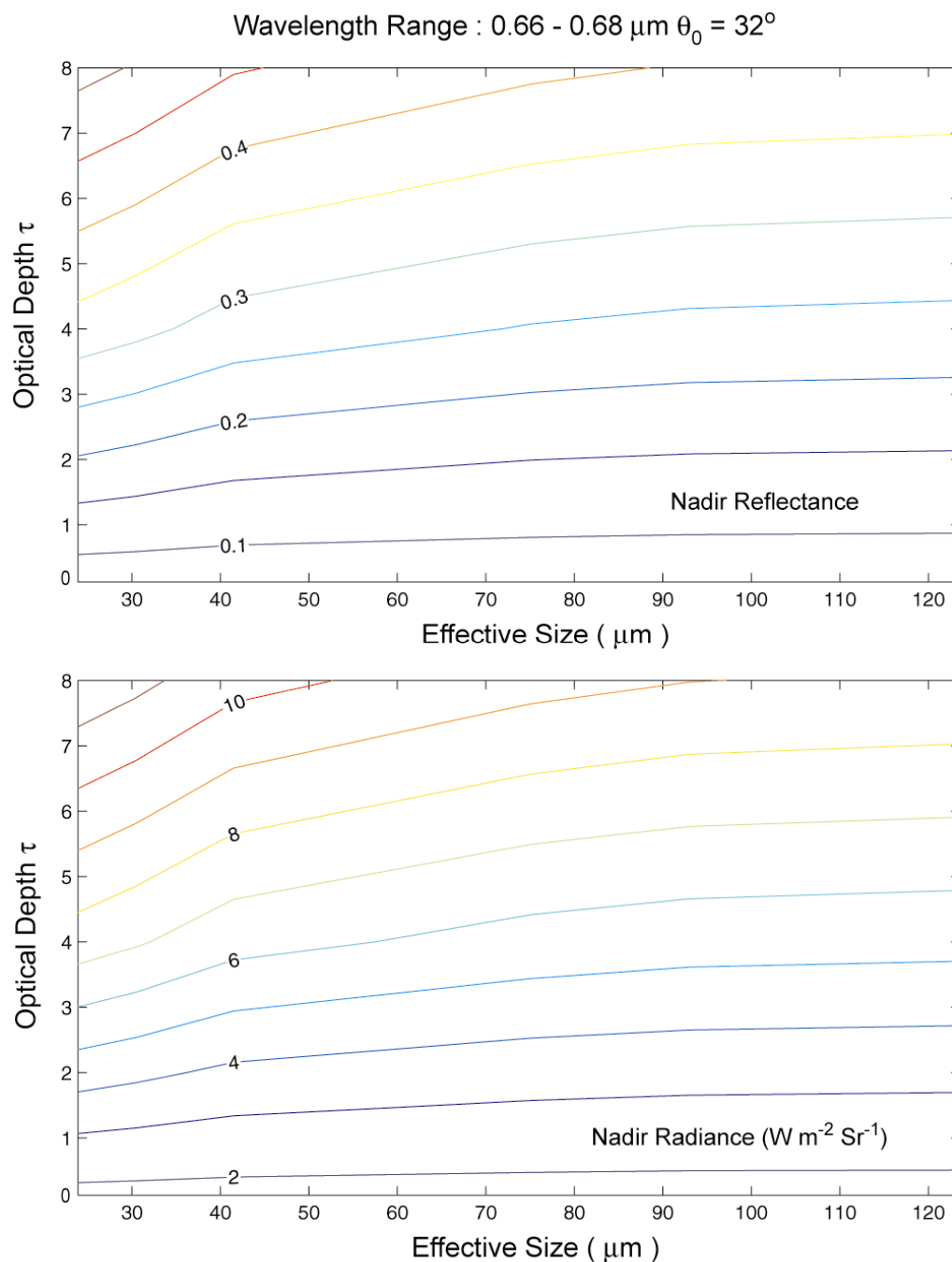
Figure 9. Contour Plot of the 0.672μm Reflectance (above) and Radiance (below) for Various Combinations of Cirrus Cloud Optical Depths and Mean Effective Sizes for High-Sun Angle (θ_o=32°) and Nadir Viewing.
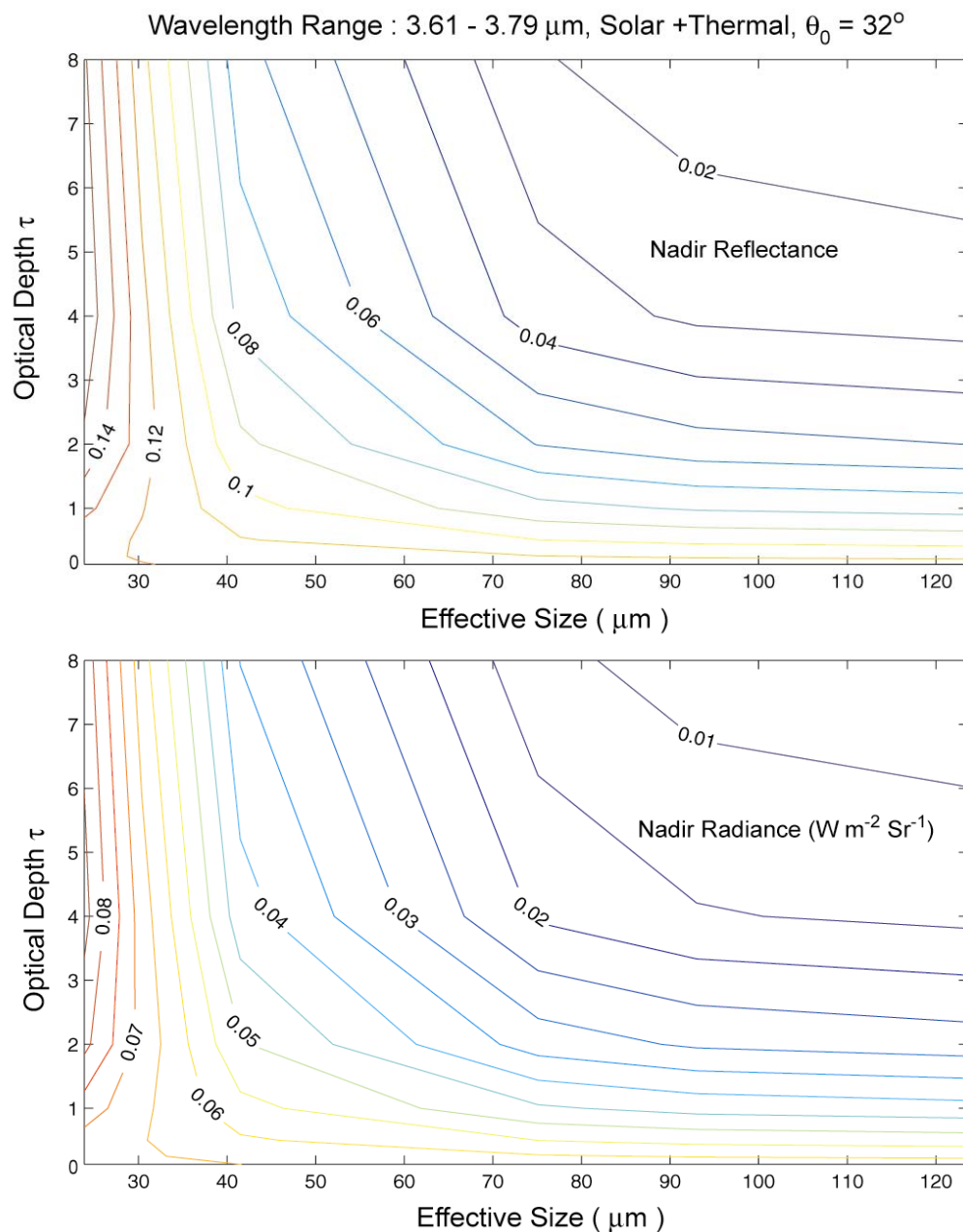
Figure 10. Contour Plot of the 3.7μm Total (Solar + Thermal) Reflectance (above) and Radiance (below) for the Same Combinations of Cirrus Cloud Optical Depths and Mean Effective Sizes for High-Sun Angle (θ_o=32°) and Nadir Viewing.

Percentage Differences between MODTRAN and UCLA
Radiative Transfer Codes ($\theta_0 = 32°$, $\theta = 0°$)
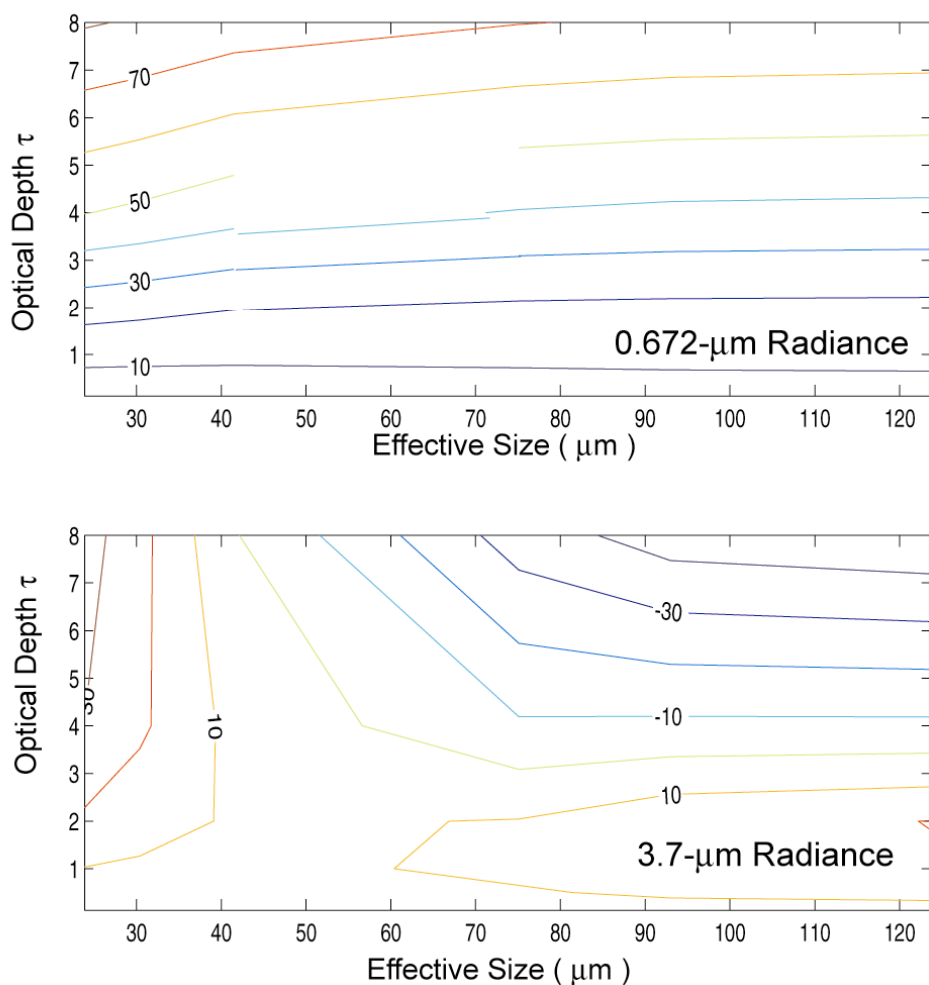
Figure 11. Contour Plot of the 0.672μm (above) and 3.7μm (below) Radiance Percentage Differences between LBLE and MODTRAN-DISORT.
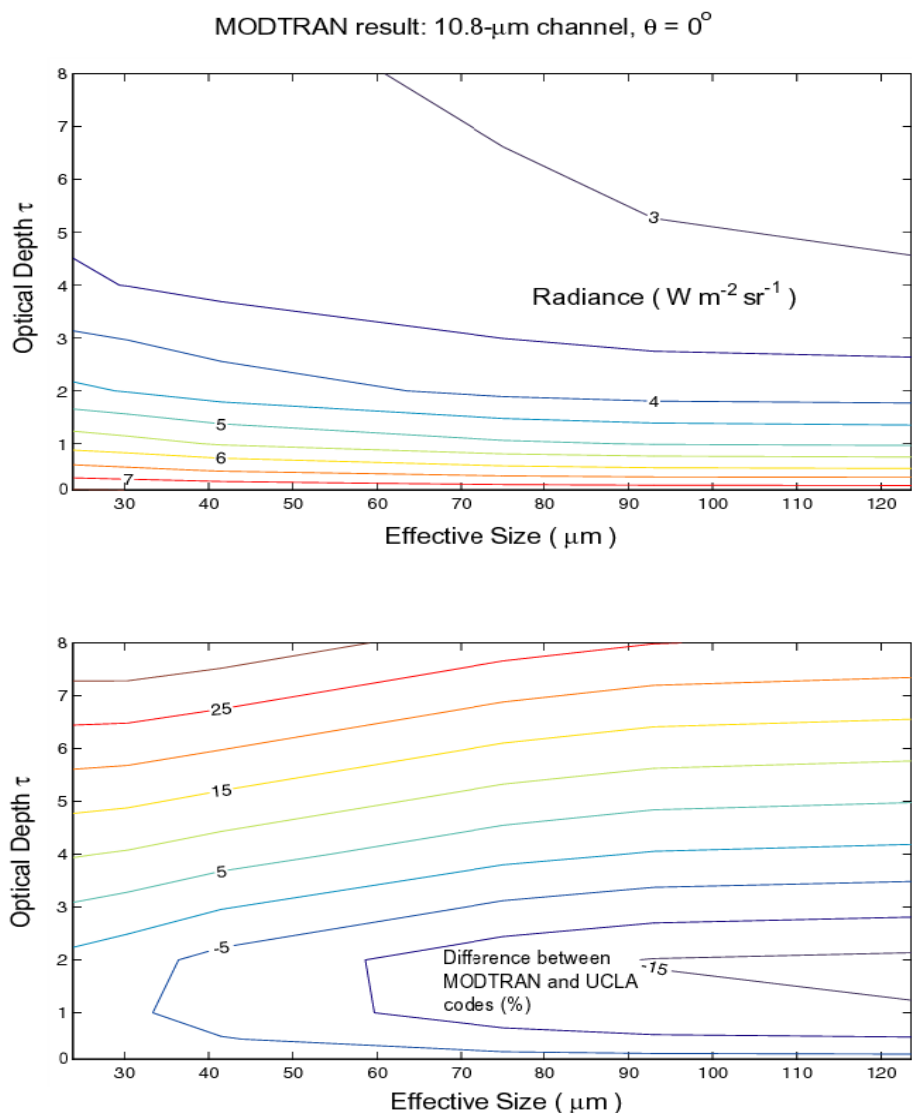
Figure 12. Contour Plots of the 10.76μm MODTRAN-DISORT Radiance (above) and Differences between LBLE and MODTRAN-DISORT Radiance (below).

3.3.2 Mathematical Description of the Algorithms

3.3.2.1 Retrieval of Ice Cloud Parameters

Figure 13 shows the flow chart of the cirrus cloud retrieval program. Once the cirrus cloud pixels are identified, three retrieval programs are applied to nighttime and daytime data. For the nighttime retrieval, the IR cloud CTT retrieval program (C1), uses the VIIRS 8.6 and 12µm radiances to infer the cirrus cloud temperature, and the IR cloud COP retrieval program (C2) uses the VIIRS 10.76 mm radiances to retrieve visible optical depth and mean effective size. For the daytime retrieval, however, the solar ice cloud retrieval algorithm (C3), using the VIIRS 1.61 and either 0.672 or 1.24µm reflectances, is employed to infer cirrus cloud optical depth and mean effective size.   With mean effective size as input, the k-ratio of M14 and M16 is calculated and input into the IR cloud CTT program (C1) to derive cloud-top temperatures.
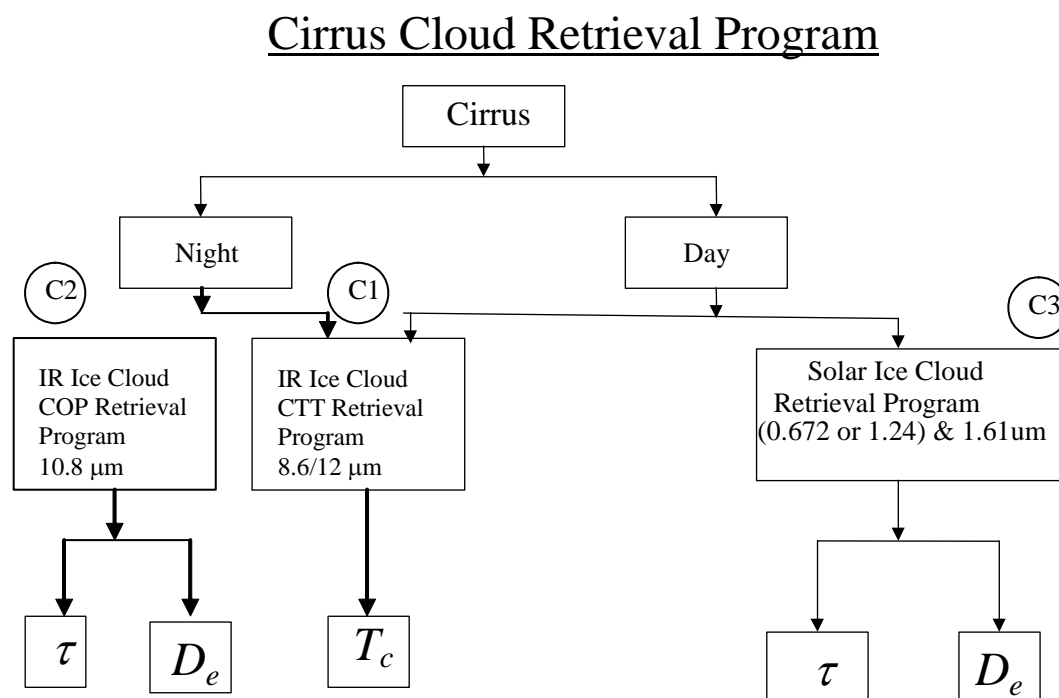
Figure 13. Flow Chart for the Cirrus Cloud Retrieval Program.

Nighttime IR Cirrus Cloud Retrieval Algorithm

The retrieval program for deriving cirrus temperature, mean effective ice crystal size and optical depth from the upwelling radiance of VIIRS cloud retrieval channels follows the principles of the dual-IR-channel technique presented in Liou *et al*. (1990). The VIIRS 3.7, 8.6 m, 10.76µm, and 12 m radiances have been selected for use. A major advantage of using these three channels for cirrus retrievals is that the radiance of these window bands is less affected by the presence of water vapor than the other bands. The retrieval program is based on the numerical solution of three groups of equations, which are derived from radiative, radiative-microphysical, and microphysical parameterizations.

a. Radiative parameterizations

From the theory of radiative transfer, we may express the upwelling radiance at TOA for the 3.7µm, 8.6 µm, 10.8 m, and 12 µm (VIIRS M12, M14, M15 and M16 respectively) channels over a cirrus cloudy atmosphere in terms of the cirrus cloud-top temperature, T_c, and emissivities, $\varepsilon_{1,2}$, as follows:

$$R_i = (1 - \varepsilon_i) R_{ai} + \varepsilon_i B_i(T_c), \qquad i = 12, 14, 15, 16 \qquad (43)$$

where R_{ai} denote the upwelling radiance reaching the cloud base for the two spectral bands and $B_i(T_c)$ are the respective Planck functions at T_c. The first term on the right-hand side of Equation 43 represents the contribution of the transmitted radiance from below the cloud. The second term denotes the emission contribution from the cloud itself. The emission by water vapor above the cirrus cloud has been neglected. The effects of cloud reflectivity, which are generally less than 3 percent of the incident radiance based on exact radiative transfer calculations, have also been neglected.

In order to solve Equation 43 for $B_{16}(T_c)$ and k_{15}/k_{12}, we relate $B_{14}(T_c)$ with $B_{16}(T_c)$, and $B_{12}(T_c)$ with $B_{15}(T_c)$, correlate ε_{14} vs. ε_{16}, and ε_{15}, and statistically determine the clear radiance R_{ai}. First, we compute the Planck functions $B_i(T_c)$ for all four channels, taking into account the filter functions of these channels. Look-up tables of Planck function are built in 0.1K intervals within the range of Tc from 150 to 350 K.

Then, we investigate the relationship between the emissivities for the M14 and M16 channels. From radiative transfer calculations and following the approach proposed by Liou *et al*. (1990), we may parameterize cirrus emissivities for all four wavelengths in terms of the visible optical depth, τ, in the form:

$$\varepsilon_i = 1 - \exp(-k_i \tau), \qquad i = 12, 14, 15, 16 \qquad (44)$$

The exponential term represents the effective transmissivity. The parameters k_i represent the effective extinction coefficients for the two channels accounting for effects of multiple scattering. All k_i are smaller than 1 because the effect of multiple scattering is smaller with IR than visible. Thus the products $k_i\tau$ may be considered as the effective optical depth that would yield the same emissivity values for the pure absorption conditions at these

wavelengths. By eliminating τ from Equation 43 for M14 and M16, and M12 and M15, we obtain

$$(1-\varepsilon_{14})^{1/k_{14}} = (1-\varepsilon_{16})^{1/k_{16}} . \qquad (45a)$$

$$(1-\varepsilon_{12})^{1/k_{12}} = (1-\varepsilon_{15})^{1/k_{15}}$$
(45b)

Equations 46(a) and 46(b) correlate ε_{14} - ε_{16} and ε_{12} - ε_{15} directly. A further combination of Equations 43 and 45a-b leads to:

$$[(R_{16}-B_{16}(T_c))/R_{a16}-B_{16}(T_c))]-[(R_{14}-B_{14}(T_c))/(R_{a14}-B_{14}(T_c))]^{k_{16}/k_{14}} = 0 , \qquad (46a)$$

$$[(R_{15}-B_{15}(T_c))/R_{a15}-B_{15}(T_c))]-[(R_{12}-B_{12}(T_c))/(R_{a12}-B_{12}(T_c))]^{k_{15}/k_{12}} = 0 . \qquad (46b)$$

b. Radiative-microphysicl parameterizations

We investigate the dependence of k_{15}/k_{12} on the particle size distribution and optical depth based on radiative transfer calculations by using the six ice crystal size distributions given in Section 3.3.1.1. A reasonable range of optical depth for these size distributions has been used. As an initial approximation, we may take k_{12} and k_{15} as independent of the optical depth. However, for more accurate retrieval of cirrus cloud parameters, we need to consider the dependence of k_{15}/k_{12} on the optical depth. Generally, k_{15}/k_{12} decreases as D_e increases. For a small D_e (~20μm), k_{15}/k_{12} is close to 2. This is primarily because the single-scattering albedo is larger for the 3.7μm wavelength (~0.8) than that for the 10.76μm wavelength (~0.4), which implies that more scattering is associated with the former wavelength. For D_e > 100μm, k_{15}/k_{12} approaches 1 for the following reasons. First, the extinction coefficients are approximately the same for the two wavelengths because of large-size parameters in which the geometric optics limit is valid. Second, the single-scattering albedos are also approximately the same for these wavelengths because substantial absorption occurs within large ice crystals. This implies that only the diffracted and externally reflected light contributes to the scattering processes. For obtaining the initial guesses, k_{15}/k_{12} can be expressed in terms of $1/D_e$ in the form:

$$k_{15}/k_{12} = \sum_{n=0}^{2} b_n D_e^{-n} \qquad (47)$$

where the coefficients b_n are determined from a second-order least square method using the radiance tables. In the retrieval scheme, however, b_n are further expressed as third-order polynomial functions of τ:

$$b_n(\tau) = \sum_{m=0}^{3} d_{nm} \tau^m \qquad (48)$$

where the coefficients d_{nm} are provided in Table 6.

Table 6. Coefficients (d_{nm}) to compute k_{15}/k_{12} from Optical Depth and Ice Cloud Effective Particle Size.

	US Standard Atmosphere			Tropical Atmosphere			Polar Atmosphere		
	n=2	n=1	n=0	n=2	n=1	n=0	n=2	n=1	n=0
m=3	0.4658	-0.0507	0.0003	0.2034	-0.0081	0.0002	0.1884	-0.012	0.0001
m=2	-9.0524	1.1868	-0.0081	-5.9222	0.3412	-0.0026	-4.1615	0.2307	-0.0036
m=1	84.456	-10.756	0.0653	53.787	-3.4981	0.0159	48.18	-3.1788	0.0155
m=0	-314.37	55.795	0.7551	-362.83	36.322	0.9342	-353.63	35.173	0.9142

Based on radiative transfer simulations of M14 and M16 radiances, we found that k_{16}/k_{14} is insensitive to particle size as shown in the following linear relationship between k_{16}/k_{14} and D_e:

$$k_{16}/k_{14} = b_0' + b_1' D_e. \qquad (49)$$

Where $b_0' = 1.596$ and $b_1' = 0.004$ [1/micron]

c. Microphysical parameterizations

A direct determination of D_e from the data that are available from the present satellite thermal infrared radiometers appears to be very difficult, if not impossible. However, we may relate D_e to the cloud temperature through appropriate observations. Based on a large number of cirrus microphysical data collected by optical probes during flights over midlatitudes, Heymsfield and Platt (1984) have suggested that ice crystal size distribution can be represented by a general power form as follows:

$$n(L) = \begin{cases} A_1 L^{b_1}(IWC) & L \leq L_0 \\ A_2 L^{b_2}(IWC) & L > L_0 \end{cases} \qquad (50)$$

where $L_0 = (A_2 / A_1)^{1/b_1 - b_2}$, IWC is the ice water content and $A_{1,2}$ and $b_{1,2}$ are temperature dependent empirical coefficients determined from the measured data. Heymsfield and Platt (1984) have shown that for a given temperature, values of $A_{1,2}$, $b_{1,2}$ and IWC may be parameterized in terms of temperature in the range of $-20^\circ C$ to $-60^\circ C$ (Liou, 1992). Based on this parameterization, the mean $n(L)$ is also a function of temperature. Moreover, aircraft and laboratory measurements indicate that the width D and the length L of a hexagonal ice crystal are related (e.g., Auer and Veal, 1970) in which a parameterization relation can be developed for the two. Thus, with the functional form of $n(L)$ determined, the temperature-dependent mean effective size $<D_e>$ can be obtained, where the bracket denotes the mean value for a given temperature. Subsequently, we perform a least squares polynomial fitting to relate $<D_e>$ to T_c in the form:

$$<D_e> = \sum_{n=0}^{3} c_n (T_c - 273)^n \qquad (51)$$

where T_c is in K, $c_0 = 326.3$, $c_1 = 12.42$, $c_2 = 0.197$ and $c_3 = 0.0012$. Equation 51 was used for cloud retrievals using AVHRR data (Ou *et al.*, 1993; Rao *et al.*, 1995).

The retrieved D_e based on Equation 51 may be in error due to uncertainties in $A_{1,2}$, $b_{1,2}$ and IWC. To improve the accuracy of the retrieved mean effective size, we modify the value of D_e according to the following procedures. Let D_e be the modified value of $<D_e>$. We assume that D_e and IWC have the following relationship based on dimensional analysis:

$$D_e \propto (IWC)^{1/3} \qquad (52)$$

Observational evidence (Heymsfield and Platt, 1984) shows that:

$$<D_e> \propto <(IWC)>^{1/3} \qquad (53)$$

where $<IWC>$ is the temperature-dependent mean value of IWC, derived from observations. According to Liou (1992), $<IWC>$ can be parameterized in terms of T_c as follows:

$$<IWC> = \exp\{-7.6 + 4 \exp[-0.2443 \times 10^{-3}(253 - T_c)^{2.445}]\} \quad \text{for } T_c < 253 \text{ K} \qquad (54)$$

The quantity IWC may be expressed by (Fu and Liou, 1993):

$$IWC = \tau / [\Delta z(\alpha + \beta/D_e)] \qquad (55)$$

where τ is the visible optical depth, Δz is the cloud thickness and α and β are empirical constants. Δz is assumed to be known and is equal to 1 km. Combining Equations 53 through 56, we obtain:

$$D_e = c\{\tau / [\Delta z(\alpha + \beta/D_e)<IWC>]\}^{1/3}<D_e> \qquad (56)$$

where c is the combined proportional factor derived from the ratio of proportionality constants implied in Equations 52 and 53. Equation 56 is an implicit algebraic equation for D_e, which is also an implicit function of T_c and   . It has been verified using the balloon-borne replicator data collected on November 26 and December 5, 1991 during the FIRE-II IFO (Ou *et al.*, 1995).

The constant "c" and Δz are parameters needed to be specified.   However, using climatology data we had arrived the following values for Δz *at different ranges of Cloud top temperature (in Celsius)*:

$\Delta z = 1.37\ Km$ *for* $T_c\ > -10^o\ C$

    $= 0.725 - 0.065 * T_c$ *for* $-10^o\ C\ \geq\ T_c > -35^o\ C$

    $= 4.7 + 0.0456 * T_c$ *for* $-35^o\ C\ \geq\ T_c > -70^o\ C$

    $= 1.508\ Km$ *for* $T_c \leq\ -70^o\ C$

With the above specification for Δz, constant c = 1.0

d. Clear radiances

Finally, in order to solve Eq. (46b) for $B_4(T_c)$, and Eq. (46a) for k_2/k_1, the upwelling radiances reaching the cloud base, R_{ai}, must be known. We may approximate these radiance values by using the radiance measured from satellites in clear conditions because little water vapor is present above cirrus clouds. In the case of VIIRS data, each scan line spans ~3000 km. Because of the high resolution of the VIIRS pixels, it is likely that, over the large area scanned by the radiometer, some of the data points correspond to clear conditions. It follows that if we can identify the clear pixels, R_{ai} may be determined by a statistical method. We may select a scene and use the data within this scene to construct a two-dimensional histogram in the domains of $R_1 - R_2$ and $R_3 - R_4$ (Ri are sensor measured radiance as defined following Equation 43). The area of the scene should be large enough to contain a statistically significant amount of pixels, but, at the same time, this area should also be sufficiently small to guarantee homogeneity of the surface temperature and water vapor distributions within the scene. Usually, a 1° by 1° scene is adequate for the analysis. The radiance corresponding to the peak of the frequency distribution is assigned as the mean clear radiance. These clear radiances are then used as needed for all pixel-level processing within the scene area. In the algorithm sensitivity studies, the clear radiance was pre-determined using the LBLE program.

To determine clear radiances for an overcast scene, which can be identified based on VIIRS cloud mask results, a neighboring-scene technique is used. Moreover, because the resulting

distribution of clear radiances may still be un-realistically noisy, a smoothing routine based on the principle of spatial coherence method is added. Details of these additions are given in Appendix C

e. Solution Procedures

Figure 14 shows a schematic description of the solution procedures. Utilizing an estimated value of k_{16}/k_{14}, we solve Eq. (46a) for T_c using successive approximation method. Once the T_c is known, ε_i, and τ Can be calculated by Equations (43) and (44). Then k_{15}/k_{12} is calculated by Eq. (46b). Finally, we use Eqs. (47) and (56) to obtain $D_{e,\,k}$ abd $D_{e,\,m}$, respectively, and determine the output value of D_e based on the weighted sum of the two D_e quantities. This completes one cycle of iteration. The final results, T_c, τ and D_e are refined by updating the k_{16}/k_{14} with new D_e throught Equation 49. Analyses show that due to the insensitivity of k_{16}/k_{14} in D_e, the final results are obtained in 2 iterations.

Input VIIRS 3.7(M12) , 8.55(M14), 10.76 (M15) and 12 μm (M16) Radiances for Cloudy Pixels

Compute pixel-level CTT (T_c) using M14 and M16 radiances

Initial $k_{16}/k_{14} = 1.1$

$k_{16}/k_{14} = 1.596 - 0.004 * D_e$

$[(R_{16}-B_{16}(Tc)) / (R_{a16}-B_{16}(T_c))] - [(R_{14}-B_{14}(T_c)) / (R_{a14}-B_{14}(T_c))]^{k_{16}/k_{14}} = 0$

Compute τ, and D_e using M12 and M15 radiances

$R_{15} = (1 - \varepsilon_{15}) R_{a15} + \varepsilon_{15} B_{15}(T_c)$ -- for ε_{15}

$\varepsilon_{15} = 1 - exp(-k_{15} \tau / cos(\theta_{sen}))$ where $k_{15} = 0.52$ -- for τ

$[(R_{15}-B_{15}(Tc)) / (R_{a15}-B_{15}(T_c))] - [(R_{12}-B_{12}(T_c)) / (R_{a12}-B_{12}(T_c))]^{k_{15}/k_{12}} = 0$

$k_{15}/k_{12} = \sum_{n=0}^{2} b_n D_{e,k}^{-n}$

$D_{e,m} = c\{\tau / [\Delta z(\alpha + \beta/D_e)<IWC>]\}^{1/3} <D_e>$ -- for D_e

Update De

CTT converged

No

Yes

Figure 14. Flow Chart for the Nighttime IR Cirrus Retrieval Algorithm.

Solar Cirrus Cloud Retrieval Algorithm

During daytime, both a solar retrieval and a thermal-IR retrieval are performed. The solar algorithm (C3) must be run first such that the thermal IR k-ratio, k_{16}/k_{14} can be calculated from Equation 49. Then, the thermal-IR algorithm (C4) proceeds without the reflected solar contamination.

A generalized description of the solar cirrus cloud retrieval algorithm is as follows. For the daytime retrieval, the solar ice cloud retrieval program (C3) uses the VIIRS 1.61μm reflectance and either the 0.672μm (non-snow/ice surfaces) or 1.24μm (snow/ice surfaces) reflectance to infer the cirrus cloud optical depth and mean effective size. The retrieval program follows the principles of the dual-solar-channel technique presented in Nakajima and King (1990). Figure 15 illustrates the underlying principles behind the simultaneous determination of cirrus cloud optical depth and mean effective size from reflected solar radiation measurements. Preliminary calculations using the MAS 0.681, 1.617 and 2.139μm channels have been carried out. Radiative transfer calculations were performed for the six ice crystal size distributions described in section 3.3.1.1 using the LBLE. The results are displayed in two-dimensional reflectance diagrams (0.681–1.617μm and 0.681–2.139μm) for optical depths ranging from 0.5 to 16. Also shown are the results for water clouds having mean effective radii of 4
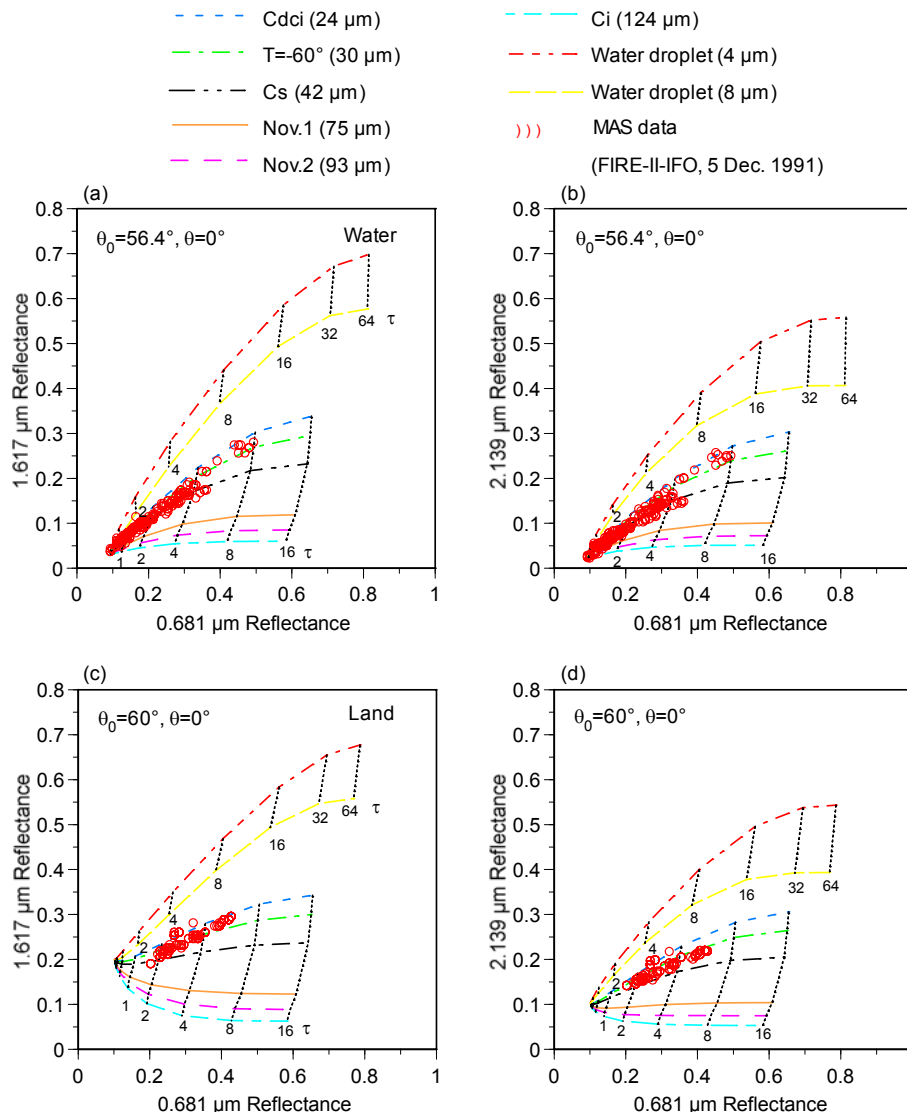
Figure 15. Display of the Correlation of MAS 0.681-1.617 m Reflectances Based on Radiative Transfer Calculations and MAS Data taken from FIRE-II IFO over Both Land and Water Surfaces. The calculations were performed for the six ice crystal size distributions presented in section 3.3.1.1 and for two water clouds with mean effective radii of 4 and 8 μm. The optical depth ( ) ranges from 0.5 to 64 for water cloud and 0.5-16 for ice cloud. Overlapped with the correlation curves are the MAS data obtained from FIRE-II-IFO on 5 December 1991. The data for the water surface were collected at 1636 UTC over the northern Gulf of Mexico. The land surface data were collected at 1923 UTC over eastern Oklahoma.

and 8μm, optical depths ranging 0.5 to 64 and MAS data obtained from FIRE-II-IFO on December 5, 1991. The top and bottom diagrams correspond to the cases for water and land surfaces, respectively. In the calculations, the effective surface albedos were

determined from the MAS reflectances over clear pixels that were identified using a scheme similar to the one developed by Ou *et al*. (1996).

The preliminary calculations illustrate the information content of optical depth and mean effective size in the MAS 0.681, 1.617 and 2.139μm reflectances. The nearly horizontal or diagonal curves are constant-D_e contours for the six ice crystal size distributions, while the nearly vertical dotted lines are the constant-τ contours for the selected optical depths. The underlying surface was assumed to be Lambertian. The minimum value of the reflection function at each wavelength corresponds to the reflection function of the underlying surface at that wavelength in the absence of an atmosphere. Display of the 0.681 and 1.617μm reflectance correlation shows that if the mean effective radius of a water cloud (stratus and cumulus) is less than about 10 μm and if the mean effective size of an ice cloud is larger than about 20 μm, a clear distinction can be made between the two in the correlation domain. Also noted is that the 0.681μm reflectance depends more strongly on optical depth than on particle size. However, the 1.617 and 2.139μm reflectances are primarily functions of particle size rather than optical depth. From the diagrams, as the optical depth increases, the constant-D_e contour lines gradually approach asymptotic values.

The MAS data were obtained from the flight missions during FIRE-II IFO. The case over water was taken at 1636 UTC, 5 December 1991, when ER-2 was flying over the northern part of the Gulf of Mexico near the southern coastal region of Louisiana. The case over land was taken at 1923 UTC, 5 December 1991, when ER-2 was flying over eastern Oklahoma. The data points indicate that the detected cirrus clouds appear to contain small ice particles with optical depths less than about 6. Larger optical depths indicate the possibility of cirrus overlying low clouds.

Figure 16 shows an algorithm for retrieving the optical depth and mean effective size of cirrus clouds from comparisons of measured reflectances with entries in the library. We first prescribe the sun-sensor geometric parameters including solar zenith angle, sensor viewing zenith angle and relative azimuth angle for each pixel. In the algorithm sensitivity studies, the surface albedo was determined based on climatological data sets. We then select values for the mean effective ice crystal sizes and optical depths. Subsequently, we construct radiance tables for each combination of ice crystal mean effective size and optical depth and for each VIIRS channel used for cloud retrieval (1.61μm and either 0.672μm or 1.24μm). A series of numerical iteration procedures are set up to search for the simulated reflectances that best match the measured reflectances (see Appendix B). In the algorithm , the "simulated" reflectances are precomputed using the LBLE and stored as LUTs. The numerical scheme is basically composed of minimizing the sum of the square of the "residual" for each channel. The "residual" is defined as the difference between the logarithm of simulated reflectance and the logarithm of the measured reflectance. This definition of the residual used for determining the best fit is typically defined as a least-squares fit (Twomey and Cocks, 1989). The retrieved cloud parameters consist of the combination of optical depth and effective particle size associated with the best-fit reflectances, yielding the minimal residual.

C3 ## Flow Chart for Cirrus Solar Retrieval Algorithm

Determine Geometry and
Surface Albedo for each Pixel:
$\mu, \mu_0, \phi, Ag(\lambda)$

VIIRS & Near-IR Radiance Data

Calculated libraries for
$r_e = r_{e1}, r_{e2}, r_{e3}, \dots, r_{en}$
$\tau = \tau_1, \tau_2, \tau_3, \dots, \tau_m$

Compute Reflectance Functions
$r_{comp}(\lambda=0.672\,\mu m, \tau_m, r_{en}; \mu, \mu_0, \phi)$
$r_{comp}(\lambda=1.61\,\mu m, \tau_m, r_{en}; \mu, \mu_0, \phi)$

Measured Reflectances:
$r_{meas}(\lambda=0.672\,\mu m, \mu, \mu_0, \phi)$
$r_{meas}(\lambda=1.61\,\mu m, \mu, \mu_0, \phi)$

Residual Definition:
$$\{ ln[r_{comp}(\lambda=0.672\mu m, \tau_m, r_{en}; \mu, \mu_0, \phi)] - ln[r_{meas}(\lambda=0.672\,\mu m, \mu, \mu_0, \phi)]\}^2$$
$$+ \{ ln[r_{comp}(\lambda=1.61\,\mu m, \tau_m, r_{en}; \mu, \mu_0, \phi) - ln[r_{meas}(\lambda=1.61\,\mu m, \mu, \mu_0, \phi)]\}^2$$

Determine combination of τ_m, r_{en} that minimizes residual

Figure 16. Flow Chart for the solar Cirrus Retrieval Algorithm

C4

Input VIIRS 0.672(M5),1.24 (M8),1.61 μm (M10) reflectances, and 8.55 (M14), 12 μm (M16) radiances for Cloudy Pixels

Determine τ, and D_e from 0.672/1.24 and 1.61 μm reflectance LUTs - daytime Solar Algorthm)

Compute cloud-top temperature (T_c) using M14 and M16 radiances and

$$k_{16}/k_{14} = 1.596 - 0.004 * D_e$$

$$[(R_{16}-B_{16}(Tc)) / (R_{a16}-B_{16}(T_c))] - [(R_{14}-B_{14}(T_c)) / (R_{a14}-B_{14}(T_c))]^{k_{16}/k_{14}} = 0$$

Exit
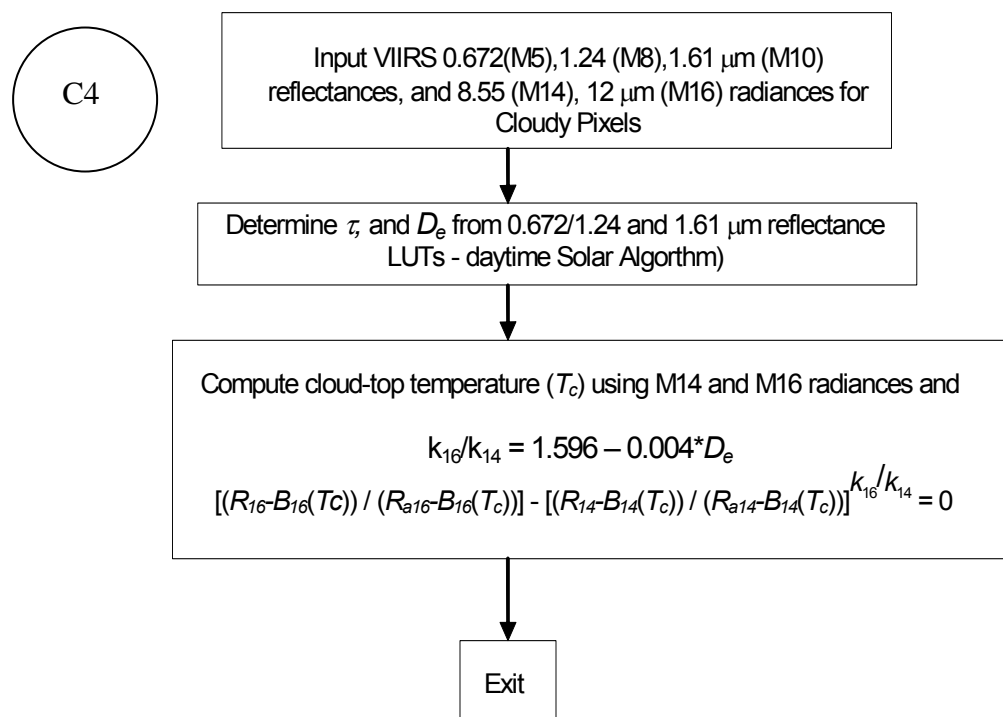
Figure 17. Flow Chart for the Daytime IR Cirrus Single-Channel CTT Retrieval Algorithm.

Figure 17 shows the flowchart for the daytime cirrus cloud COP (C3) for the retrieval of Cloud top temperature. We first use C3 to determine the visible optical depth and effective particle size. Then we use C4 (as in C1) to determine the cloud-top temperature.

Thin Cirrus Overlaying Sunglint Surfaces

Sun glint does not normally affect the cloud EDRs since clouds preclude any surface reflection. The sole exception is the case of thin cirrus clouds overlaying sun glint areas with no additional underlying clouds. This case will be indicated by the VIIRS Cloud Mask via the following checks:

- flags indicate the possibility of sun glint,
- flags indicate thin cirrus exists,
- other cloud flags have not been tripped.

The thin cirrus tests use M9 (1.378μm) and the thermal infrared bands, M15 (10.7625μm) and M16 (12.0125μm). These tests are not compromised by sun glint. When the special circumstance of only thin cirrus (no other clouds) over sun glint occurs, then cloud top temperature is determined using M15 (10.7625μm) alone instead of M12 (3.7μm) and M15 (10.7625μm) together. The cloud top temperature solution will degrade somewhat, but this is unavoidable given the specular reflection noise precluding the use of M12 observations during sun glint conditions.

3.3.2.2   **Retrieval of Water Cloud Parameters**

Once the water cloud pixels are identified, two retrieval programs are applied to nighttime and daytime data as shown in Figure 18. For the daytime retrieval, the solar water cloud retrieval algorithm (W1) uses the VIIRS 0.672μm (non-snow/ice surfaces), 1.24μm (snow/ice surfaces) and 1.61μm reflectance data to infer water cloud optical depth and mean effective radius (r_e). Unlike the ice cloud retrieval, there is no IR algorithm for water cloud retrievals during daytime. For this case, the Cloud Optical Properties (COP) unit does not return a value for cloud top temperature instead depending upon the Cloud Top Parameters (CTP) unit for generation of this parameter. For the nighttime retrieval, the IR water cloud retrieval algorithm (W2), using the VIIRS 3.7μm and 10.76μm radiances, along with microphysical parameterizations, is employed to infer the water cloud temperature, mean effective radius and visible optical depth.

Solar Water Cloud Retrieval Algorithm

A generalized description of the solar water cloud retrieval algorithm is as follows. Figure 19 shows an algorithm for retrieving the optical depth and mean effective size of water clouds from comparisons of measured reflection functions with entries in the library. We first prescribe the sun-sensor geometric parameters, including the solar zenith angle, the sensor viewing zenith angle and relative azimuth angle for each pixel. Operationally, surface albedo is obtained from a internal table given the surface type from the VIIRS Cloud mask. In the algorithm sensitivity studies, the surface albedo is determined from climatological data.

Water Cloud Retrieval Program
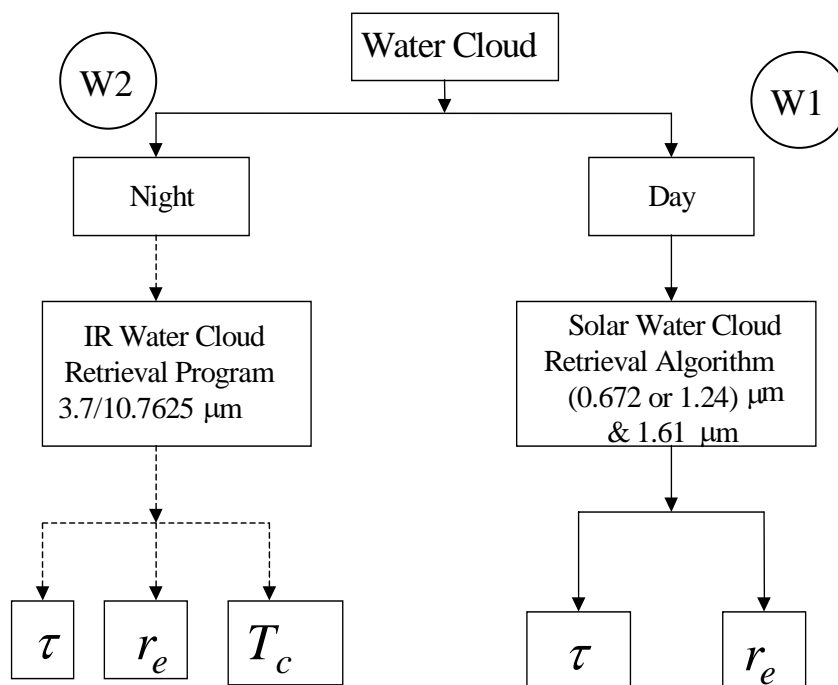
Figure 18. Flow Chart for the Water Cloud Retrieval Program.

W1 Flow Chart for Water Cloud Solar Retrieval Algorithm

Determine Geometry and
Surface Albedo for each Pixel:
$\mu, \mu_0, \phi, Ag(\lambda)$

VIIRS & Near-IR Radiance Data

Calculated libraries for
$r_e = r_{e1}, r_{e2}, r_{e3}, \ldots, r_{en}$
$\tau = \tau_1, \tau_2, \tau_3, \ldots, \tau_m$

Compute Reflectance Functions
$r_{comp}(\lambda=0.672\,\mu m, \tau_m, r_{en}; \mu, \mu_0, \phi)$
$r_{comp}(\lambda=1.61\,\mu m, \tau_m, r_{en}; \mu, \mu_0, \phi)$

Measured   Reflectances
$r_{meas}(\lambda=0.672\,\mu m, \mu, \mu_0, \phi)$
$r_{meas}(\lambda=1.61\,\mu m, \mu, \mu_0, \phi)$

Residual Definition:
$\{ln[r_{comp}(\lambda=0.672\mu m, \tau_m, r_{en}; \mu, \mu_0, \phi)] - ln[r_{meas}(\lambda=0.672\,\mu m, \mu, \mu_0, \phi)]\}^2$
$+ \{ln[r_{comp}(\lambda=1.61\,\mu m, \tau_m, r_{en}; \mu, \mu_0, \phi) - ln[r_{meas}(\lambda=1.61\,\mu m, \mu, \mu_0, \phi)]\}^2$

Determine combination of τ_m, r_{en} that minimizes residual

Figure 19. Flow Chart for the Solar Water Cloud Retrieval Algorithm.

Subsequently, we construct reflectance arrays for each combination of water droplet effective radius, optical depth and for each VIIRS channel used for cloud retrieval (0.672, 1.24 and 1.61 m) at given surface, solar and sensor geometry conditions. A series of numerical iteration procedures, as described in Appendix B, are set up to search for the simulated reflectances in the arrays that best match the measured reflectances. In the algorithm , the "simulated" reflectances are pre-computed using the LBLE and stored as LUTs. The numerical scheme minimizes the sum of the square of the "residual" for each channel. The "residual" is defined as the difference between the logarithm of the simulated reflectance and the logarithm of the measured reflectance.

Nighttime IR Water Cloud Retrieval Algorithm

The retrieval program for inferring water cloud temperature, effective droplet radius and optical depth from the upwelling radiance of VIIRS cloud retrieval channels is similar to the cirrus cloud IR retrieval program. It also follows the principles of the dual-IR-channel technique presented in Liou *et al*. (1990). The VIIRS $3.7\mu m$ and $10.76\mu m$ radiances are used for retrieval. A major advantage of using these two channels for water cloud retrievals is that the presence of water vapor has almost no effects on the radiance of these window bands.

a. Radiative parameterizations

From the theory of radiative transfer, we may express the upwelling radiance at TOA for the 3.7µm (M12) and 10.76µm (M15) channels over a water cloud atmosphere as

$$R_i = R_{wi} + T_i R'_i \qquad i = 12,\ 15 \qquad (57)$$

where R_{wi} and T_i are the emitted radiance and the transmittance due to atmospheric water vapor and other gaseous species above the water cloud top, respectively; and R'_i is the atmospheric-corrected upwelling radiance at the cloud top. The second term in Eq. (57) represents the portion of the TOA radiance attributed to the transmitted upwelling radiance at the cloud top. A version of the radiative transfer program developed by Kratz (1995) has been used to compute the two atmospheric parameters. However, we use parameterization equations to determine R_{wi} and T_i. With those, it is then possible to derive R'_i from Eq. (63).

We then further express R'_i in terms of the water cloud mean temperature T_c and emissivities ε_{12} and ε_{15} as follows:

$$R'_i = (1 - \varepsilon_i) R'_{ai} + \varepsilon_i B_i(T_c) \qquad i = 12,\ 15 \qquad (58)$$

where R'_{ai} denote the upwelling radiance reaching the cloud base for the two spectral bands, and $B_i(T_c)$ are the respective Planck functions at T_c. The first term on the right-hand side of Equation 64 represents the contribution of the transmitted radiance from below the cloud. The second term denotes the emission contribution from the cloud itself.

In order to solve Equation (58) for T_c and ε_i numerically, we can correlate ε_{12} and ε_{15}, and relate $B_{12}(T_c)$ with $B_{15}(T_c)$. The clear radiance $R_{a12,}$ and $R_{a15,}$ must also be known. First we compute the Planck functions $B_{12}(T_c)$ and $B_{15}(T_c)$, taking into account the filter functions of both channels, and produce values of both $B_{12}(T_c)$ and $B_{15}(T_c)$ in 0.1 K intervals within the range of T_c from 150 to 300K.

Then, we investigate the relationship between the emissivities for the two channels. From radiative transfer calculations and following the approach proposed by Liou et al. (1990), we may parameterize water emissivities at the 3.7 and 10.76µm wavelengths in terms of visible optical depths τ in the form:

$$\varepsilon_i = \alpha_i[1 - \exp(-k_i \tau / \cos\theta_{swnsor})] \qquad i = 12,\ 15 \qquad (59)$$

The exponential term represents the effective transmissivity. The parameters k_{12} and k_{15} represent the effective extinction coefficients for the two channels accounting for multiple scattering within water clouds and for the difference between visible and IR extinction coefficients. Both k_{12} and k_{15} are smaller than 1 because the effect of multiple scattering increases transmission. Thus the products $k_i\tau$ may be considered as effective optical depth that would yield the same emissivity values for the non-scattering conditions at the 3.7 and 10.76µm wavelengths. A scaling factor $_i$ has been added to Equation 66, which accounts for the scattering effects. For the 10.76µm band, $_{15}$ is nearly 1 due to very small scattering

for that band and is set to 1 in the science code. For 3.7μm, α_{12} is a function of r_e, and its value for a selected r_e can be obtained as the value of α_i at very large τ (~64). Using the α_i values for the nine reference r_e, we obtain a polynomial function of α_i in terms of r_e^{-1} as follows:

$$\alpha_1(r_e) = \sum_{n=0}^{3} m_n r_e^{-n} .$$

(60)

where r_e is in μm, m_0=0.8658, m_1=2.9877, m_2=-4.9921 and m_3=2.4863.

By eliminating τ from Equation 66, we obtain

$$(1 - \varepsilon_{12} / \alpha_{12})^{1/k_{12}} = (1 - \varepsilon_{15})^{1/k_{15}}$$

(61)

Equation 68 correlates ε_{12} and ε_{15} directly. A further combination of Equations 64 and 68 leads to:

$$[1 - (R'_{a12} - R'_{12}) / \alpha_1 (R'_{a12} - B_{12}(T_c))]^{1/k_{12}} = [(R'_{15} - B_2(T_c)) / R'_{a15} - B_{15}(T_c))]^{1/k_{15}}$$

(62)

Substitution of Equation 58 into Equation 62 results in a nonlinear algebraic equation, with T_c as the only unknown:

$$[(R'_{15} - B_{15}(T_C)) / (R'_{a15} - B_{15}(T_C))] - [1 - (R'_{a12} - R'_{12}) / \alpha_1 (R'_{a12} - B_{12}(T_C))]^{k_{15}/k_{12}} = 0$$

(63)

b. Radiative-microphysical parameterizations

We investigate the dependence of k_{15}/k_{12} on the particle size distribution and optical depth based on radiative transfer calculations by using nine water droplet size distributions given in Section 3.4. A reasonable range of optical depth (0.125-64) for these size distributions has been used. As an initial approximation, we may take k_{12} and k_{15} as independent of the optical depth. However, for more accurate retrieval of water cloud parameters, we need to consider the dependence of k_{15}/k_{12} on the optical depth. Generally, k_{15}/k_{12} decreases as r_e increases. For a small r_e (~2μm), k_{15}/k_{12} is close to 2.5. This is primarily because the single-scattering albedo is larger for the 3.7μm wavelength (~0.8) than that for the 10.76μm wavelength (~0.4), which implies that more scattering is associated with the former wavelength. For r_e > 16 μm, k_{15}/k_{12} approaches 1 for the following reasons. First, the extinction coefficients are approximately the same for the two wavelengths because of large-size parameters in which the geometric optics limit is valid. Second, the single-scattering albedos are also approximately the same for these wavelengths because substantial absorption occurs within large water droplets. This implies that only the diffracted and externally reflected light contributes to the scattering processes. For obtaining the initial guesses, k_{15}/k_{12} can be expressed in terms of $\ln(\tau)$ in the form:

$$k_{15}/k_{12} = \sum_{n=0}^{3} d_n [\ln(\tau)]^n$$

(64)

where the coefficients d_n are determined from a second-order least square method using the radiance tables. In the operational retrieval scheme, however, d_n are further expressed as third-order polynomial functions of $\ln(r_e)$:

$$d_n = \sum_{m=0}^{2} b_{mn} \left[\ln(r_e) \right]^m \qquad (65)$$

where the coefficients b_{mn} are provided in Table 7.

Table 7. Coefficients (b_{mn}) to compute k_{15}/k_{12} from Optical Depth and Water Cloud Effective Droplet Radius.

	$r_e < 12\mu m$			$r_e \geq 12\mu m$		
	m = 2	m = 1	m = 0	m = 2	m = 1	m = 0
n = 3	0.0083	-0.0172	-0.004	0	-0.0056	0.01
n = 2	-0.0348	0.0393	0.1065	0.059	-0.3445	0.4798
n = 1	-0.1093	0.3897	-0.6297	0	0.117	-0.6268
n = 0	0.5188	-1.1634	1.8143	-0.3106	1.4341	0.4822

c. Microphysical Parameterizations

We start with the familiar relationship between r_e, *LWP*, and .

$$r_e = \frac{3}{2} \frac{LWP}{\rho_l \tau}, \qquad (66)$$

Where r_e is the mean effective radius (m), *LWP* is the liquid water path (gm / m^2), ρ_l is the water density (= 1 gm /cm^3), is the optical depth (A unit conversion factor of 1000 must be multiplied). *LWP* can be obtained from

$$LWP = LWC \times \Delta z, \qquad (67)$$

Where LWC is the liquid water content (gm / m^3), Δz is the cloud geometric thickness. We assume $\Delta z = 1$ km. Following Matveev (1984), the climatological mean water cloud LWC may be expressed as a function of temperature. Based on his results, we assume that LWC can be obtained based on the following relationship:

$$LWC = a + bT_c, \qquad (68)$$

where *a* = -1.284 and *b*=0.0055, T_c is the cloud temperature (K).

d. Solution procedures

Figure 20 shows a schematic description of the solution procedures. Using the VIIRS 3.7 and 10.7625μm channel data, we first obtain an estimate of mean water cloud temperature based on the 10.76 mm brightness temperature, and effective droplet size from Eq. (66). Then we compute k_{15}/k_{12} and α_{12} based on Eqs. (64) and (60), respectively, and substitute these parameters into Eq. (63) to obtain cloud-top temperature by a numerical iterative method. Afterward, the visible optical depth is obtained from Eq. (59), and the effective droplet radius is obtained from Eq. (66).

Input VIIRS 3.7 and 10.76μm Radiances for Cloudy Pixels

Set initial cloud temperature guess (T_c) as brightness temp. @ 10.76 μm;

Set initial cloud optical thickness (τ) = 12; Calculate initial particle size (r_e) as:

$$r_e = 3LWP \Big/ 2\rho\tau \quad \text{where } LWP = LWC \times \Delta z, \text{ and } LWC = a + bT_c$$

Calc. new T_c: $k_{15}/k_{12} = \sum_{n=0}^{3} d_n(r_e)[\ln(\tau)]^n$ and $\alpha_1 = \sum_{n=0}^{3} m_n r_e^{-n}$

$$[(R'_{15}-B_{15}(T_c))/(R'_{a15}-B_{15}(T_c))] - [1-(R'_{a12}-R'_{12}(T_c))/\alpha_1(R'_{a12}-B_{12}(T_c))]^{k15/k12} = 0$$

New τ: $\varepsilon_{15} = (R'_{a15} - R'_{15})/(R'_{a15} - B_{15}(T_c))$; $\tau = -\ln(1-\varepsilon_{15})/k_{15}$

New r_e: $r_e = 3LWP \Big/ 2\rho\tau$ (Note: $k_{15} = 0.52$)

Do T_c, τ and r_e all converge?   No
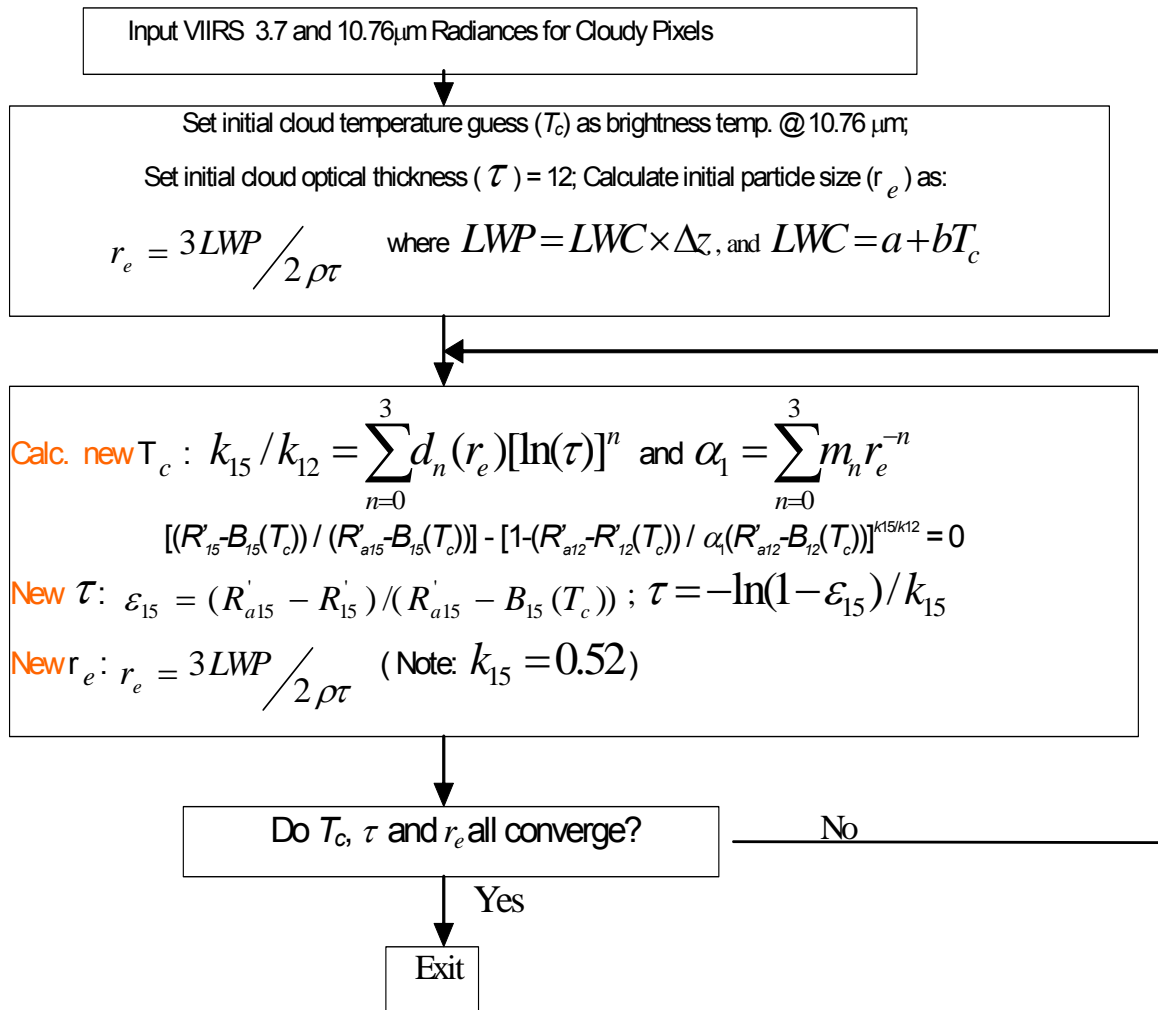
Yes

Exit

Figure 20. Flow Chart for the Nighttime IR Water Cloud Retrieval Algorithm.

3.3.3 Algorithm Output

Effective particle size and optical depth are output for all clouds and illumination conditions. Additionally, cloud temperature is retrieved whenever the IR algorithms are used which includes ice clouds (day and night) and water clouds at night. During daytime, water cloud

temperature is not retrieved from these algorithms. It will instead be estimated from the Cloud Top Parameters unit.

3.3.4 Variance and Uncertainty Estimates

Retrieval errors can be caused by instrumental characteristics including noise and calibration errors. Algorithm sensitivity studies on the EDR uncertainty due to instrumental noises have been performed by adding random noises to the simulated radiances according to the sensor noise model. Results of these studies are presented in sections 3.4 and 3.5. A summary of these studies are given as follows.

Algorithm sensitivity studies have been carried out separately for cirrus clouds using solar and IR algorithms and for water clouds using solar algorithms. These studies are designed to investigate whether the algorithms meet the threshold and objective requirements specified in VIIRS SRD (Appendix A) given reasonable assumptions about the uncertainty of input radiance. The key requirements for the retrieved optical depth and effective particle size are the measurement range, measurement accuracy and precision errors. Other requirements are less relevant than these. According to the specification of the SRD, for optical depth, the threshold requirement for the measurement range is between 0 and 10. The threshold requirement for measurement accuracy is the greater of 10 percent or 0.05 optical depth; and the objective requirement for measurement accuracy is the greater of 5 percent or 0.025 (suggested value). Also, the threshold requirement for precision error is the greater of 5 percent or 0.025 optical depth, and the objective requirement is the greater of 2 percent or 0.02 (suggested value). For effective particle size, the threshold requirement for the measurement range is between 0 and $50\mu m$. The threshold requirement for the measurement accuracy is the greater of 10 percent or $4\mu m$; and the objective requirement is the greater of 5 percent or $2\mu m$. The threshold requirement for the measurement precision is the greater of 5 percent or $2\mu m$; while the objective requirement is 2 percent. We demonstrate that these threshold and objective values for the measurement range, accuracy and precision errors are met.

A few values of the measurement requirements above are to be determined by the contractor. For optical depth, we suggest the objective value for the measurement range is between 0.1 and 64, and between 0.1 and 12 for the retrieval of daytime and nighttime water clouds, respectively; and between 0.1 and 10 for the retrieval of both daytime and nighttime cirrus clouds. The lower limit of the range should be 0.1 instead of 0 for both threshold and objective. The originally set lower bound 0 corresponds to clear, while 0.1 represents an adequate lower limit based on research results (e.g., Ou *et al.*, 1995). Moreover, water cloud optical depths cover most of this range. Established research-grade solar algorithms (e.g., King *et al.*, 1996) address the range between 0.5 and 64 for water cloud retrieval. In addition, based on Ou *et al.* (1993, 1995) and Rao *et al.* (1995), the measurement range of the optical depth of both daytime and nighttime cirrus cloud is between 0.1 and 10. Nighttime retrievals for water clouds are more difficult to achieve, and the anticipated measurement range based on IR techniques is about 1 to 12.

We also suggest the objective value for the measurement precision of optical depth is the greater of 2 percent and 0.02. Based on Figure 10 of the MODIS-ATBD, Version 6 (King *et al.*, 1996), for water cloud optical depth larger than 5, the retrieval error of the solar algorithm is generally less than 2 percent. On the other hand, Rao *et al*. (1995) show that for ice cloud optical depth larger than 1, the retrieval errors for optical depth are less than 2 percent, and for optical depth less than 1, the retrieval errors are less than 0.02 optical depth.

For cloud effective particle size, we suggest that the objective requirements for the measurement range are between 5 and 62.5μm for cirrus clouds, and between 2 and 32μm for water clouds. We specify the lower limit of the measurement range to be 1 μm instead of 0μm, because particles with size smaller than 1μm are generally classified as aerosols. It has been demonstrated that the IR algorithm can address the ice crystal mean effective size (D_e) range between 23 and 124μm (Ou *et al.,* 1993, 1995; Rao *et al.,* 1995). Because the definition of the effective particle size implies radius, the above D_e range corresponds to a range of effective particle radius between 11.5 and 62μm. With available *in situ* contrail size distributions and associated single-scattering properties based on the unified light-scattering theories for ice crystals (Liou *et al.,* 1998), the lower limit of retrievable ice crystal effective particle size can be extended down to 5μm. On the other hand, established research-grade solar algorithms address the measurement range between 2 and 32μm for water clouds. Nighttime retrievals for water clouds are more difficult to achieve, and the anticipated measurement range based on the IR techniques is expected to be from 4 to 16μm.

3.4 ALGORITHM SENSITIVITY STUDIES ON RETRIEVALS OF OPTICAL THICKNESS

The algorithm sensitivity studies were carried out using the results generated by the radiative transfer model for seven separate scenarios. These scenarios form the basis for defining the input parameters required by the radiative transfer model. They are:

(1)   Cirrus cloud in US Standard Atmosphere, sensor pointing at nadir.

(2)   Cirrus cloud in US Standard Atmosphere, sensor pointing off-nadir.

(3)   Cirrus cloud in US Standard Atmosphere, sensor pointing at edge-of-scan.

(4)   Cirrus cloud in Tropical Atmosphere, sensor pointing at nadir.

(5)   Cirrus cloud in Sub-Arctic Atmosphere, sensor pointing at nadir.

(6)   Cirrus cloud in Desert Atmosphere, sensor pointing at nadir.

(7)   Water cloud in US Standard Atmosphere, sensor pointing at nadir.

For scenarios 1 through 4, synthetic retrievals for both daytime and nighttime conditions were carried out for combinations of input cirrus optical depths and effective particle sizes. For scenario 7, only synthetic retrievals for daytime conditions were carried out.

The LBLE described in Section 3.3.1.7 was used to generate simulated radiance. The input parameters for each scenario are given in Table 8. For all scenarios, the solar zenith angle is fixed at 32°, the nominal date is 1 May and the location is 40° North based on the Raytheon VIIRS orbital simulation. Parameters specified include the atmospheric profile, sun-sensor geometry, retrieval channel characteristics (including central wavelength, bandwidth and response function), cloud type, altitude and thickness, as well as surface albedo and emissivity. The radiative transfer calculations are performed for a wide range of selected visible optical depths and mean effective sizes. For cirrus clouds, the optical depths are: 0.125, 0.25, 0.5, 1, 2, 3, 4, 5, 6, 7, 8, 9, 10 and 12. The mean effective sizes are: 23.9, 30.4, 41.5, 71 and 93μm. For water clouds, the optical depths are: 0.125, 0.25, 0.5, 1, 2, 3, 4, 5, 6, 8, 12, 16, 24, 32, 48 and 64. The mean droplet radii are: 2, 3, 4, 6, 8, 12, 16, 24 and 30μm. Many radiance values are thus produced, and they are further processed to create data sets that are appropriate for the parameter retrieval algorithms and algorithm sensitivity analyses.

This section addresses results of the algorithm sensitivity analysis for Cloud Optical Depth using the cirrus and water cloud IR and solar retrieval algorithms. The results of these algorithm sensitivity analyses follow.

3.4.1 SNR Tests

The SNR tests address the impact of SNR on both pixel-level and image-level retrievals. The pixel-level retrievals are performed for a single pixel assuming various combinations of cloud optical depth and effective particle size. The imagery-level retrievals are performed for pixels aggregated (averaged) to VIIRS SRD horizontal cell size (HCS). The required HCS is a function of EDR parameter; threshold and objective values are stated. In this report, only the pixel-level SNR tests are addressed. The test results are presented separately for the solar algorithm and IR algorithms. To create data sets to support the pixel level SNR test, noise based on the system specification noise model is added directly to the radiance contained in the radiance tables and then retrievals are performed using the noise-added data in the tables. To guarantee sample sizes are sufficient to support tests, noise is randomly added to each radiance value 32 times. In effect, 32 noise perturbed radiance tables are created. Retrievals are performed using each of the 32 noise-added tables and the no-noise table. The results of the retrieval process are then statistically analyzed to compute the metrics described in the SRD (accuracy, precision, etc.).

Table 8. Input Parameters for Each Scenario.

	SET #						
	USSCir-n1*	**USSCir-i***	**USSCir-eos**	**TCir-n**	**SACir-n**	**DesCir-n**	**USSWat-n**
Description	Baseline US Standard/ Cirrus Nadir	Baseline US Standard/ Cirrus Intermediate	Baseline US Standard/ Cirrus Edge-of-Scan	Baseline Tropical/ Cirrus Nadir	Baseline Subarctic / Cirrus Nadir	Baseline Desert/ Cirrus Nadir	Baseline US Standard/ Water Cloud
Atmosphere							
US Standard (1)	X	X	X				X
Tropical (3)				X			
Sub-arctic					X		
Desert						X	
Skin Temperature MODTRAN Default (uses sfc air temp.)	X	X	X	X	X	X	X
Aerosol Model MODTRAN Default	X	X	X	X	X		X
Desert						X	
Sensor Geometry							
Nadir	X			X	X	X	X
Off-Nadir		X					
Edge-of-Scan			X				
Cloud Height	9-10 km	9-10 km	9-10 km	14-15 km	9-10 km	9-10 km	1 -2 km

3.4.1.1   **Daytime**
Results

Cirrus Cloud in US Standard Atmosphere, Sensor Pointing at Nadir

Figure 21 shows the two-dimensional correlations for the reflectance pairs: 0.672–1.61μm and 0.672–2.25μm for the selected six ice crystal size distributions and 14 optical depths. These diagrams clearly illustrate the information content of optical depth and mean effective

size in the 0.672, 1.61 and 2.25µm reflectances. Display of the 0.672 and 1.61µm reflectance correlation shows that if the mean effective size of an ice cloud is larger than about 24µm but less than about 124µm, an accurate retrieval of ice crystal mean effective size can be achieved. Based on a similar argument, if the optical depth of an ice cloud is larger than about 0.5 but less than 12, an accurate retrieval of optical depth can also be obtained. Also noted is that the 0.672µm reflectance mainly depends on the optical depth, while the 1.61 and 2.25µm reflectances are primarily functions of mean ice crystal size for optically thick ice clouds. Consequently, data for these three channels can be utilized to determine both optical depth and mean effective ice crystal size. The validity of such correlations has been examined using the MAS data obtained from the flight missions during FIRE-II IFO. Limited comparisons between MAS data points and computed results show that most of the data points fall inside the correlative mesh of optical depth vs. mean effective size.

Figure 22 show the accuracy and precision of retrieved optical depths as functions of optical depth. These results are based on retrievals of combinations of all possible optical depths and mean effective sizes using the display of the 0.672 and 1.61µm reflectance correlation. Two straight lines denote threshold (greater of 10 percent or 0.05) and objective (greater of 5 percent or 0.025) values. The accuracy of retrieved optical depths meets both the threshold and objective requirements for most selected values of optical depth. The precision of retrieved optical depths meets both the threshold (greater of 5 percent or 0.025) and objective (greater of 2 percent or 0.02) requirements for most selected values of optical depth. For very small optical depths (e.g., < 0.5), both the accuracy and precision errors are close to threshold and objective requirements, but for larger optical depths, both the accuracy and precision errors are well below the threshold and objective curves and are close to zero. The extremely small values of accuracy and precision errors indicate that the solar algorithm is highly accurate and very stable in retrieving optical depths in this case.
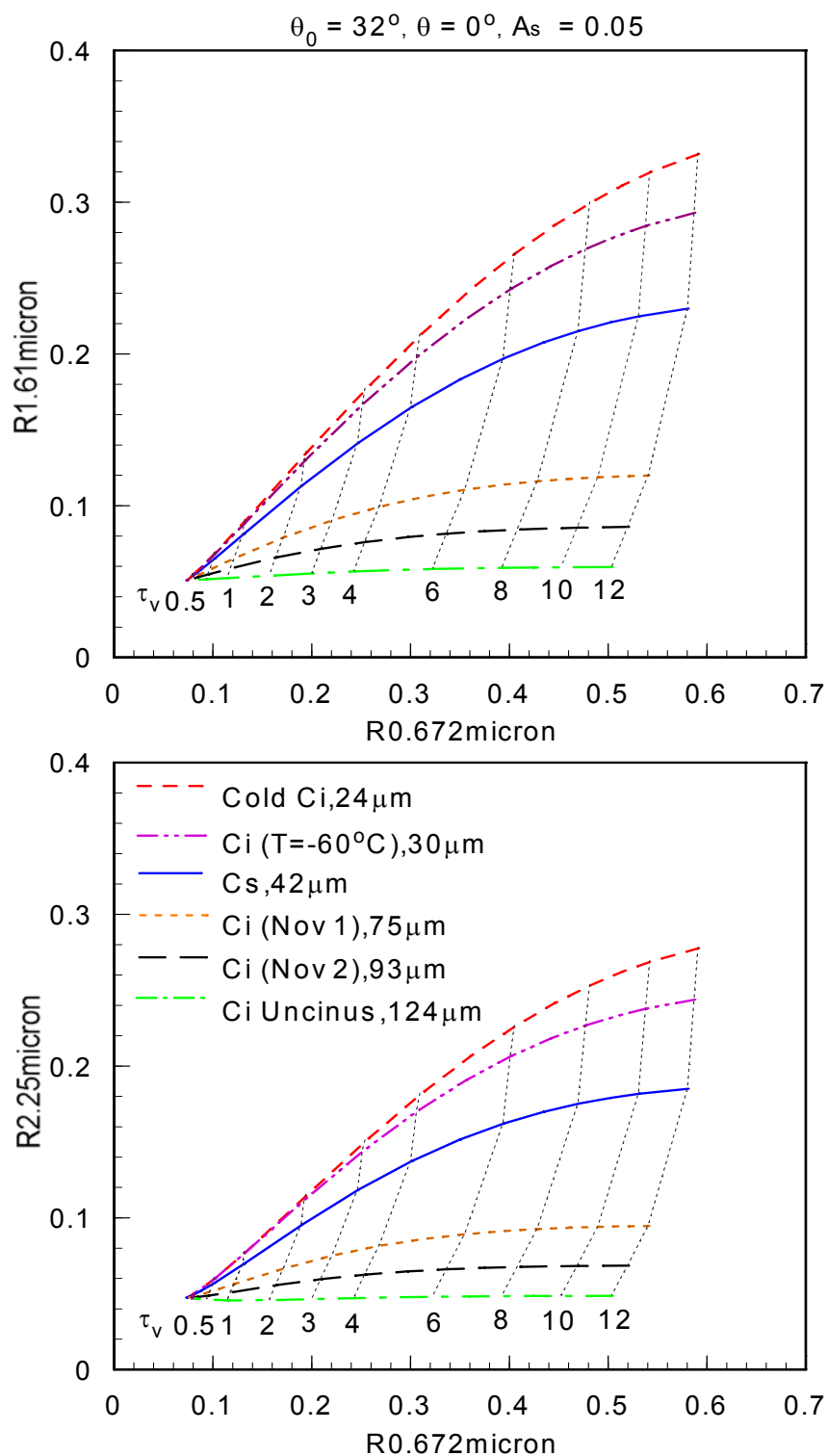
Figure 21. Display of the Correlation between the VIIRS 0.672 and 1.61μm Reflectances (top) and between the 0.672 and 2.25μm Reflectances (bottom) for Cirrus Clouds in US Standard Atmosphere, Sensor at Nadir.

Accuracy of Optical Depth (Daytime)
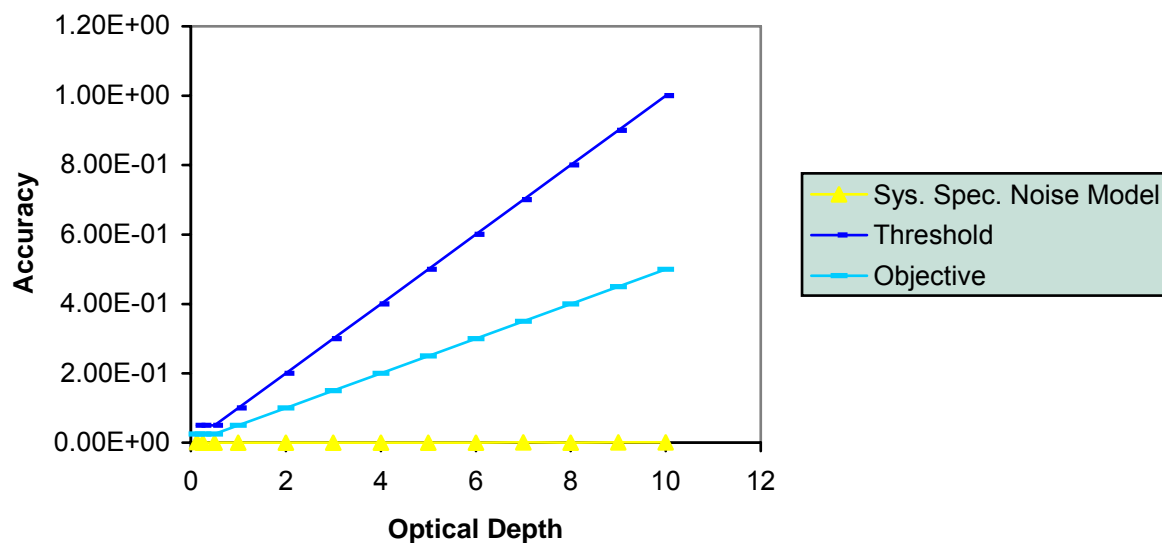
Precision of Optical Depth (Daytime)

Figure 22. Accuracy (top) and Precision (bottom) of Retrieved Optical Depths from the Cirrus Solar Algorithm for US Standard Atmosphere based on the 0.672–1.61μm Correlation, Sensor at Nadir.

To examine the effects of adding the VIIRS 2.25μm channel for the retrieval of cirrus cloud parameters, Figure 23 show the accuracy and precision of retrieved optical depths as functions of optical depth. These results are based on retrieval combinations of all possible optical depths and mean effective sizes using the display of the 0.672 and 2.25μm reflectance correlation. Two straight lines denote threshold (greater of 10 percent or 0.05) and objective (greater of 5 percent or 0.025) values. The accuracy of retrieved optical depths meets both the threshold and objective requirements for most selected values of optical depth. The precision of retrieved optical depths meets both the threshold (greater of 5 percent or 0.025) and objective (greater of 2 percent or 0.02) requirements for most selected values of optical depth. For very small optical depths (e.g., <0.5), both the accuracy and precision errors are close to threshold and objective requirements. For larger optical depths, both the accuracy and precision errors are close to zero for a variety of surface conditions, different geometries, and different cloud types. Figure 23 is similar to Figure 22. Thus we expect all retrievals using the 0.672-2.25μm correlations will produce similar results as those using the 0.672-1.61μm correlations. For the rest of the algorithm studies on the solar retrieval algorithm, we will only show results using the 0.672-1.61μm correlation.

Cirrus Cloud in US Standard Atmosphere, Sensor pointing Off-nadir

Figure 24 shows the two-dimensional correlations for the reflectance pairs: 0.672–1.61μm and 0.672–2.25μm for the selected ice crystal size distributions and optical depths. The sensor zenith angle is 40°, and the relative azimuth angle is 136°. Like Figure 21, these diagrams illustrate the information content of optical depth and mean effective size in the 0.672, 1.61 and 2.25μm reflectances. However, both the 1.61 and 2.25μm surface albedos are changed from 0.05 in Figure 21 to 0.25 to simulate the land surface condition. Thus, the shape of the correlation mesh in Figure 24 is different than that in Figure 21. This change of the shape of the correlation mesh does not affect the retrieval accuracy and precision. Display of the 0.672 and 1.61μm reflectances correlation shows that if the mean effective size of an ice cloud is larger than about 24μm but less than about 124μm, an accurate retrieval of ice crystal mean effective size can be achieved. Based on a similar argument, if the optical depth of an ice cloud is larger than about 0.5 but less than 12, an accurate retrieval of optical depth can also be obtained. Also noted is that the 0.672μm reflectance mainly depends on the optical depth, while the 1.61 and 2.25μm reflectances are primarily functions of mean ice crystal size for optically thick ice clouds. Consequently, data for these three channels can be utilized to determine both optical depth and mean effective ice crystal size.

Accuracy of Cloud Optical Depth
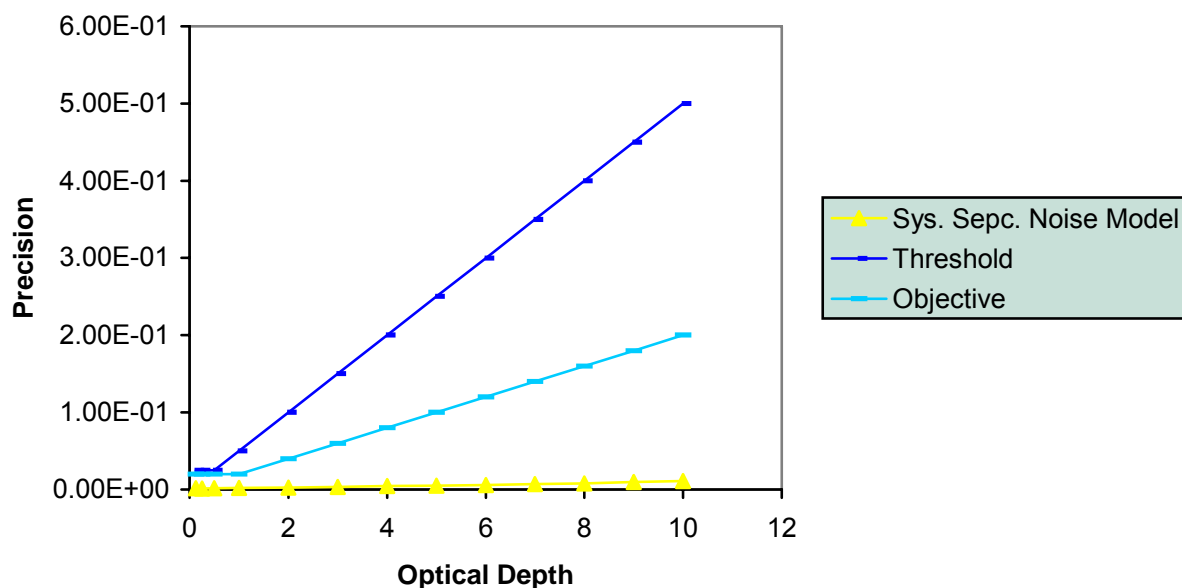

Precision of Cirrus Cloud Optical Depth

Figure 23. Accuracy (top) and Precision (bottom) of Retrieved Optical Depths from the Cirrus Solar Algorithm for US Standard Atmosphere based on the 0.672–2.25 μm Correlation, Sensor at Nadir.

Figure 24. Display of the 0.672-1.61μm (top) and 0.672-2.25μm (bottom) Reflectance Correlations for Cirrus Cloud in US Standard Atmosphere, Sensor pointing Off-Nadir.

Figure 25 show the accuracy and precision of retrieved optical depths as functions of optical depth. These results are based on retrieval combinations of all possible optical depths and mean effective sizes. Two straight lines denote threshold (greater of 10 percent or 0.05) and objective (greater of 5 percent or 0.025) values. The accuracy of retrieved optical depths meets both the threshold and objective requirements for most selected values of optical

depth. The precision of retrieved optical depths meets both the threshold (greater of 5 percent or 0.025) and objective (greater of 2 percent or 0.02) requirements for most selected values of optical depth. For very small optical depths (e.g., <0.5), both the accuracy and precision errors are close to threshold and objective requirements, but for larger optical depths, both the accuracy and precision errors are well below the threshold and objective curves. The small values of accuracy and precision errors again indicate that the solar algorithm is highly accurate and very stable in retrieving optical depths for the off-nadir sensor position.

Cirrus Cloud in US Standard Atmosphere, Sensor at Edge-of-Scan

Figure 26 shows the two-dimensional correlations for the reflectance pairs: 0.672–1.61μm and 0.672–2.25μm for the selected ice crystal size distributions and optical depths. The sensor is assumed to be pointing at edge-of-scan. Like Figure 21, these diagrams illustrate the information content of optical depth and mean effective size in the 0.672, 1.61 and 2.25μm reflectances. However, both the 1.61 and 2.25μm surface albedos are changed from 0.05 in Figure 21 to 0.25 to simulate the land surface condition. Thus, the shape of the correlation mesh in Figure 26 is different than that in Figure 21. This change of the shape of the correlation mesh does not affect the retrieval accuracy and precision. Display of the 0.672 and 1.61μm reflectance correlation shows that if the mean effective size of an ice cloud is larger than about 24μm but less than about 124μm, an accurate retrieval of ice crystal mean effective size can be achieved. Likewise, if the optical depth of an ice cloud is larger than about 0.5 but less than 12, an accurate retrieval of optical depth can also be obtained. Also noted is that the 0.672μm reflectance mainly depends on the optical depth, while the 1.61 and 2.25μm reflectances are primarily functions of mean ice crystal size for optically thick ice clouds. Consequently, data for these three channels can be utilized to determine both optical depth and mean effective ice crystal size.
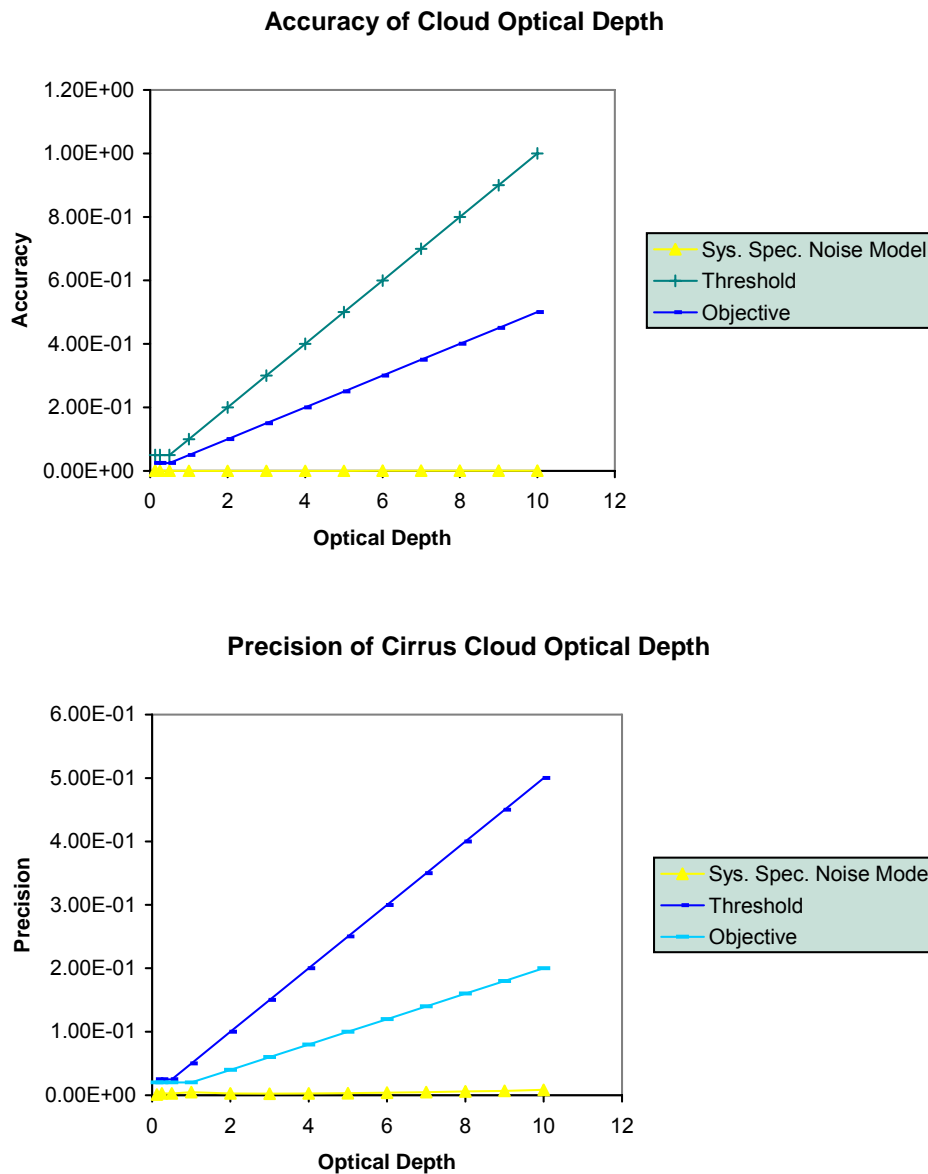
Figure 27 shows the accuracy and precision of retrieved optical depths as functions of optical depth. These results are based on retrieval combinations of all possible optical depths and mean effective sizes. Two straight lines denote threshold (greater of 10 percent or 0.05) and objective (greater of 5 percent or 0.025) values. The accuracy of retrieved optical depths meets both the threshold and objective requirements for most selected values of optical depth. The precision of retrieved optical depths meets both the threshold (greater of 5 percent or 0.025) and objective (greater of 2 percent or 0.02) requirements for most selected values of optical depth. For very small optical depths (e.g., <0.5), both the accuracy and precision errors are close to threshold and objective requirements, but for larger optical depths, both the accuracy and precision errors are well below the threshold and objective curves. The small values of accuracy and precision errors again indicate that the solar algorithm is highly accurate and very stable in retrieving optical depths in the edge-of-scan case.

Accuracy of Cirrus Cloud Optical Depth

Precision of Optical Depth

Figure 25. Accuracy (top) and Precision (bottom) of Retrieved Optical Depths from the Cirrus Solar Algorithm for US Standard Atmosphere, Sensor pointing Off-Nadir.
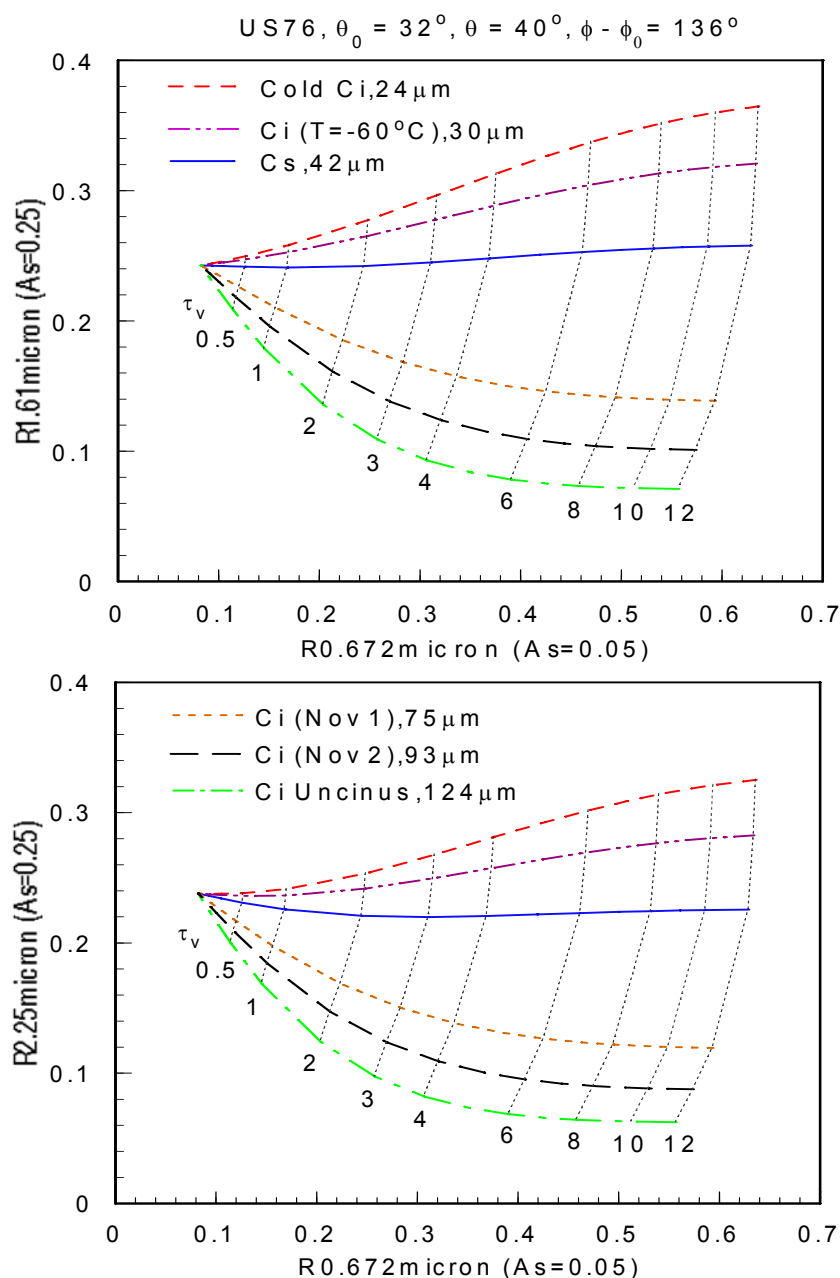
Figure 26. Display of the 0.672-1.61μm (top) and 0.672-2.25μm (bottom) Reflectance Correlations for Cirrus Cloud in US Standard Atmosphere, Sensor at Edge-of-Scan.

**Accuracy - US Standard Atmosphere, ice cloud optical depth,
solar, edge-of-scan**
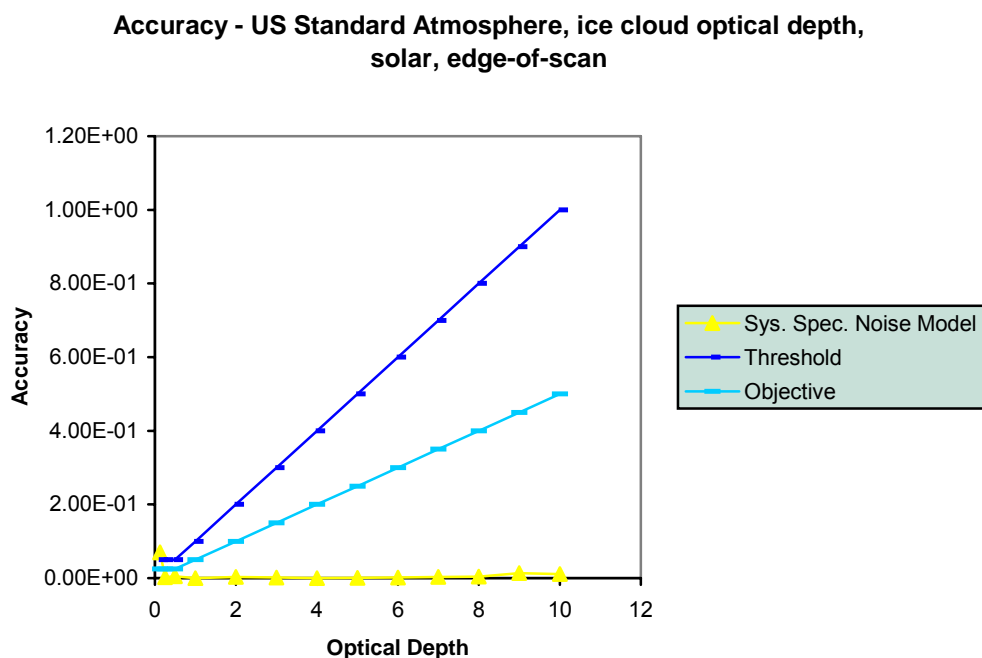
(b)

**Precision - Optical Depth, US Standard Atmosphere, Ice cloud , solar,
edge of scan**
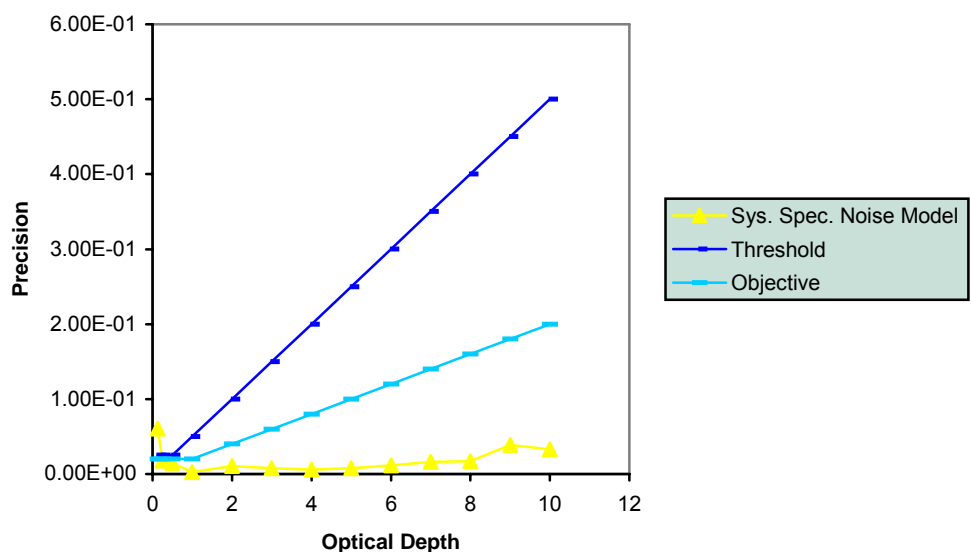
Figure 27 (a) Accuracy and (b) Precision of retrieved optical depths from the solar algorithm for cirrus cloud in US Standard Atmosphere with sensor pointing at edge-of-scan for different sensor noise models.

Cirrus Cloud in Tropical Atmosphere with Sensor at Nadir

Figure 28 shows the two-dimensional correlations for the reflectance pairs: 0.672–1.61μm and 0.672–2.25μm for the selected ice crystal size distributions and optical depths. The sensor is assumed to be pointing at nadir. Like Figure 21, these diagrams illustrate the information content of optical depth and mean effective size in the 0.672, 1.61 and 2.25μm reflectances. However, both the 1.61 and 2.25μm surface albedos are changed from 0.05 in Figure 21 to 0.25 to simulate the land surface condition. Thus, the shape of the correlation mesh in Figure 28 is different than that in Figure 21. This change of the shape of the correlation mesh does not affect the retrieval accuracy and precision. Display of the 0.672 and 1.61μm reflectance correlation shows that if the mean effective size of an ice cloud is larger than about 24μm but less than about 124μm, an accurate retrieval of ice crystal mean effective size can be achieved. Likewise, if the optical depth of an ice cloud is larger than about 0.5 but less than 12, an accurate retrieval of optical depth can also be obtained. Also noted is that the 0.672μm reflectance mainly depends on the optical depth, while the 1.61 and 2.25μm reflectances are primarily functions of mean ice crystal size for optically thick ice clouds. Consequently, data for these three channels can be utilized to determine both optical depth and mean effective ice crystal size.

Figure 29 shows the accuracy and precision of retrieved optical depths as functions of optical depth. These results are based on retrieval combinations of all possible optical depths and mean effective sizes. Two straight lines denote threshold (greater of 10 percent or 0.05) and objective (greater of 5 percent or 0.025) values. The accuracy of retrieved optical depths meets both the threshold and objective requirements for most selected values of optical depth. The precision of retrieved optical depths meets both the threshold (greater of 5 percent or 0.025) and objective (greater of 2 percent or 0.02) requirements for most selected values of optical depth. For very small optical depths (e.g., <0.5), both the accuracy and precision errors are close to threshold and objective requirements, but for larger optical depths, both the accuracy and precision errors are well below the threshold and objective curves. The small values of accuracy and precision errors again indicate that the solar algorithm is highly accurate and very stable in retrieving optical depths.
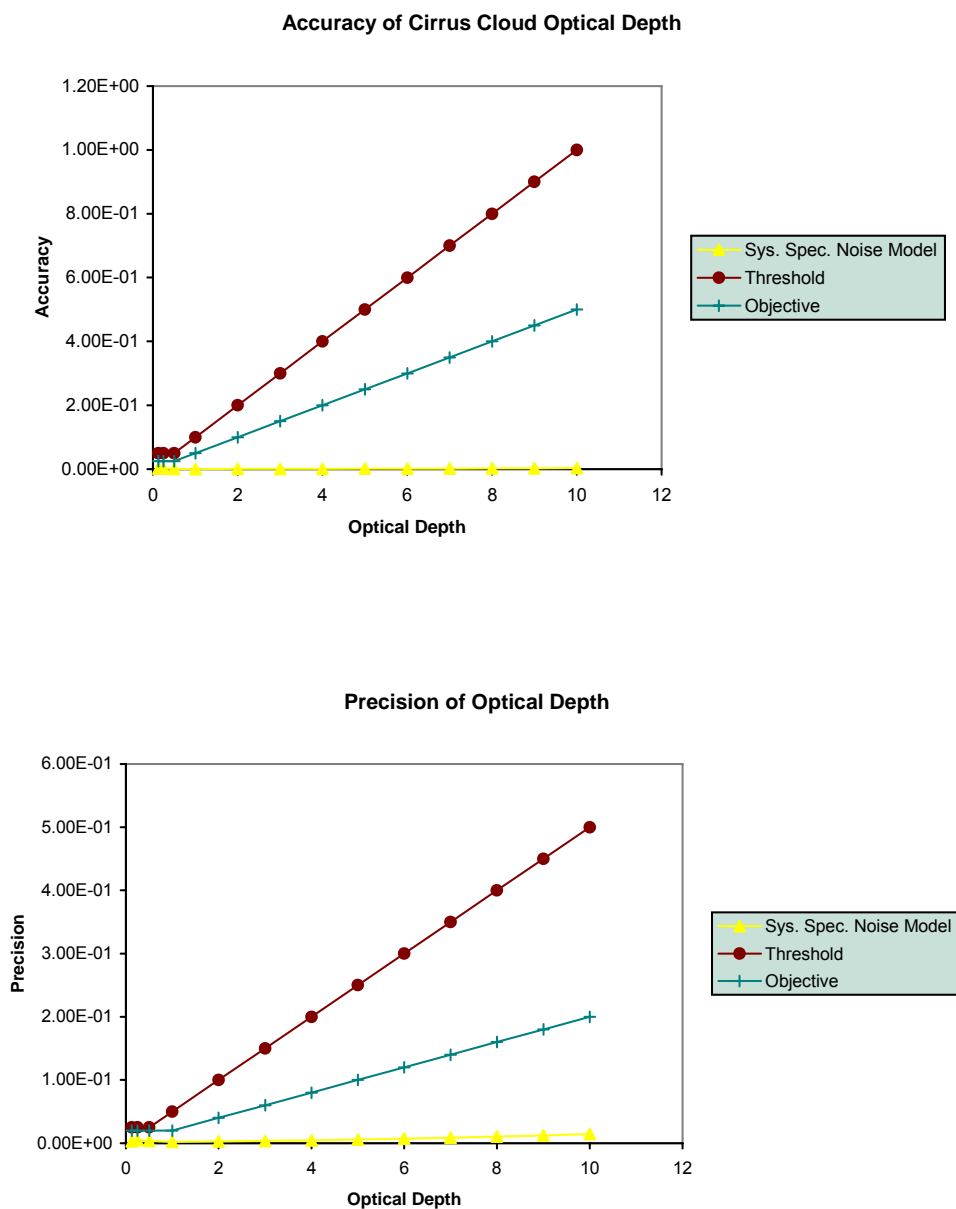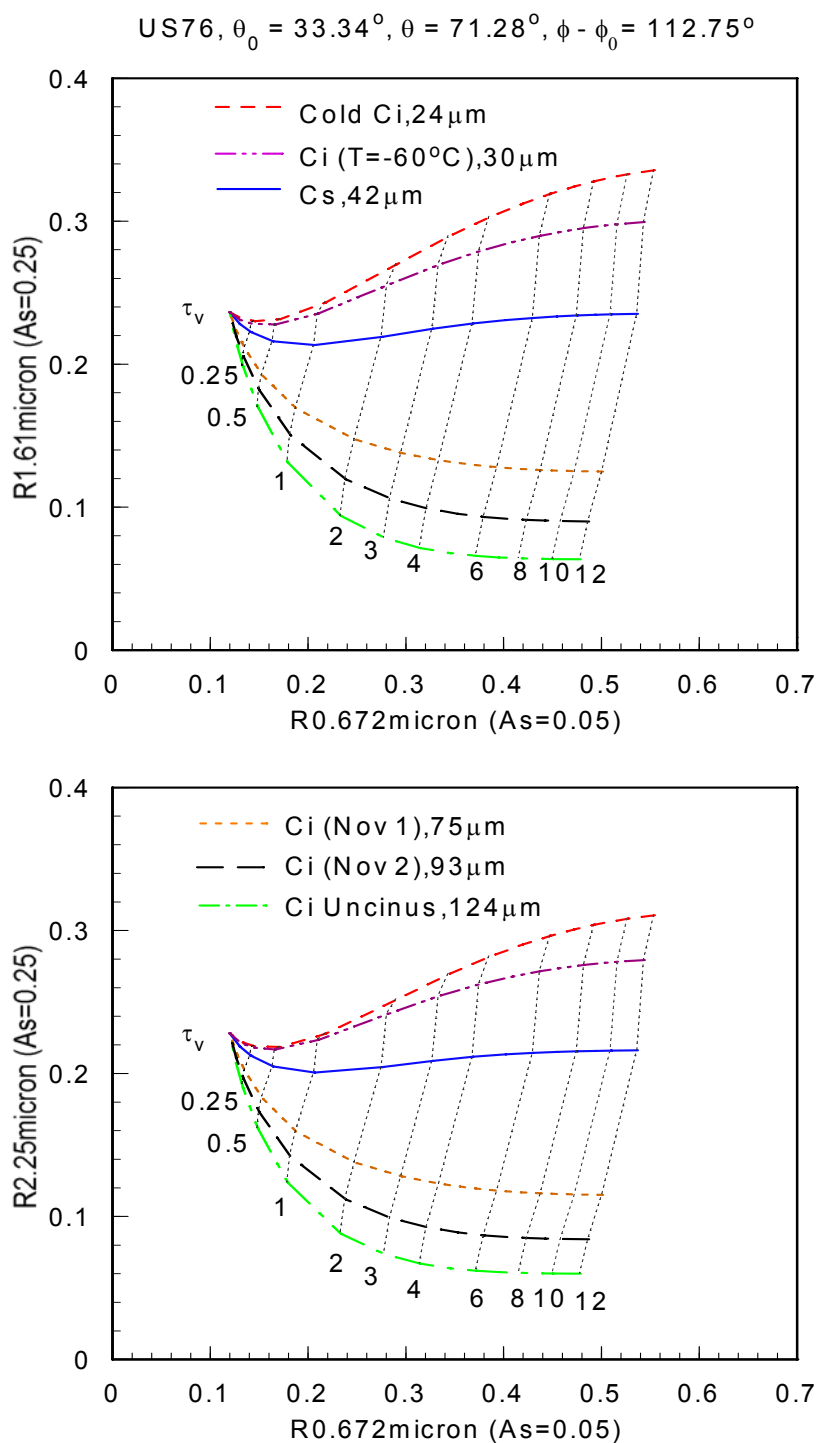
Figure 28. Display of the 0.672-1.61μm (top) and 0.672-2.25μm (bottom) Reflectance Correlations for Cirrus Cloud in Tropical Atmosphere, Sensor at Nadir.

Accuracy of Optical Depth

Precision of Optical Depth

Figure 29. Accuracy (top) and Precision (bottom) of Retrieved Optical Depths from the Solar Algorithm for Cirrus Cloud in Tropical Atmosphere, Sensor at Nadir.

Cirrus Cloud in Sub-Arctic Atmosphere with Sensor at Nadir

 Figure 30 shows the two-dimensional correlation for the reflectance pair: 1.2–1.61μm for the selected ice crystal size distributions and optical depths. The sensor is assumed to be pointing at nadir. Like Figure 21, these diagrams illustrate the information content of optical depth and mean effective size in the 1.2 and 1.61μm reflectances. However, the 1.2 and

1.61µm surface albedos are changed from 0.05 in Figure 21 to 0.164 and 0.0 respectively to simulate the ice/snow surface condition. Thus, the shape of the correlation mesh in Figure 30 is different than that in Figure 21. This change of the shape of the correlation mesh does not affect the retrieval accuracy and precision. Display of the 1.2 and 1.61µm reflectance correlation shows that if the mean effective size of an ice cloud is larger than about 24µm but less than about 124µm, an accurate retrieval of ice crystal mean effective size can be achieved. Likewise, if the optical depth of an ice cloud is larger than about 0.5 but less than 12, an accurate retrieval of optical depth can also be obtained. Also noted is that the 1.2µm reflectance mainly depends on the optical depth, while the 1.61µm reflectance is primarily a function of mean ice crystal size for optically thick ice clouds. Consequently, data for these two channels can be utilized to determine both optical depth and mean effective ice crystal size.

Figure 31 shows the accuracy and precision of retrieved optical depths as functions of optical depth. These results are based on retrieval combinations of all possible optical depths and mean effective sizes. Two straight lines denote threshold (greater of 10 percent or 0.05) and objective (greater of 5 percent or 0.025) values. The accuracy of retrieved optical depths meets both the threshold and objective requirements for most selected values of optical depth. The precision of retrieved optical depths meets both the threshold (greater of 5 percent or 0.025) and objective (greater of 2 percent or 0.02) requirements for most selected values of optical depth. For very small optical depths (e.g., <0.5), both the accuracy and precision errors are close to threshold and objective requirements, but for larger optical depths, both the accuracy and precision errors are well below the threshold and objective curves. The small values of accuracy and precision errors again indicate that the solar algorithm is highly accurate and very stable in retrieving optical depths.
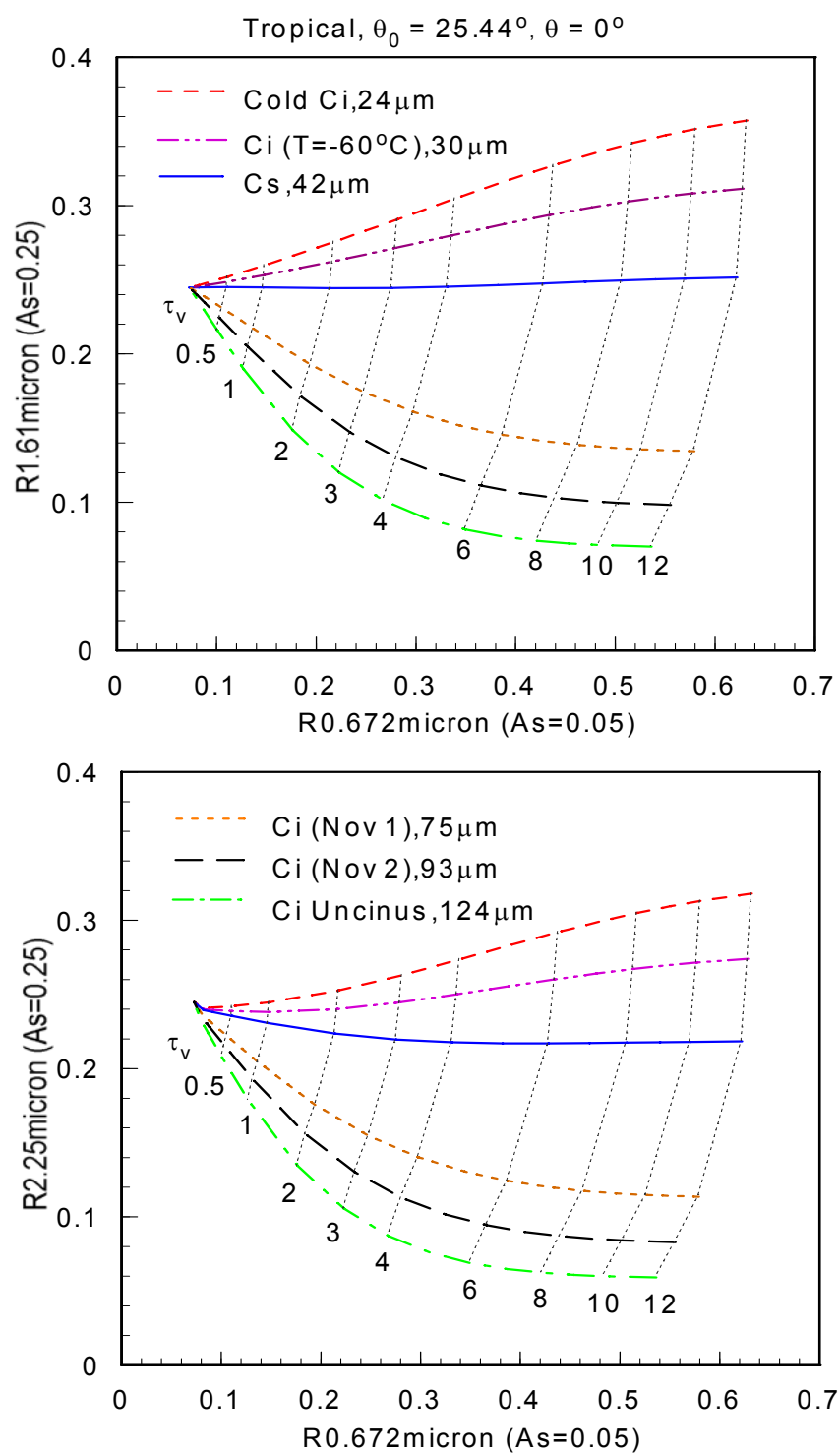
Figure 30. Display of the 1.2-1.61μm Reflectance Correlations for Cirrus Cloud in Sub-Arctic Atmosphere, Sensor at Nadir.

Accuracy of Optical Depth (Subarctic, Solar Ice Cloud, Nadir)

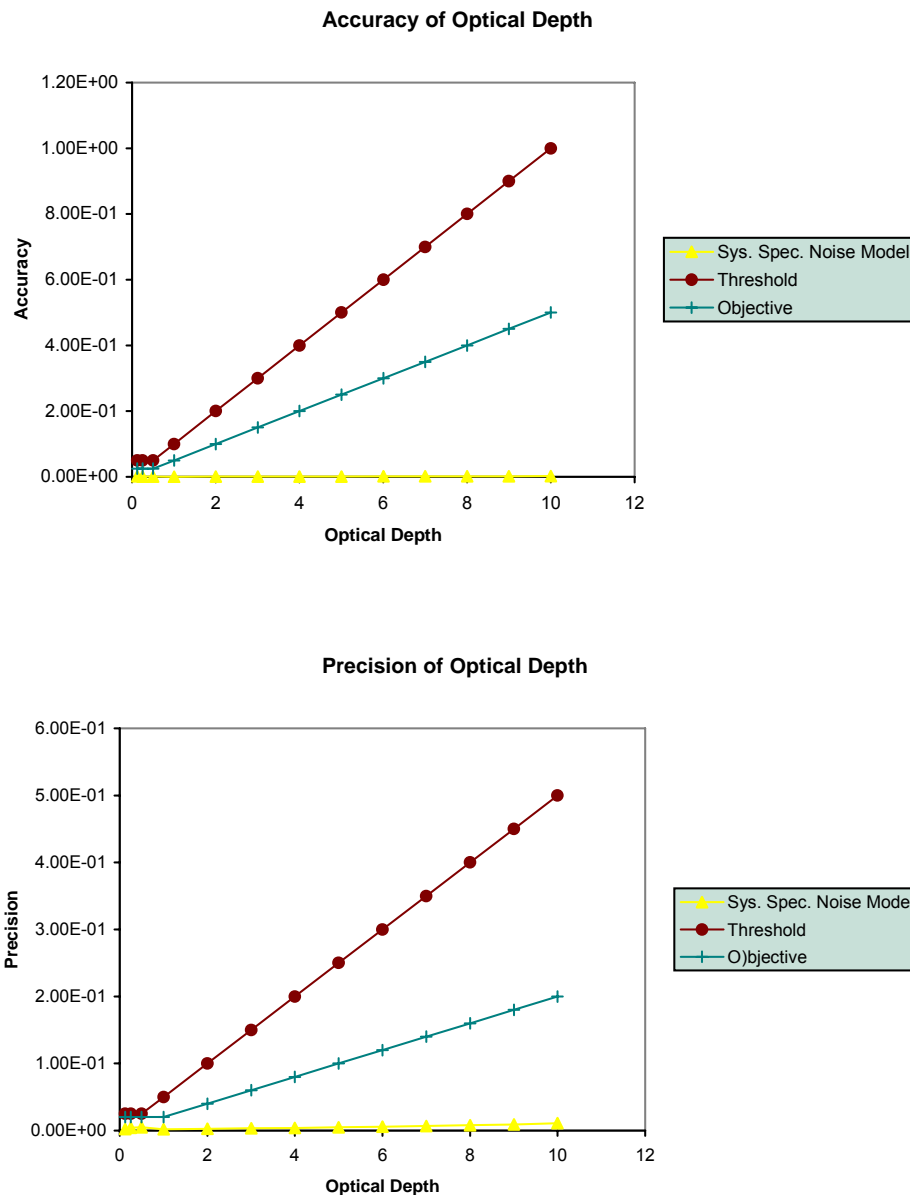**Precision of Optical Depth (Subarctic, Solar Ice cloud, Nadir)**

Figure 31. Accuracy (top) and Precision (bottom) of Retrieved Optical Depths from the Solar Algorithm for Cirrus Cloud in Sub-Arctic Atmosphere, Sensor at Nadir.

Cirrus Cloud in Desert Atmosphere with Sensor at Nadir

Figure 32 shows the two-dimensional correlations for the reflectance pairs: 0.672–1.61μm for the selected ice crystal size distributions and optical depths. The sensor is assumed to be pointing at nadir. Like Figure 21, these diagrams illustrate the information content of optical depth and mean effective size in the 0.672 and 1.61μm reflectances. However, both

the 0.672 and 1.61μm surface albedos are changed from 0.05 in Figure 21 to 0.40 and 0.64, respectively, to simulate the land surface condition. Thus, the shape of the correlation mesh in Figure 32 is different than that in Figure 21. This change of the shape of the correlation mesh does not affect the retrieval accuracy and precision. Display of the 0.672 and 1.61μm reflectance correlation shows that if the mean effective size of an ice cloud is larger than about 24μm but less than about 124μm, an accurate retrieval of ice crystal mean effective size can be achieved. Likewise, if the optical depth of an ice cloud is larger than about 0.5 but less than 12, an accurate retrieval of optical depth can also be obtained. Also noted is that the 0.672μm reflectance mainly depends on the optical depth, while the 1.61μm reflectances are primarily functions of mean ice crystal size for optically thick ice clouds. Consequently, data for these two channels can be utilized to determine both optical depth and mean effective ice crystal size.

Figure 33 shows the accuracy and precision of retrieved optical depths as functions of optical depth. These results are based on retrieval combinations of all possible optical depths and mean effective sizes. Two straight lines denote threshold (greater of 10 percent or 0.05) and objective (greater of 5 percent or 0.025) values. The accuracy of retrieved optical depths meets both the threshold and objective requirements for most selected values of optical depth. The precision of retrieved optical depths meets the threshold (greater of 5 percent or 0.025) requirements for most selected values of optical depth. The small values of accuracy and precision errors again indicate that the solar algorithm is highly accurate and very stable in retrieving optical depths.
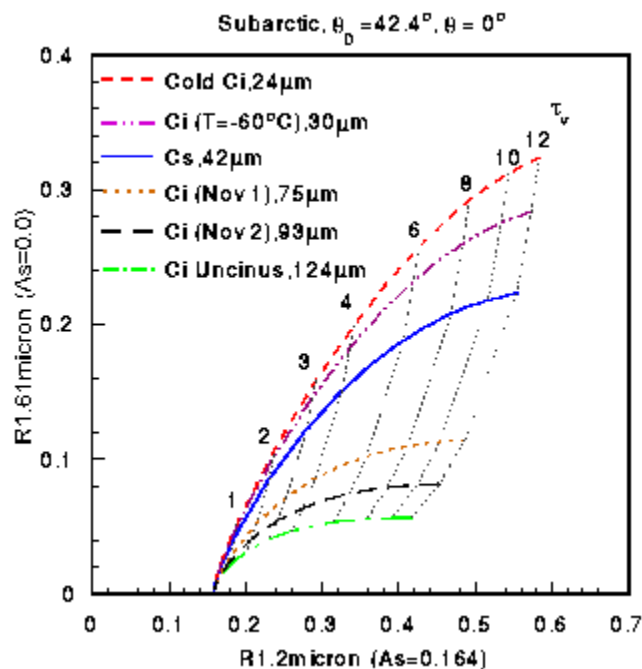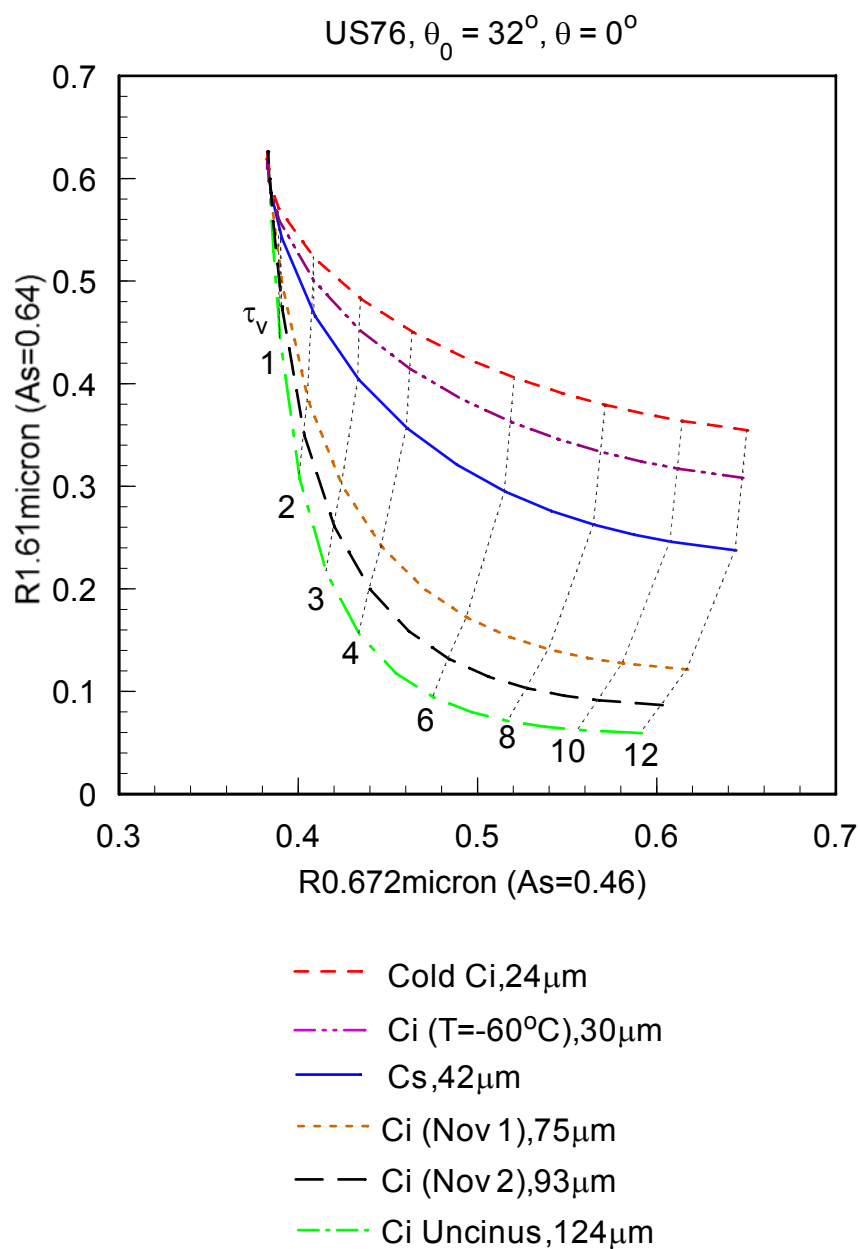
Figure 32. Display of the 0.672-1.61μm Reflectance Correlations for Cirrus Cloud in Desert Atmosphere, Sensor at Nadir.

Accuracy of Optical Depth (Desert, US Standard Atm., Solar Ice Clouds, Nadir)

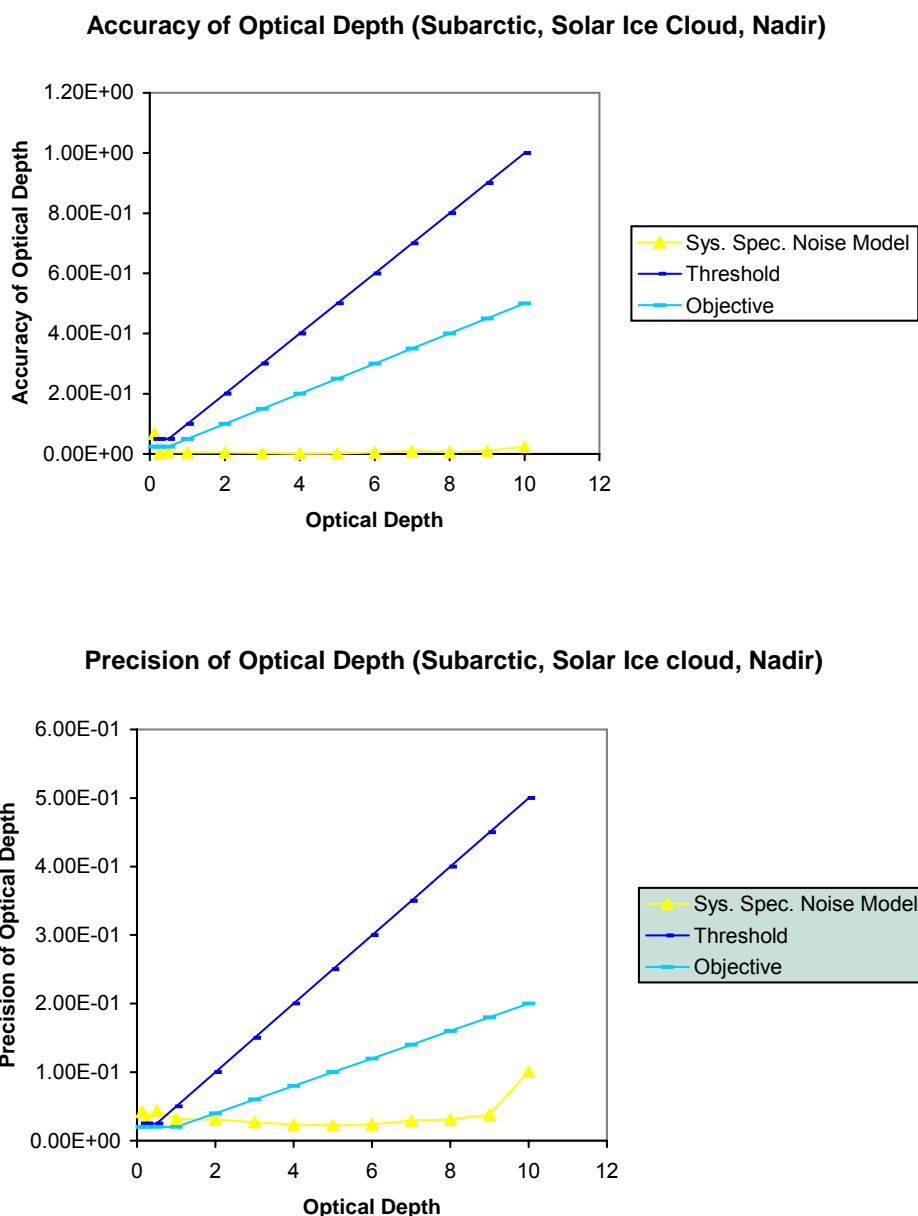**Precision of Optical Depth (Desert, US Standard Atmosphere, Solar Ice Cloud, Nadir)**

Figure 33. Accuracy (top) and Precision (bottom) of Retrieved Optical Depths from the Solar Algorithm for Cirrus Cloud in Desert Atmosphere, Sensor at Nadir.

Water Cloud in US Standard Atmosphere, Sensor at Nadir

Figure 34 shows the two-dimensional correlations for the reflectance pairs: $0.672–1.61\mu m$ and $0.672–2.25\mu m$ for the selected water droplet effective radii and optical depths. The sensor is assumed to be pointing at nadir. These diagrams illustrate the information content of optical depth and droplet effective radius in the 0.672, 1.61 and $2.25\mu m$ reflectances. Both

the 1.61 and 2.25μm surface albedos are set at 0.05 as in Figure 21 to approximately simulate the ocean surface condition. Thus, the shape of the correlation mesh in Figure 34 is similar to that in Figure 21. This similarity in the shape of the correlation mesh causes the retrieval accuracy and precision to be close to those for cirrus clouds in US Standard Atmosphere with sensor pointing at nadir. Display of the 0.672 and 1.61μm reflectance correlation shows that if the droplet effective radius of a water cloud is larger than about 4μm but less than about 30μm, an accurate retrieval of water droplet effective radius can be achieved.

The curves of 2 and 3μm partially overlap those of 4 and 6μm. Therefore, if the droplet effective size is less than 4μm, the retrieved optical depths may be in error, because the retrieval scheme will take the data as from a cloud of 5 and 6μm. If the optical depth of an ice cloud is larger than about 0.5 but less than 12, an accurate retrieval of optical depth can also be obtained. It is noted that the 0.672μm reflectance mainly depends on the optical depth, while the 1.61 and 2.25μm reflectances are primarily functions of mean droplet radius for optically thick water clouds. Consequently, data from these three channels can be utilized to determine both optical depth and droplet effective radius.

Figure 35 show the accuracy and precision of retrieved optical depths as functions of optical depth. These results are based on retrievals of combinations of all possible optical depths and mean effective sizes. Two straight lines denote threshold (greater of 10 percent or 0.05) and objective (greater of 5 percent or 0.025) values. The accuracy of retrieved optical depths meets both the threshold and objective requirements for most selected values of optical depth. The precision of retrieved optical depths meets both the threshold (greater of 5 percent or 0.025) and objective (greater of 2 percent or 0.02) requirements for most selected values of optical depth. For very small optical depths (e.g., <0.5), both the accuracy and precision errors are close to threshold and objective requirements, but for larger optical depths, both the accuracy and precision errors are well below the threshold and objective curves. The small values of accuracy and precision errors again indicate that the solar algorithm is highly accurate and very stable in retrieving optical depths for water clouds for the US Standard Atmosphere with the sensor pointing at nadir.
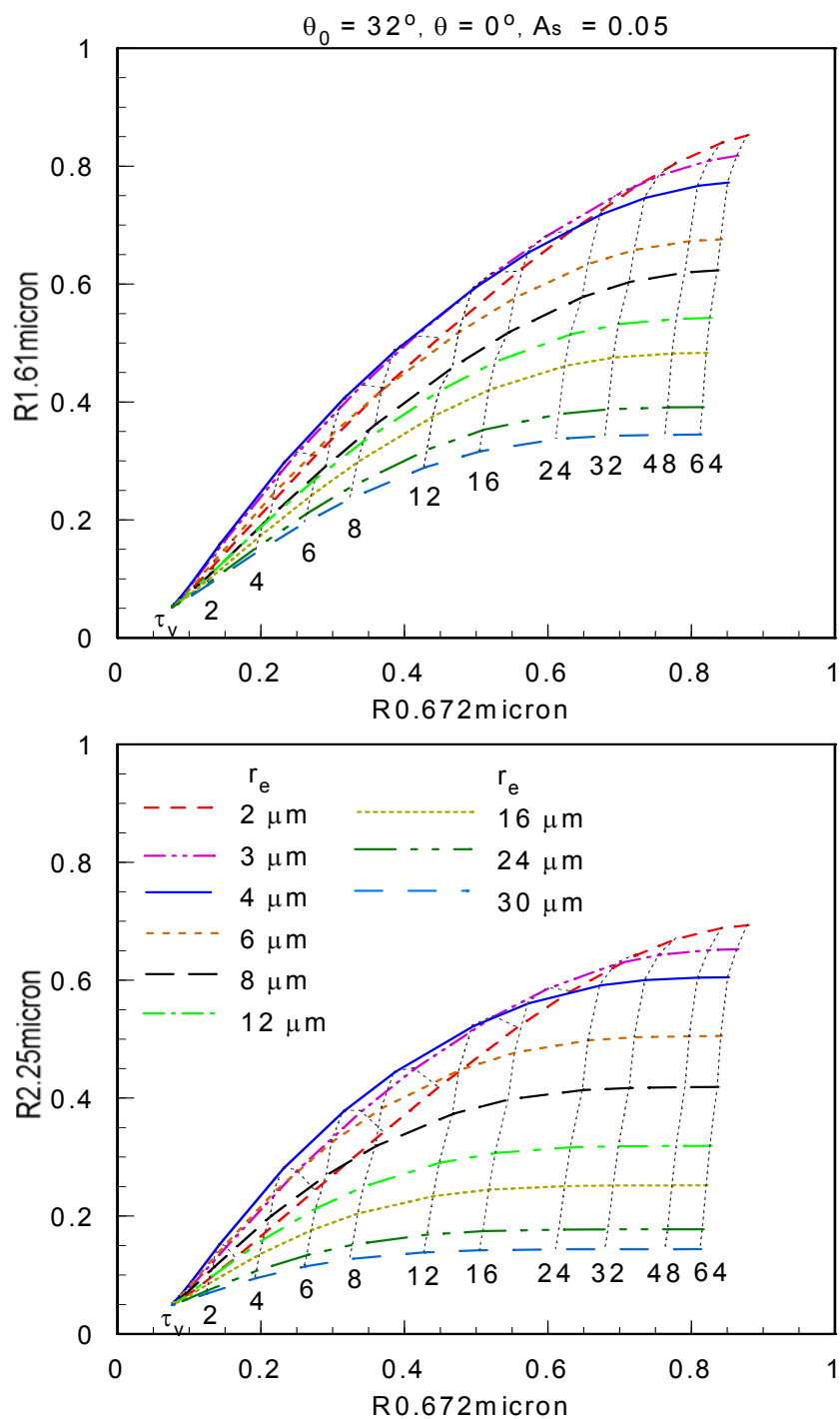
Figure 34. Display of the 0.672-1.61μm (top) and 0.672-2.25μm (bottom) Reflectance Correlations for Water Cloud in US Standard Atmosphere, Sensor at Nadir.

Accuracy of Optical Depth for Water Cloud at Nadir

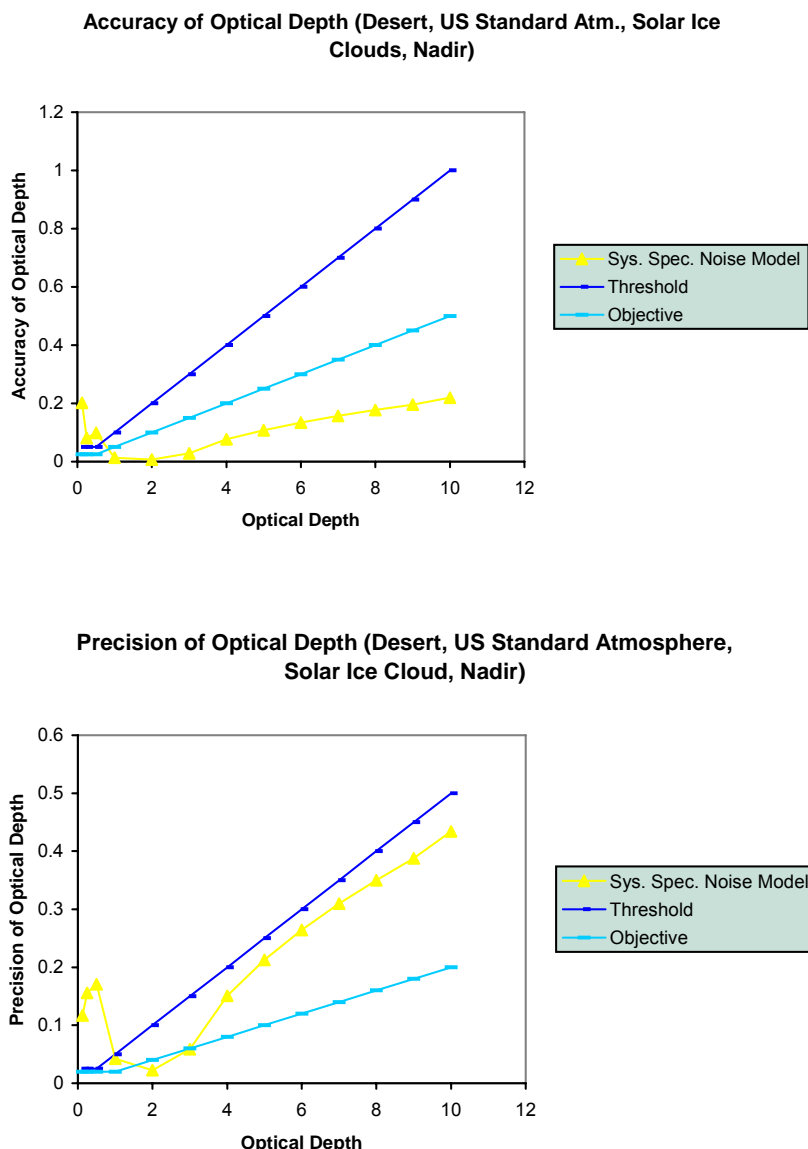**Precision of Optical Depth for Water Cloud at nadir**

Figure 35. Accuracy (top) and Precision (bottom) of Retrieved Optical Depths from the Solar Algorithm for Water Cloud in US Standard Atmosphere, Sensor at Nadir.

3.4.1.2 Nighttime Results

Cirrus Cloud in US Standard Atmosphere, Sensor at Nadir

Figure 36 shows the accuracy and precision of retrieved optical depths from the nighttime IR algorithm as a function of optical depth. These results are based on retrieval combinations of optical depths between 0.125 and 7 and of mean effective sizes between 20 and 100μm. Two straight lines denote threshold (greater of 10 percent or 0.05) and objective (greater of 5 percent or 0.025) values. The accuracy of the retrieved optical depths meets the threshold requirement for optical depths up to 6. The accuracy does not meet the threshold for optical depths larger than 6, mainly because the exponential relationship between IR emissivity and optical depth. For optically thick clouds, the IR emissivity approaches one, so that a small error in the retrieved emissivity can lead to a large error in optical depth. The precision of retrieved optical depths meets the threshold (greater of 5 percent or 0.025) requirement for optical depths up to 7. Precision becomes less satisfactory for larger optical depths, because the sensitivity of emissivity toward optical depth is reduced due to the exponential relationship between the emissivity and optical depth.

Cirrus Cloud in US Standard Atmosphere, Sensor pointing Off-Nadir

Figure 37 shows the accuracy and precision of retrieved optical depths from the nighttime IR algorithm as a function of optical depth. These results are based on retrieval combinations of optical depths between 0.125 and 7 and of mean effective sizes between 20 and 100μm. The straight lines denote threshold (greater of 10 percent or 0.05) and objective (greater of 5 percent or 0.025) values. The accuracy of the retrieved optical depths meets the threshold requirement for optical depths up to 7. The accuracy does not meet the threshold for optical depths larger than 7, mainly due to the exponential relationship between IR emissivity and optical depth. For optically thick clouds, the IR emissivity approaches one, so that a small error in the retrieved emissivity can lead to a large error in optical depth. The precision of retrieved optical depths meets the threshold (greater of 5 percent or 0.025) requirement for optical depths up to 5. Precision becomes less satisfactory for larger optical depths, because sensitivity of emissivity toward optical depth is reduced due to the exponential relationship between the emissivity and optical depth.

Accuracy of Optical Depth

Precision of Optical Depth for De = 41.5 um

Figure 36. Accuracy (top) and Precision (bottom) of Retrieved Optical Depths from the IR Algorithm for Cirrus Cloud in US Standard Atmosphere, Sensor at Nadir.

**Accuracy of Cirrus Cloud Optical Depth from Nighttime IR
Algorithm for US Standard Atmosphere at theta=40 deg**
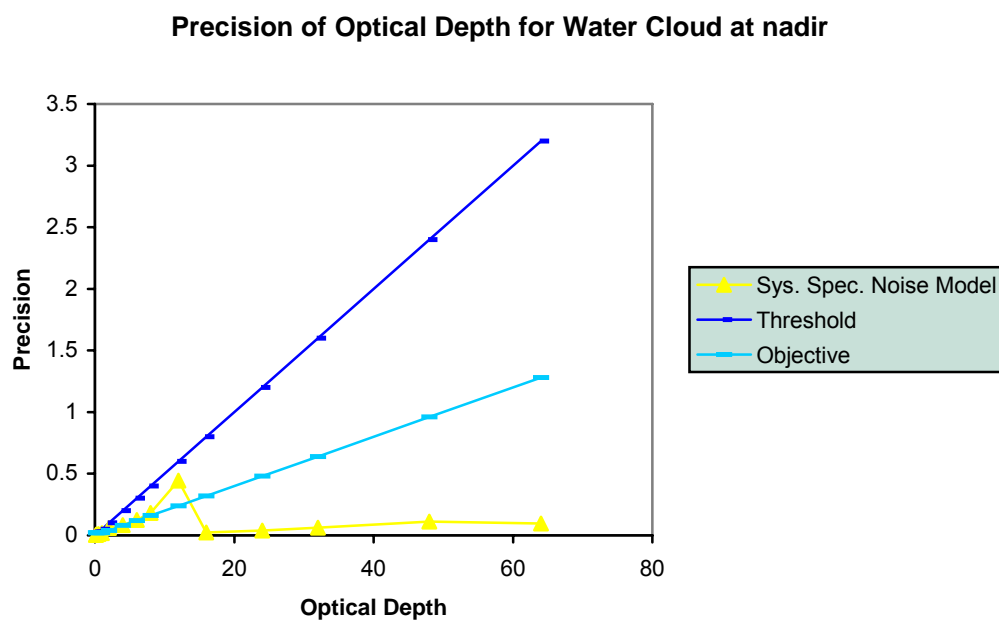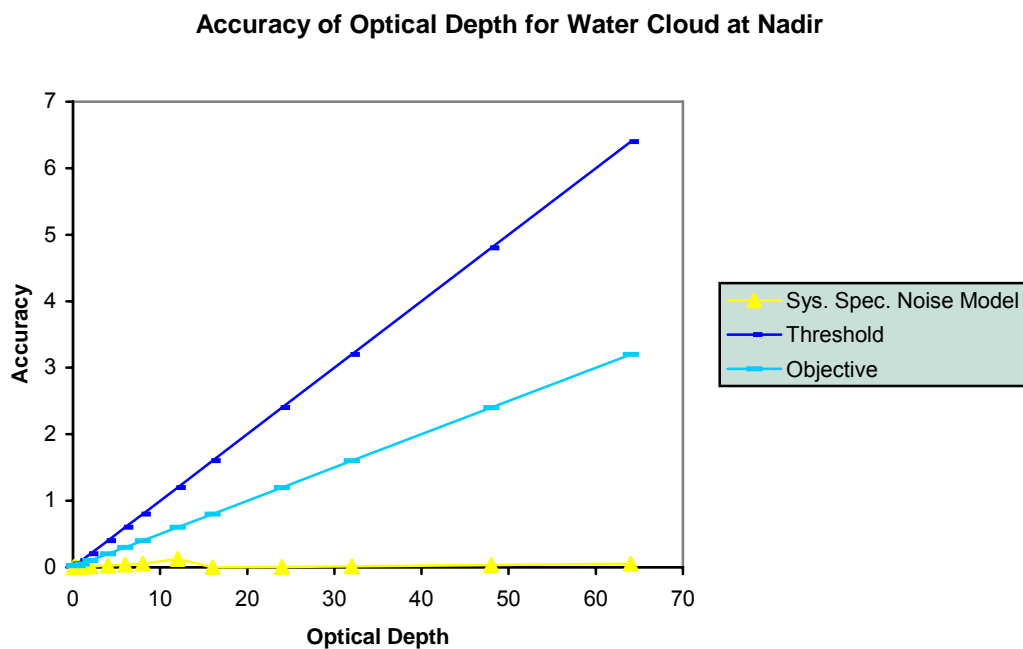

Precision of Optical Depth

**Figure 37. Accuracy (top) and Precision (bottom) of Retrieved Optical Depths from
the IR Algorithm for Cirrus Cloud in US Standard Atmosphere, Sensor pointing Off-
Nadir.**

Accuracy of Optical Depth (US Standard Atm., IR Ice Cloud, Edge)

Precision of Optical Depth (US Standard Atm., IR Ice Cloud, Edge)

Figure 38. Accuracy (top) and Precision (bottom) of Retrieved Optical Depths from the IR Algorithm for Cirrus Cloud in US Standard Atmosphere, Sensor at Edge-of-Scan.

Cirrus Cloud in US Standard Atmosphere, Sensor at Edge-of-Scan

Figure 38 shows the accuracy and precision of retrieved optical depths from the nighttime IR algorithm as a function of optical depth. These results are based on retrieval combinations of optical depths between 0.125 and 5 and of mean effective sizes between 20 and 100μm. The straight lines denote threshold (greater of 10 percent or 0.05) and objective (greater of 5 percent or 0.025) values. The accuracy of the retrieved optical depths meets the threshold requirement for optical depths up to 3. The accuracy does not meet the threshold for optical depths larger than 3, mainly due to the exponential relationship between the IR emissivity and the optical depth. For optically thick clouds, the IR emissivity approaches one, so that a small error in the retrieved emissivity can lead to a large error in optical depth. The precision of retrieved optical depths meets the threshold (greater of 5 percent or 0.025) requirement for optical depths up to 3. Precision becomes less satisfactory for larger optical depths, because sensitivity of emissivity toward optical depth is reduced due to the exponential relationship between the emissivity and optical depth.

Cirrus Cloud in Tropical Atmosphere, Sensor at Nadir

Figure 39 shows the accuracy and precision of retrieved optical depths from the nighttime IR algorithm as a function of optical depth. These results are based on retrieval combinations of optical depths between 0.125 and 8 and of mean effective sizes between 20 and 100μm. The straight lines denote threshold (greater of 10 percent or 0.05) and objective (greater of 5 percent or 0.025) values. The accuracy of the retrieved optical depths meets the threshold requirement for optical depths up to 8. The accuracy does not meet the threshold for optical depths larger than 8, mainly because the exponential relationship between the IR emissivity and the optical depth. For optically thick clouds, the IR emissivity approaches one, so that a small error in the retrieved emissivity can lead to a large error in derived optical depth. These results are based on retrievals of combinations of optical depths between 0.125 and 7 for the mean effective size of 41.5μm. The precision of retrieved optical depths meets the threshold (greater of 5 percent or 0.025) requirement for optical depths up to 8. Precision becomes less satisfactory for larger optical depths, because sensitivity of emissivity toward optical depth is reduced due to the exponential relationship between the emissivity and optical depth
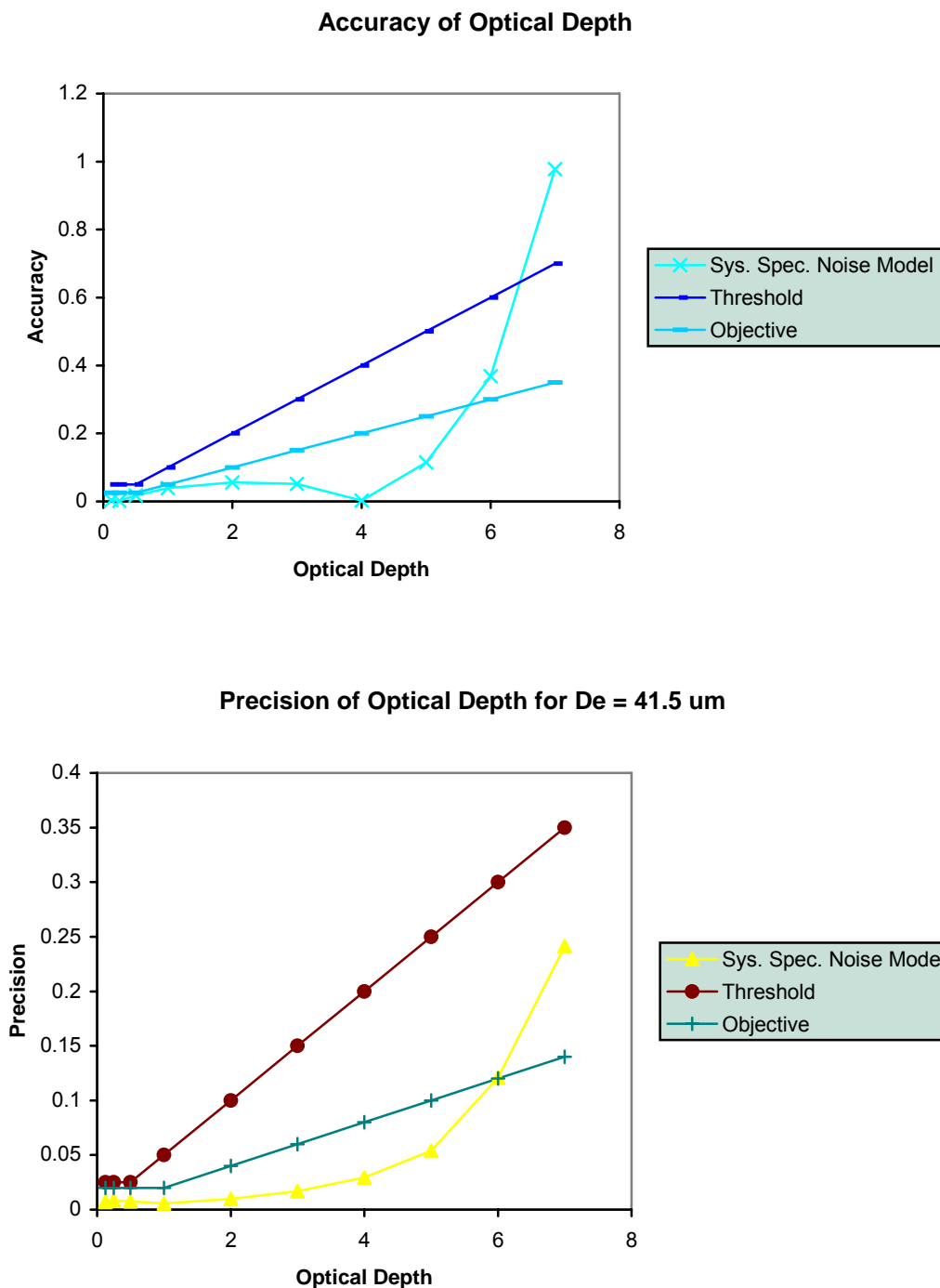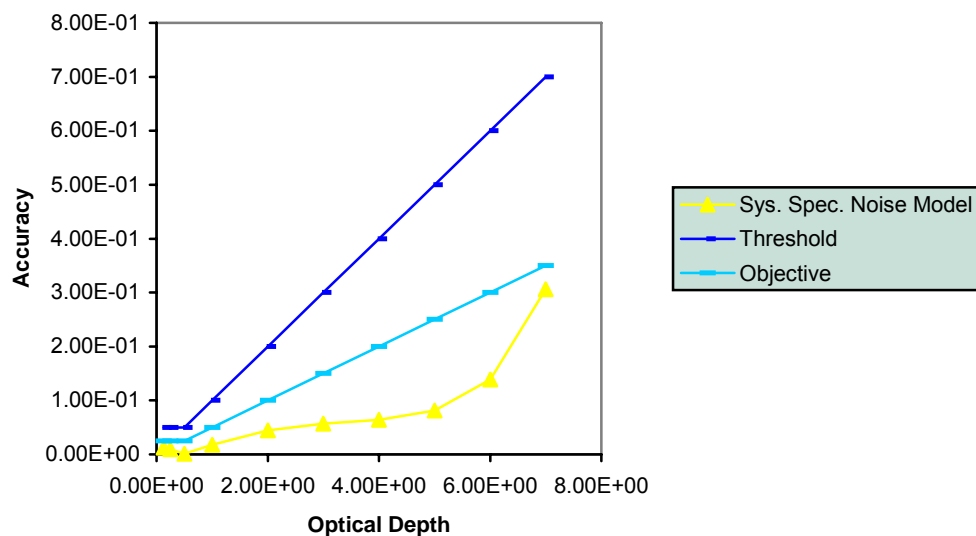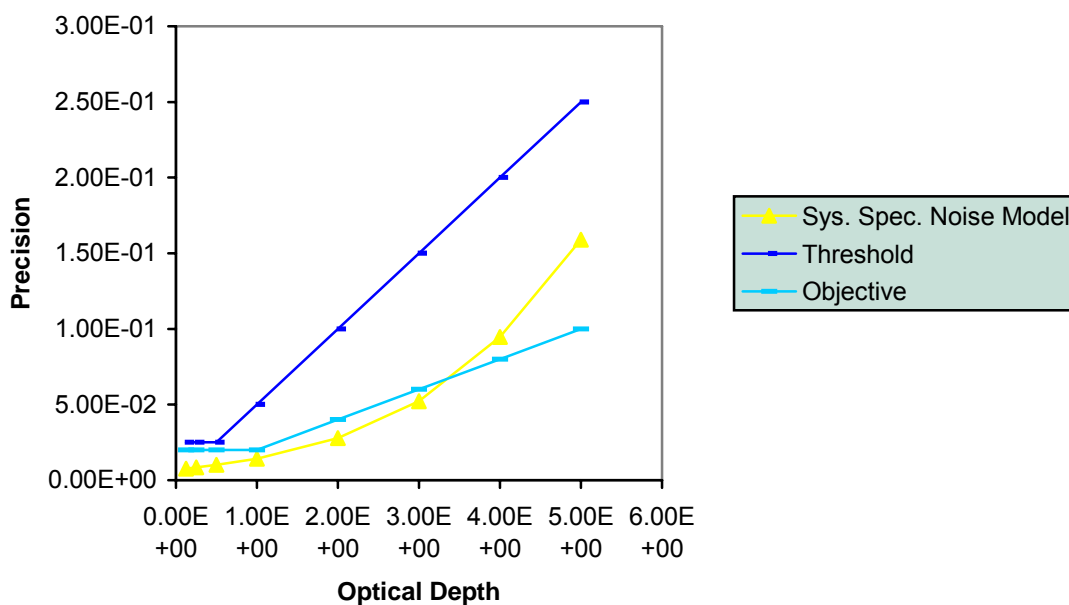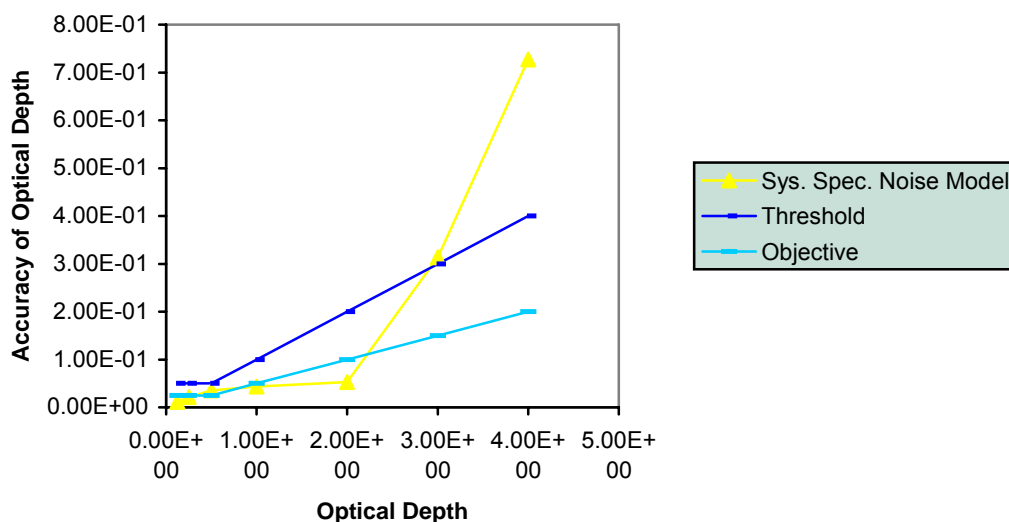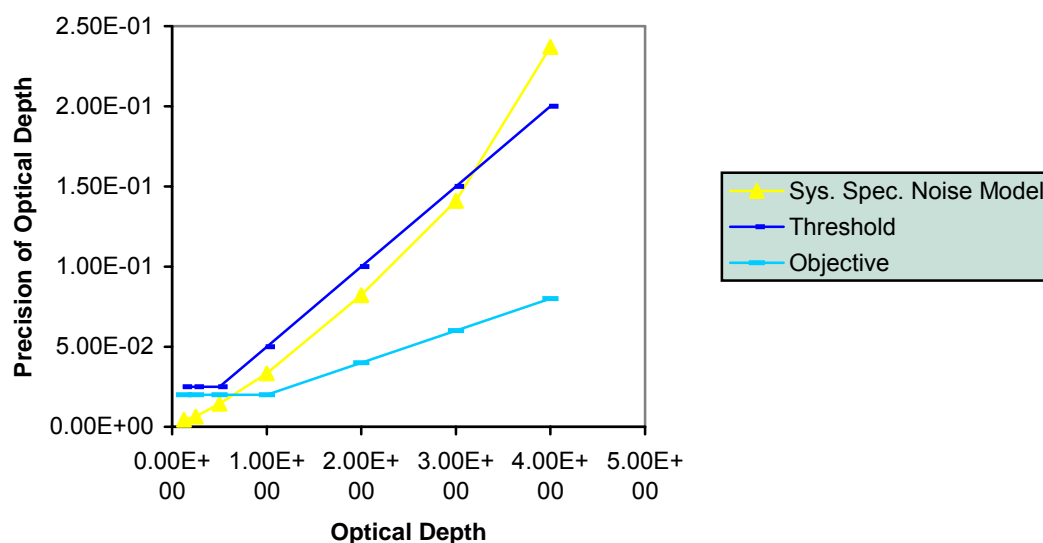
Water Cloud in US Standard Atmosphere, Sensor at Nadir

Figure 40 shows the accuracy and precision of retrieved optical depths from the nighttime IR algorithm as a function of optical depth for the no-noise case. These results are based on retrievals of combinations of optical depths between 0.125 and 10 and of effective particle sizes between 2 and 12 μm. Two straight lines denote threshold (greater of 10 percent or 0.05) and objective (greater of 5 percent or 0.025) values. The accuracy of the retrieved optical depths meets the threshold requirement for optical depths up to 5. For optical depths larger than 5, the IR emissivity becomes less sensitivity to the optical depth. For optically thick clouds, the IR emissivity approaches one, so that a small error in the retrieved emissivity can lead to a large error in optical depth. The precision of retrieved optical depths meets the threshold (greater of 5 percent or 0.025) requirement for optical depths up to 3.

Precision becomes less satisfactory for larger optical depths, because of lack of sensitivity of emissivity toward optical depth.

Accuracy of Optical Depth

Precision of Optical Depth
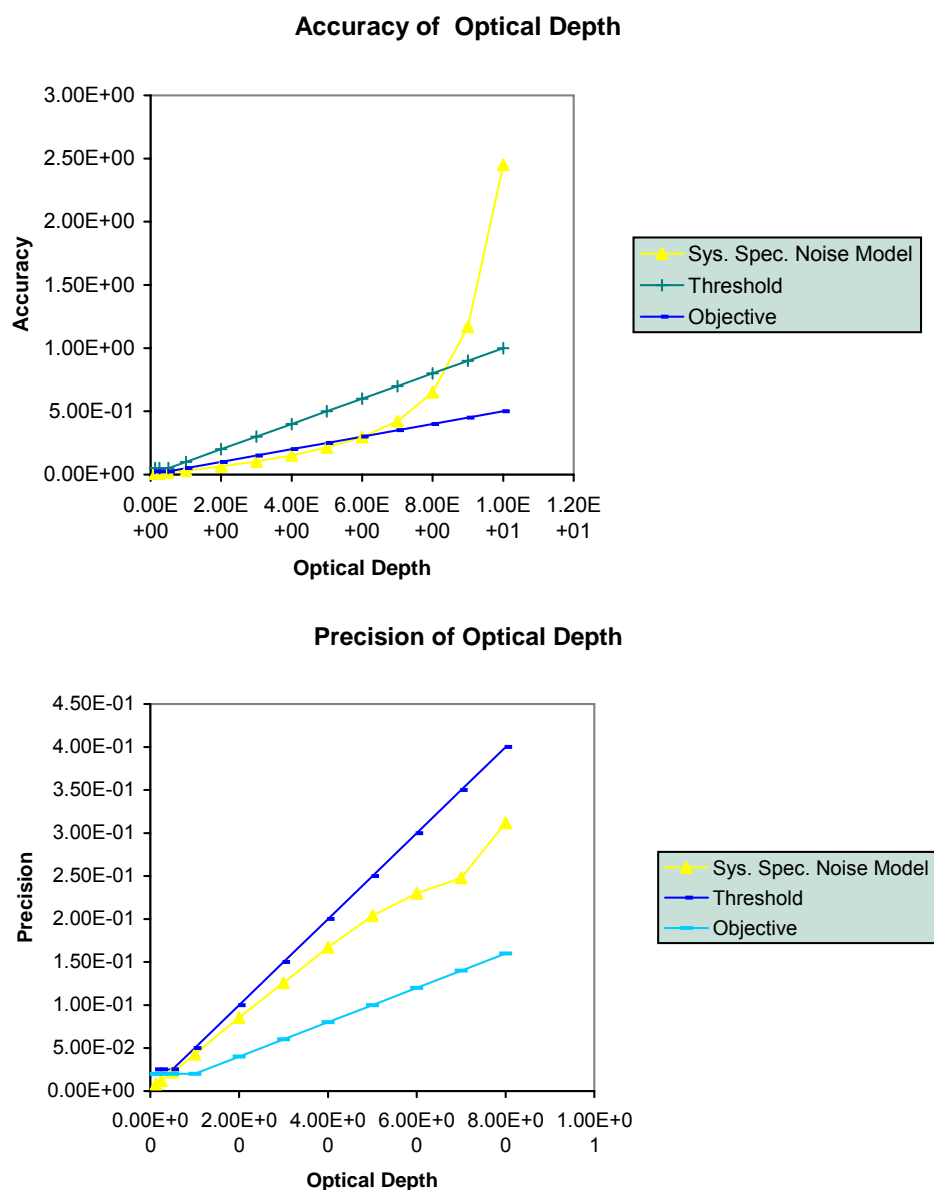
Figure 39. Accuracy (top) and Precision (bottom) of Retrieved Optical Depths from the IR Algorithm for Cirrus Cloud in Tropical Atmosphere, Sensor at Edge-of-Scan.

Accuracy of nighttime IR water COD

Precison of Nighttime IR Water COD

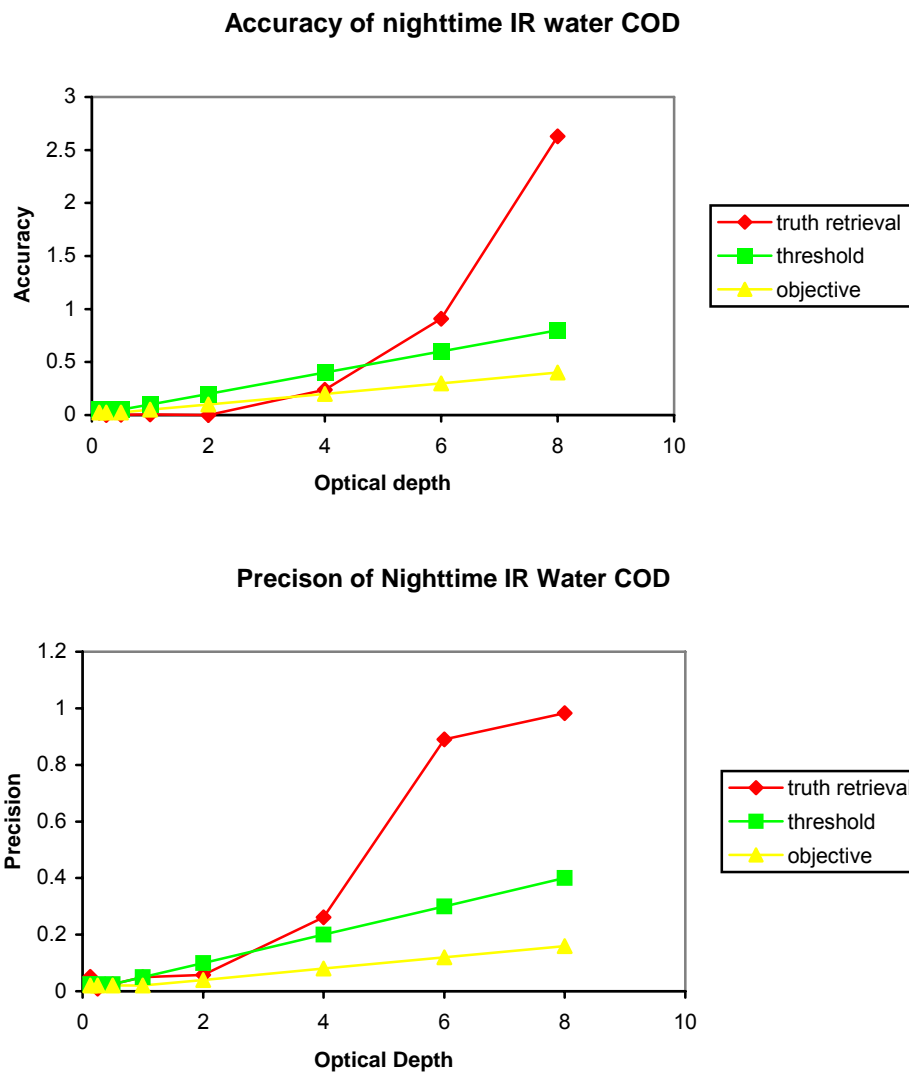**Figure 40. Accuracy (top) and Precision (bottom) of Retrieved Optical Depths from the IR Algorithm for Water Cloud in US Standard Atmosphere for No-Noise Retrievals, Sensor at Nadir.**

3.4.1.3
Recommendations

- For daytime retrievals, the VIIRS noise model is generally suitable for retrieving cloud optical depth using the 1.61μm and either the 0.672μm (non-snow/ice surface) or 1.2μm (snow/ice surface) channels.

- For nighttime retrievals using the IR algorithm, the VIIRS noise model is generally suitable for retrieving cloud optical depth using the 3.7 and $10.7625\mu m$ channels.

3.4.2 Error Budget Studies

3.4.2.1 Algorithm Specific Errors in the Cloud Module

Algorithm specific errors, otherwise referred to as "intrinsic errors", for the cloud module are discussed below. We define intrinsic errors as errors internal to the algorithms, related to algorithm assumptions or simplifications. Table 8.2-1 of the Error Budget Document gives various intrinsic error sources and their impacts on the retrievals. At this time, only truth retrieval errors are considered. Most of the other intrinsic errors have not been included in the EBs.

3.4.2.2 Input Error Sources

There are a number of input parameters to the cloud algorithms. We have attempted to quantify the impact of errors in these input data sources on retrieval accuracy. Our approach has been to develop partial derivatives that quantify the change in a metric value (e.g., measurement accuracy metric, precision metric or uncertainty metric) to a small perturbation in the input parameter. These partial derivatives are then multiplied by a "standard error", which captures the anticipated RMS error in that input parameter. The product of the partial derivative with the standard error gives an estimate of an input parameter's contribution to the error budget for a given EDR. These error budgets have been developed by applying the retrieval algorithms to scenes. In general, these scenes cover approximately a 100km x 100km area. The spatial distribution of clouds within the area is determined through the use of TASC's Cloud Scene Simulation Model (CSSM). Processing of CSSM data yields a 2-D distribution of visible cloud optical thickness at 0.1km spatial resolution for a cloud layer. We assert an atmospheric scenario which includes sensor geometry, surface characteristics, atmospheric profiles and cloud base height, cloud top height and effective particle size. These atmospheric characteristics are used to develop RT look-up tables (LUTs) for the scenario of VIIRS channel radiances as a function of cloud effective particle size and optical depth. These RT LUTs are used to create radiance images for the scene for each VIIRS channel used by the cloud algorithms, by associating a radiance value from the LUT with the optical depth value associated with each 0.1km data point. The 0.1km data are aggregated to the VIIRS pixel size. Perturbations to radiances, such as BBR, MTF, geolocation and calibration are applied to the 0.1km prior to aggregation. Perturbations to scenario parameters are effected by re-computing the radiance LUTs. The perturbed radiances are then applied to the scene. The unperturbed radiances are used to develop so-called truth retrievals. The retrievals using the perturbed radiances are used to compute SRD metrics and the partial derivatives. This methodology was used to develop EBs for all cloud EDRS, except CBH and CCL. The techniques used for the CBH and CCL EDRs are described in their respective sections.

Table 8.3-1 of the Error Budget Document provides a general list of input parameters used by the cloud algorithms. A given retrieval algorithm may not use all input parameters. The input parameters are divided into three groups: surface parameters, atmospheric profiles and EDRs and SDRs. Note that error contributions for the VCM and Cloud Phase algorithms will be introduced once these models have been tuned for the new bands. Previous experience with these models suggests that the impact on the error budgets should be small.

3.4.2.3   Sensor Error Sources

Several attributes of the sensor were assumed throughout the cloud EDR EBs. These are listed below:

- Sensor Noise Model
- MTF Model: 5
- Band-to-Band Registration (BBR): 0.2 pixel shift
- Geolocation: 0.2 pixel shift
- Absolute Radiometric Calibration (ARA): 0.4% IR channels, 2% solar channels
- Pixel sizes: nadir (753m, 1160m and 1600m)

The BBR and geolocation errors and MTF model were applied to the 0.1km radiance data prior to aggregation.

3.4.2.4   Specified and Predicted Performance

The Error Budgets for COT are divided into four areas consistent with the specification and with the four algorithms used to produce this EDR: daytime water cloud, daytime ice cloud, nighttime ice cloud and nighttime water cloud. The specified and predicted performances based on Error Budget analyses for these four cloud types are provided in Section 6.7.3 of the Error Budget Document (Raytheon Document Y3249.V3) and in Ou *et al.* (2003).

3.5 ALGORITHM SENSITIVITY STUDIES ON RETRIEVALS OF EFFECTIVE PARTICLE SIZE

The sensitivity studies on the retrievals of effective particle size were carried out using the cloud optical properties retrieval algorithm under development at UCLA. The algorithm sensitivity studies were carried out using the results generated by the radiative transfer model for seven separate scenarios. These scenarios form the basis for defining the input parameters required by the radiative transfer model. They are:

(1) Cirrus cloud in US Standard Atmosphere, sensor at nadir.

(2) Cirrus cloud in US Standard Atmosphere, sensor pointing off-nadir.

(3) Cirrus cloud in US Standard Atmosphere, sensor at edge-of-scan.

(4) Cirrus cloud in Tropical Atmosphere, sensor at nadir.

(5) Cirrus cloud in Sub-Arctic Atmosphere, sensor at nadir.

(6) Cirrus cloud in Desert Atmosphere, sensor at nadir.

(7) Water cloud in US Standard Atmosphere, sensor at nadir.

For scenarios 1 through 5, synthetic retrievals for both daytime and nighttime conditions were carried out for combinations of input cirrus optical depths and effective particle sizes. For scenario 7, only synthetic retrievals for daytime conditions were carried out.

The LBLE radiative transfer model described in section 3.3.1.7 was used to generate simulated radiances. The input parameters for each scenario have been given in Table 8. For all scenarios, the solar zenith angle is fixed at 32°, the nominal date and location are based on the VIIRS simulated orbit on 1 May at 40° North. For a given specification of atmospheric profile, sun-sensor geometry, retrieval channel characteristics (including central wavelength, bandwidth and response function), cloud type, altitude and thickness, as well as surface albedo and emissivity, the radiative transfer calculations are performed for a wide range of selected visible optical depths and mean effective ice crystal sizes or water droplet radii. For cirrus clouds, the optical depths chosen are: 0.125, 0.25, 0.5, 1, 2, 3, 4, 5, 6, 7, 8, 9, 10 and 12. The mean effective sizes chosen are: 23.9, 30.4, 41.5, 71, and 93μm. For water clouds the optical depths selected are: 0.125, 0.25, 0.5, 1, 2, 3, 4, 5, 6, 8, 12, 16, 24, 32, 48, and 64. The mean droplet radii selected are: 2, 3, 4, 6, 8, 12, 16, 24 and 30μm. Many radiance values are thus produced, and they are further processed to create data sets that are appropriate for the parameter retrieval algorithms and algorithm sensitivity tests.

This section addresses results of the algorithm sensitivity analyses for cloud effective particle sizes using the cirrus and water cloud IR and solar retrieval algorithms, which use VIIRS bands at 3.7 and 10.7625 m for IR algorithms and bands at 0.672, 1.24 and 1.61 m for solar algorithms, respectively. In the present work, the cirrus cloud retrieval algorithm retrieves mean effective size as defined in Equation 1. The ice crystal mean effective size is

in the dimension of width (equivalent to the dimension of diameter for a sphere, a cylindrical column or a circular plate), while according to the VIIRS SRD, the cloud effective particle size is defined in the dimension of radius (or half of the diameter for a sphere, a cylindrical column or a circular plate). We thus define the effective particle size for ice clouds to be half of the ice crystal mean effective size. Therefore the uncertainty of cloud effective particle size is also half of that for the ice crystal mean effective size. The water cloud retrieval algorithm retrieves effective droplet radius. We define the effective particle size for water clouds to be equal to the effective droplet radius. Illustrative results of these algorithm sensitivity analyses follow.

3.5.1 SNR Tests

The SNR tests address the impact of SNR on both pixel-level and image-level retrievals. The pixel-level retrievals are performed for a single pixel assuming various combinations of cloud optical depth and effective particle size. The imagery-level retrievals are performed for pixels aggregated (averaged) to the VIIRS SRD horizontal cell size (HCS). The required HCS is an EDR parameter; threshold and objective values are stated. The test results are presented separately for the solar and IR algorithms. To create data sets to support the pixel level SNR test, noise based on the System Specification noise model is added directly to the radiance contained in the radiance tables, and then retrievals are performed using the noise-added data in the tables. To guarantee sample sizes are sufficient to support tests, noise is randomly added to each radiance value 32 times. In effect, 32 noise perturbed radiance tables are created. Retrievals are performed using each of the 32 noise-added tables and the no-noise table. The results of the retrieval process are then statistically analyzed to compute the metrics described in the SRD (accuracy, precision, etc.).

3.5.1.1   Daytime Results

Cirrus Cloud in US Standard Atmosphere, Sensor at Nadir

Figure 41 shows the accuracy and precision of retrieved mean effective size as a function of mean effective size. These results are based on retrieval combinations of all possible optical depths (0 to 10) and mean effective sizes (20 to 100μm). Two lines denote threshold (greater of 10 percent or 4μm) and objective (greater of 5 percent or 2μm) values. The accuracy of retrieved mean effective sizes meets both the threshold and objective requirements across the range of mean effective size. The accuracy is about the same magnitude across the range of mean effective size. The precision of retrieved mean effective sizes meets the threshold requirement for the full range of mean effective sizes. The small accuracy and precision errors indicate that the solar algorithm is reasonably accurate and stable in retrieving mean effective sizes.

Figure 42 show the accuracy and precision of retrieved effective particle size as a function of mean effective size using the 0.672-2.25μm correlation. These results are based on retrieval combinations of all possible optical depths and mean effective sizes using the 0.672 and 2.25μm reflectance correlation. Two straight lines denote threshold (greater of 10 percent or

4μm) and objective (greater of 5 percent or 2μm) values. The accuracy of retrieved effective particle sizes meets both the threshold and objective requirements for most selected values of effective particle sizes. The precision of retrieved effective particle sizes meets the threshold (greater of 5 percent or 2μm) requirements for mean effective particle sizes between 25 and 70 m. For larger optical depths, both the accuracy and precision errors are close to zero. Figures 41 and 42 illustrate the superiority of the 1.61μm reflectance to the 2.25μm reflectance with respect to EPS retrieval. For the rest of the algorithm studies on the solar retrieval algorithm, we will only show results using the 0.672-1.61μm correlation.

Cirrus Cloud in US Standard Atmosphere, Sensor pointing Off-Nadir

Figure 43 shows the accuracy and precision of retrieved mean effective sizes as a function of mean effective size. These results are based on retrieval combinations of all possible optical depths (0 to 10) and mean effective sizes (20 to 100μm). Two lines denote threshold (greater of 10 percent or 4μm) and objective (greater of 5 percent or 2μm) values. The accuracy of retrieved mean effective size meets both the threshold and objective requirements for the range of mean effective sizes. The accuracy is about the same magnitude across the range of mean effective size. The precision of retrieved mean effective size meets both the threshold and objective requirements for the full range of mean effective sizes. The small accuracy and precision errors indicate that the solar algorithm is reasonably accurate and stable in retrieving mean effective sizes.

Cirrus Cloud in US Standard Atmosphere, Sensor at Edge-of-Scan

Figure 44 shows the accuracy and precision of retrieved mean effective size as a function of mean effective size. These results are based on retrieval combinations of all possible optical depths (0 to 10) and mean effective sizes (20 to 100μm). Two lines denote threshold (greater of 10 percent or 4μm) and objective (greater of 5 percent or 2μm) values. The accuracy of retrieved mean effective sizes meets both the threshold and objective requirements for the range of mean effective sizes. The accuracy is about the same magnitude across the range of mean effective size. The precision of retrieved mean effective sizes meets the threshold requirement for the full range of mean effective sizes. The precision of retrieved mean effective sizes meets the objective requirement for mean effective sizes between 20 and 80 m. The small accuracy and precision errors indicate that the solar algorithm is reasonably accurate and stable in retrieving mean effective sizes.

Accuracy of Mean Effective Size (daytime)

Precision of Mean Effective Size

Figure 41. Accuracy (top) and Precision (bottom) of Retrieved Effective Particle Size from the Cirrus Solar Algorithm for US Standard Atmosphere based on the 0.672-1.61μm Correlation, Sensor at Nadir.

Accuracy of Mean Effective Size

Precision of Mean Effective Size

Figure 42. Accuracy (top) and Precision (bottom) of Retrieved Effective Particle Size from the Cirrus Solar Algorithm for US Standard Atmosphere based on the 0.672-2.25μm Correlation, Sensor at Nadir.

Accuracy of Mean Effective Size

Precision of Mean Effective Size

Figure 43. Accuracy (top) and Precision (bottom) of Retrieved Effective Particle Size from the Cirrus Solar Algorithm for US Standard Atmosphere based on the 0.672-1.61μm Correlation, Sensor pointing Off-Nadir.

Accuracy of mean effective size

Precision -Optical depth, US Standard Atmosphere, ice cloud, solar, edge-of-scan
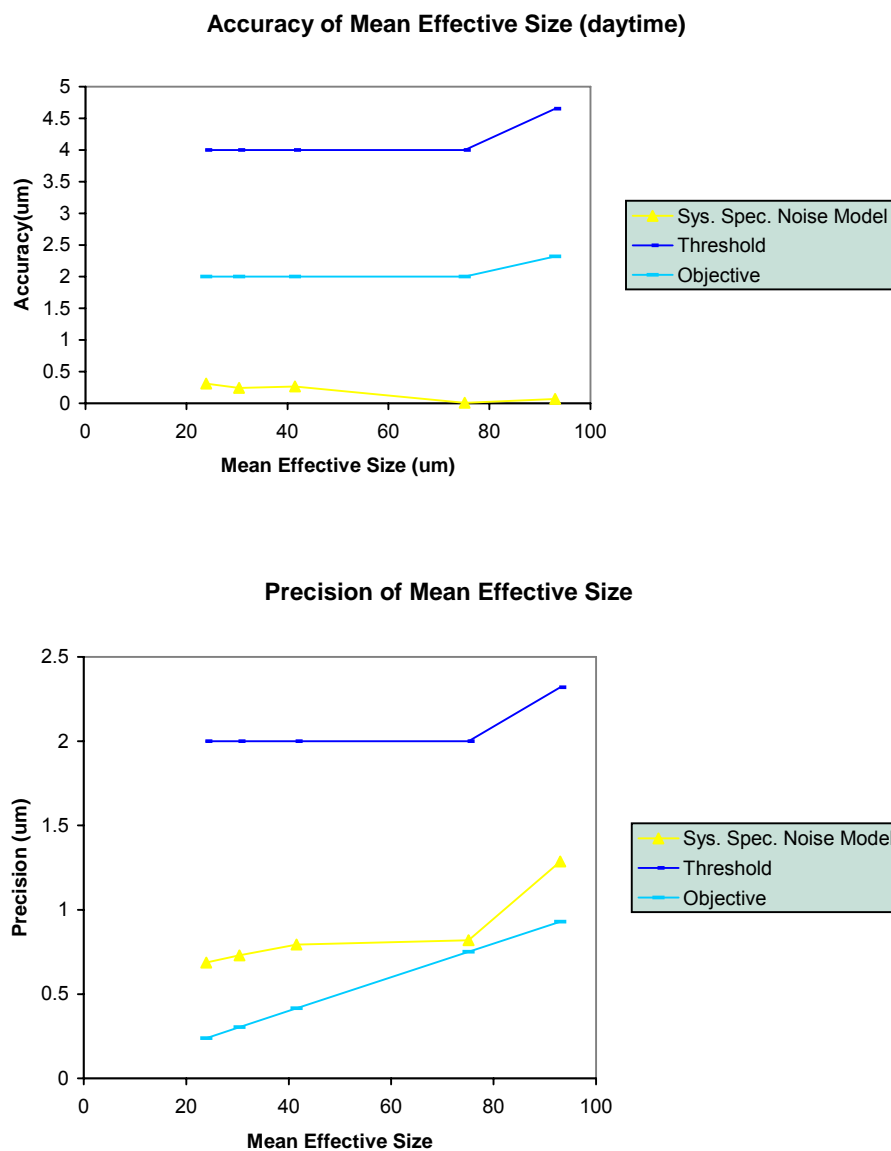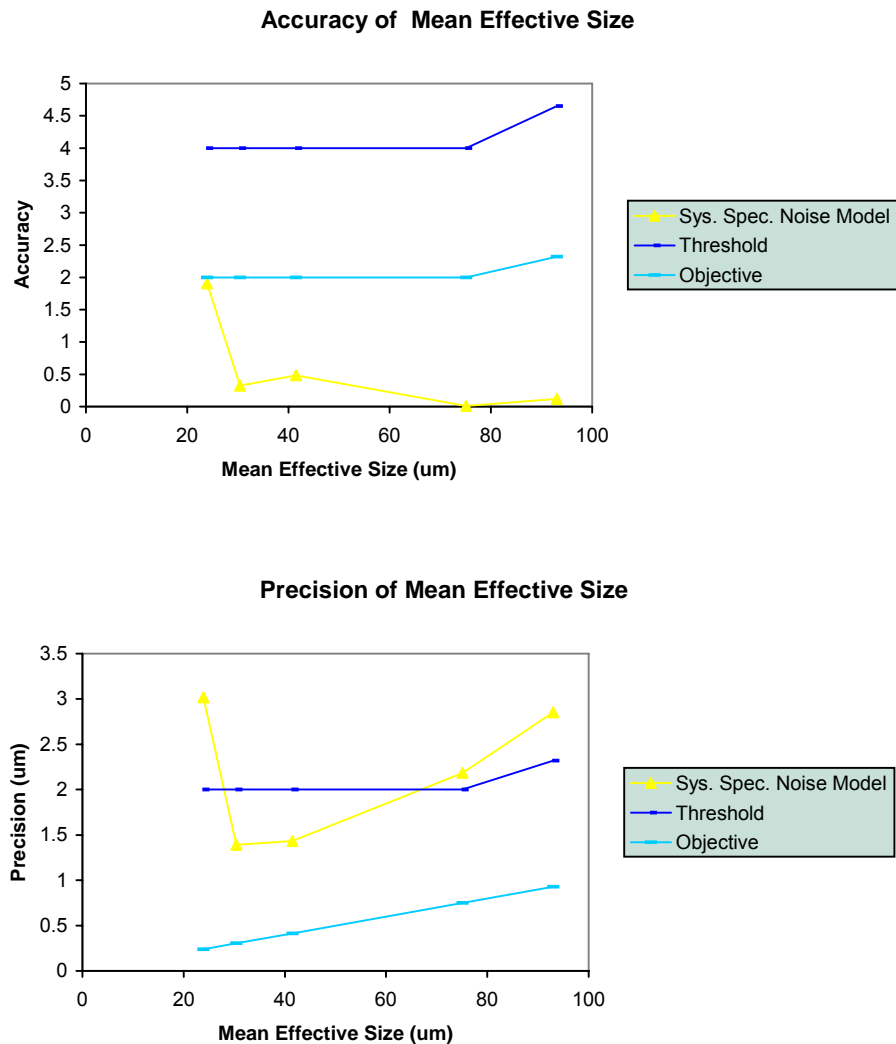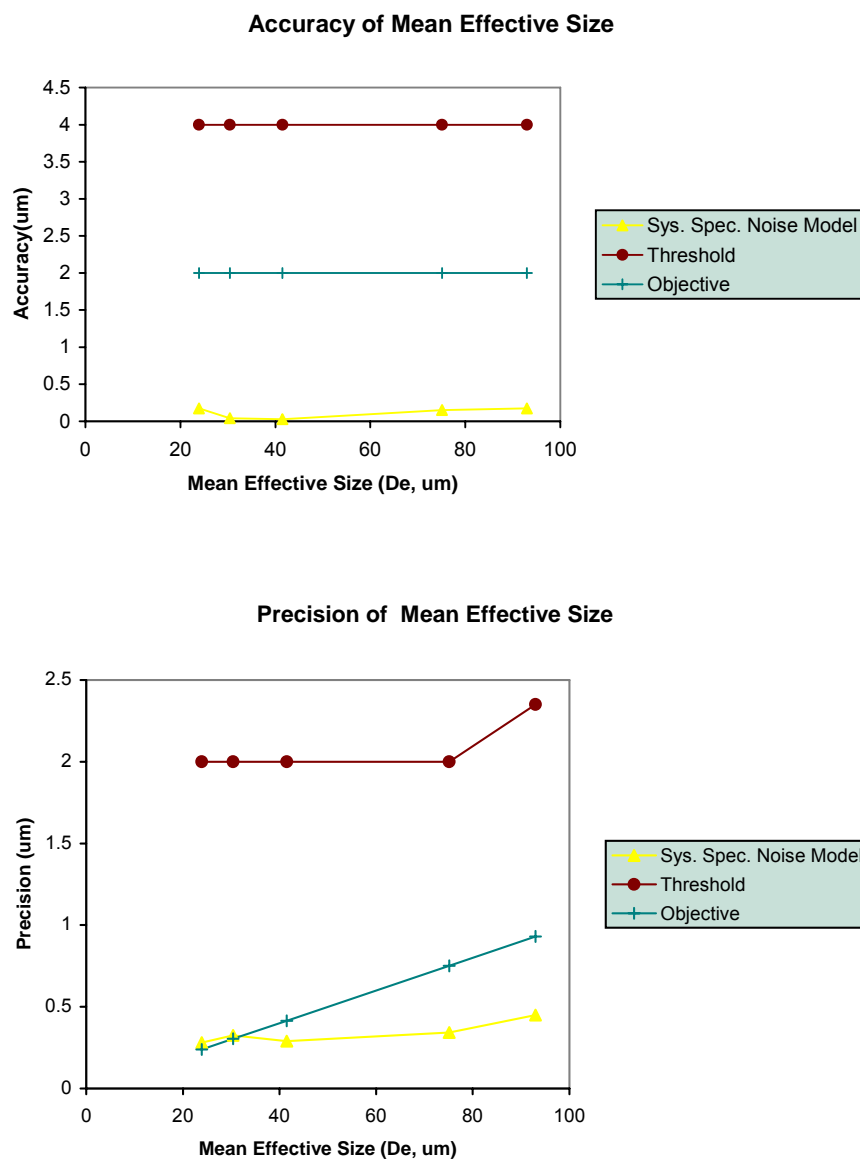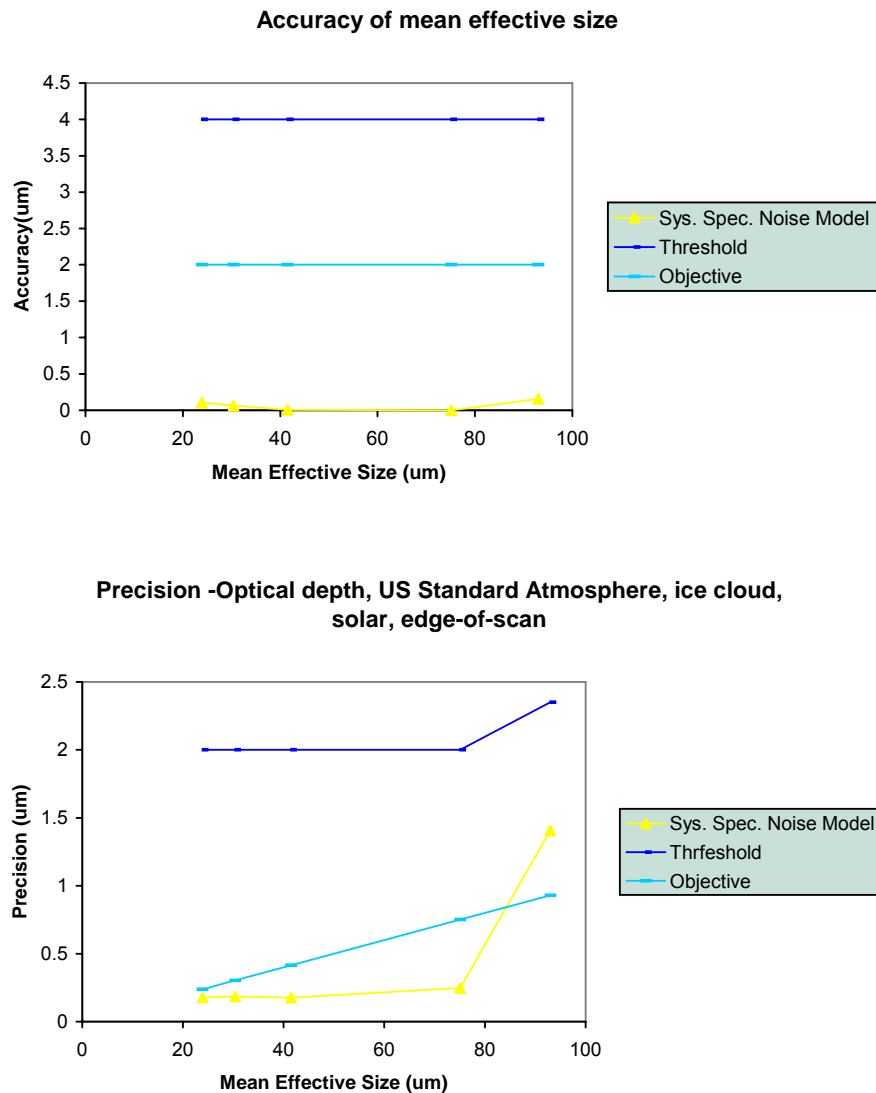

Figure 44. Accuracy (top) and Precision (bottom) of Retrieved Effective Particle Size from the Cirrus Solar Algorithm for US Standard Atmosphere based on the 0.672-1.61µm Correlation, Sensor at Edge-of-Scan.

Cirrus Cloud in Tropical Atmosphere, Sensor at Nadir

Figure 45 shows the accuracy and precision of retrieved mean effective size as a function of mean effective size. These results are based on retrieval combinations of all possible optical depths (0 to 10) and mean effective sizes (20 to 100μm). Two lines denote threshold (greater of 10 percent or 4μm) and objective (greater of 5 percent or 2μm) values. The accuracy of retrieved mean effective sizes meets both the threshold and objective requirements for the range of mean effective sizes. The accuracy error increases somewhat with larger particle sizes. The precision of retrieved mean effective sizes meets the threshold requirement for the full range of mean effective sizes. The precision of retrieved mean effective sizes meets the objective requirement for mean effective sizes between 40 and 100 m. The small accuracy and precision errors indicate that the solar algorithm is reasonably accurate and stable in retrieving mean effective sizes.

Cirrus Cloud in Sub-Arctic Atmosphere, Sensor at Nadir

Figure 46 shows the accuracy and precision of retrieved mean effective size as a function of mean effective size. These results are based on retrieval combinations of all possible optical depths (0 to 10) and mean effective sizes (20 to 100μm). Two lines denote threshold (greater of 10 percent or 4μm) and objective (greater of 5 percent or 2μm) values. The accuracy of retrieved mean effective size meets both the threshold and objective requirements for the range of mean effective sizes. The accuracy is about the same magnitude across the range of mean effective size. The precision of retrieved mean effective size meets both the threshold and objective requirements for the full range of mean effective sizes. The small accuracy and precision errors indicate that the solar algorithm is reasonably accurate and stable in retrieving mean effective sizes.

Cirrus Cloud in Desert Atmosphere, Sensor at Nadir

Figure 47 shows the accuracy and precision of retrieved mean effective size as a function of mean effective size. These results are based on retrieval combinations of all possible optical depths (0 to 10) and mean effective sizes (20 to 100μm). Two lines denote threshold (greater of 10 percent or 4μm) and objective (greater of 5 percent or 2μm) values. The accuracy of retrieved mean effective sizes meets both the threshold and objective requirements for the range of mean effective size. The accuracy is about the same magnitude across the range of mean effective size. The precision of retrieved mean effective sizes meets the threshold requirement for the full range of mean effective sizes. The precision of retrieved mean effective sizes meets the objective requirement for mean effective sizes between 40 and 100 m. The small accuracy and precision errors indicate that the solar algorithm is reasonably accurate and stable in retrieving mean effective sizes.

Accuracy of r(eff) for Ice Cloud at Nadir for a Tropical Atmosphere

Precision of r(eff) for Daytime Ice Cloud at Nadir for a Tropical Atmosphere

Figure 45. Accuracy (top) and Precision (bottom) of Retrieved Effective Particle Size from the Cirrus Solar Algorithm for Tropical Atmosphere based on the 0.672-1.61μm Correlation, Sensor at Nadir.

Accuracy of Mean Effective Size (Subarctic, Solar Ice Cloud, Nadir)

Precision of Mean Effective Size (Subarctic, Solar Ice Cloud, Nadir)

Figure 46. Accuracy (top) and Precision (bottom) of Retrieved Effective Particle Size from the Cirrus Solar Algorithm for Sub-Arctic Atmosphere based on the 1.2-1.61μm Correlation, Sensor at Nadir.

**Accuracy of Mean Effective Size (Desert, US Standard Atm.,
Solar Ice Cloud, Nadir)**

**Precision of Mean Effective Size (Desert, US Standard Atm.,
Solar Ice Cloud, Nadir)**

**Figure 47. Accuracy (top) and Precision (bottom) of Retrieved Effective Particle Size
from the Cirrus Solar Algorithm for Desert Atmosphere based on the 0.672-1.61μm
Correlation, Sensor at Nadir.**

Water Cloud in US Standard Atmosphere, Sensor at Nadir

Figure 48 shows the accuracy and precision of retrieved droplet effective radius as functions
of droplet effective radius. These results are based on retrieval combinations of all possible
optical depths (0 to 64) and mean effective sizes (4 to 30μm). For accuracy, the horizontal
lines denote threshold (greater of 10 percent or 4μm) and objective (greater of 5 percent or

2μm) values. The accuracy of retrieved droplet effective radius meets both the threshold and objective requirements for the range of droplet effective radius. For precision, the horizontal line denotes threshold (greater of 5 percent or 2μm), and the sloped line denotes objective (2 percent). The precision of retrieved droplet effective radius meets the threshold requirement for the full range of droplet effective radius. The small accuracy and precision errors indicate that the solar algorithm is reasonably accurate and stable in retrieving droplet effective radius.

Accuracy of r(eff) for Water Cloud at Nadir

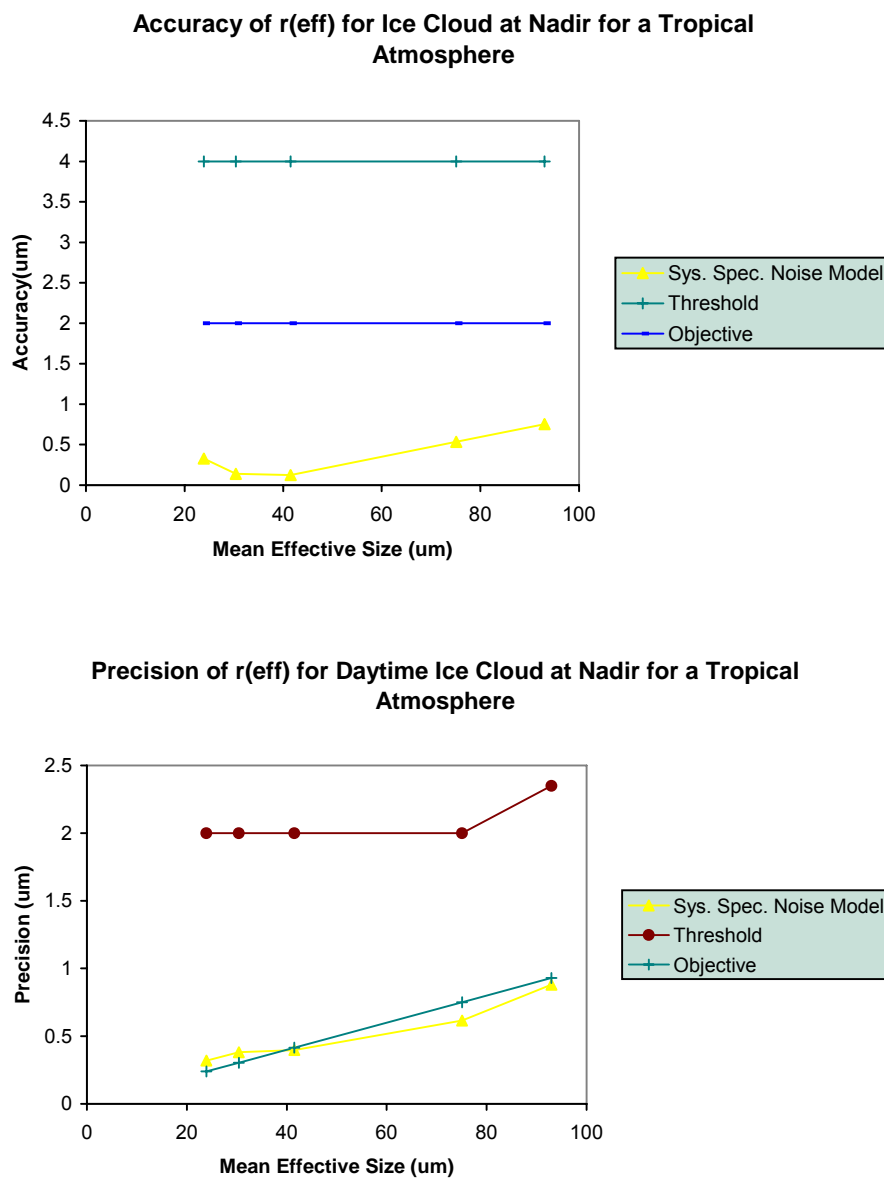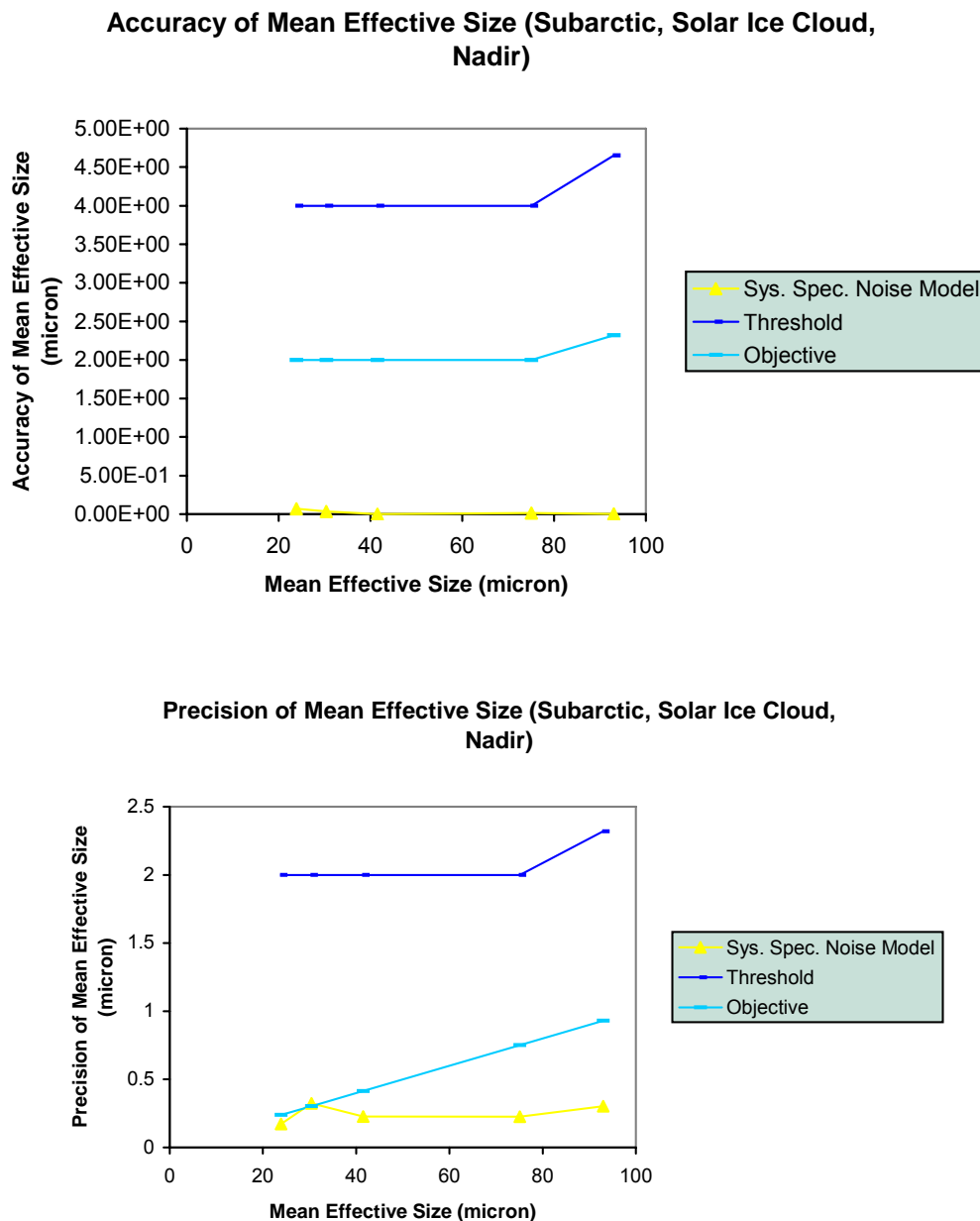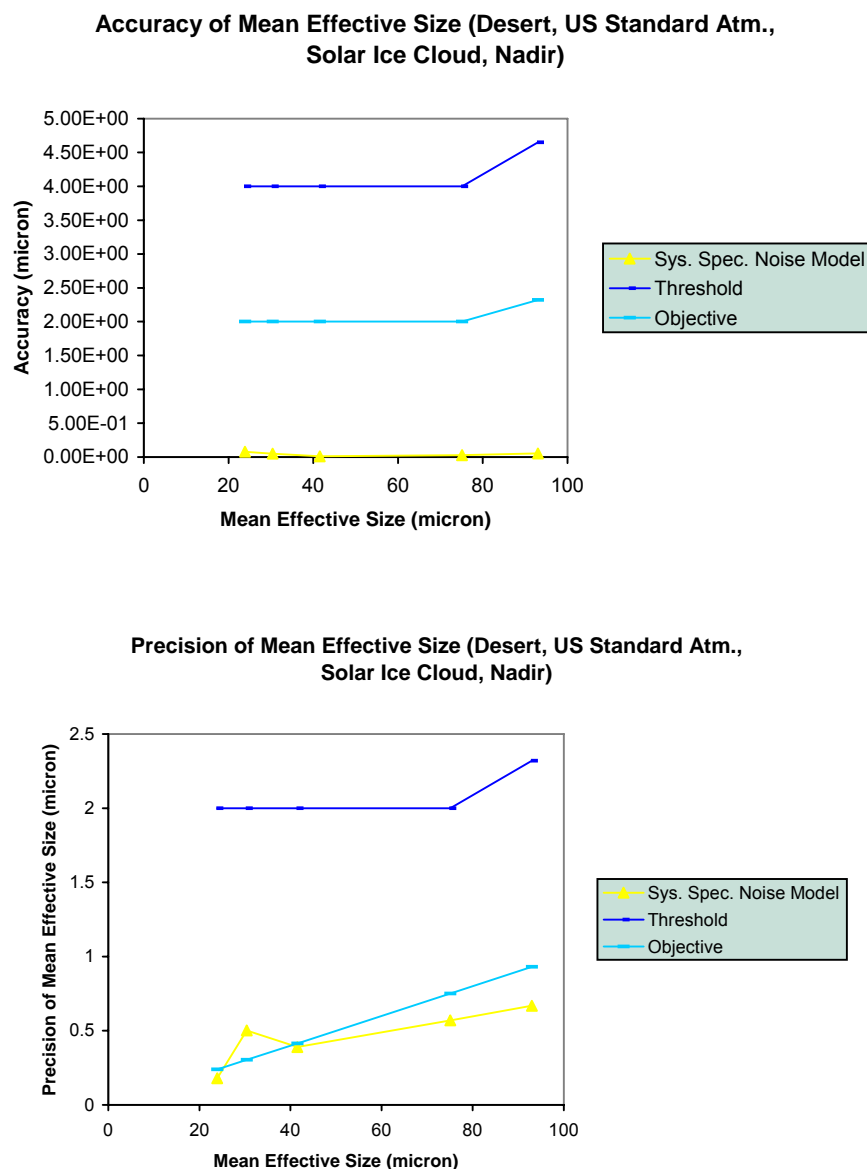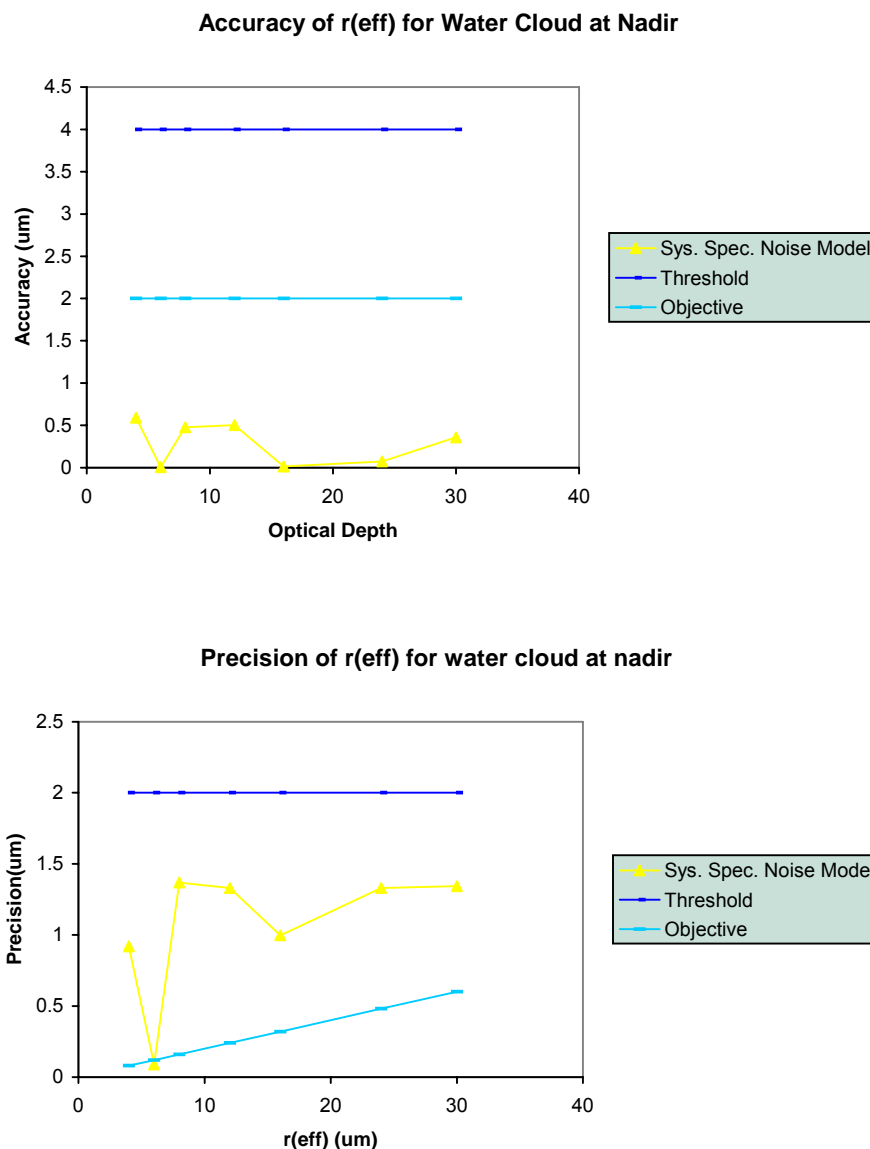**Precision of r(eff) for water cloud at nadir**

Figure 48. Accuracy (top) and Precision (bottom) of Retrieved Effective Particle Size from the Water Cloud Solar Algorithm for US Standard Atmosphere based on the 0.672-1.61μm Correlation, Sensor at Nadir.

3.5.1.2   **Nighttime**
Results

Cirrus Cloud in US Standard Atmosphere, Sensor at Nadir

Figure 49 shows the accuracy of retrieved mean effective ice crystal sizes from the nighttime IR algorithm as a function of optical depth for three mean effective sizes (23.9, 41.5 and 93μm. Horizontal lines denote threshold (greater of 10 percent or 4 μm) and objective (greater of 5 percent or 2μm) values. The accuracy of the retrieved mean effective ice crystal size for D_e=23.9μm meets the threshold and objective requirements for optical depths up to 7 and 5 respectively. The accuracy of the retrieved mean effective ice crystal size for D_e=41.5μm meets the threshold and objective requirements for optical depths up to 5 and 3 respectively. The accuracy of the retrieved mean effective ice crystal size for D_e=93μm meets the threshold requirement for optical depths up to 3. The accuracy does not meet the threshold for optical depths larger than 6, mainly due to the indirect effects of the exponential relationship between the IR emissivity and the optical depth. As the emissivity approaches unity, small errors in the retrieved emissivity will be amplified in the retrieved optical depth, and thus the accuracy of the retrieved mean effective size, which depends on the accuracy of the retrieved optical depth, is affected. On the other hand, as the emissivity approaches zero, errors in the retrieved cloud-top temperature increase. Therefore, the accuracy of the retrieved mean effective size, which depends on the accuracy of the retrieved cloud temperature, becomes worse for smaller optical depths. Moreover, the range of optical depths for which the threshold and objective requirements are met becomes smaller for larger ice crystal mean effective size. This is because as the mean effective size increases, the sensitivity of 3.7μm radiance to mean effective size decreases. Figure 50 shows the precision of retrieved mean effective ice crystal sizes from the nighttime IR algorithm as a function of optical depth for two mean effective sizes (23.9 and 41.5μm). The horizontal lines denote threshold (greater of 5 percent or 2 μm) and objective (2 percent) values. The precision of the retrieved mean effective ice crystal size for D_e=23.9μm meets the threshold and objective requirements for optical depths between 1 and 7, and between 5 and 7, respectively. The precision of the retrieved mean effective ice crystal size for D_e=41.5μm meets the threshold for optical depths between 2 and 7.

Cirrus Cloud in US Standard Atmosphere with Sensor pointing Off-Nadir

Figure 51 shows the accuracy of retrieved mean effective size from the nighttime IR algorithm as a function of optical depth for three mean effective sizes (23.9, 41.5 and 93μm). The horizontal lines denote threshold (greater of 10 percent or 4μm) and objective (greater of 5 percent or 2μm) values. The accuracy of the retrieved mean effective ice crystal size for D_e = 23.9μm meets the threshold and objective requirements for optical depths less than 10 and between 1 and 5, respectively. The accuracy of the retrieved mean effective ice crystal size for D_e = 41.5μm meets the threshold and objective requirements for optical depths up to 4 and 3, respectively. Accuracy meets the threshold requirement for D_e=93μm and optical depths between 0.5 and 2. As the emissivity approaches unity, small errors in the retrieved emissivity will be amplified in the retrieved optical depth, and thus the accuracy of the

retrieved mean effective size, which depends on the accuracy of the retrieved optical depth, is also amplified. On the other hand, as the emissivity approaches zero, errors in the retrieved cloud-top temperature increases. Therefore, the uncertainty of the retrieved mean effective size, which depends on the accuracy of the retrieved cloud temperature, becomes larger for smaller optical depths. Moreover, the range of optical depths for which the threshold and objective requirements are met becomes smaller for larger ice crystal mean effective size. This is because as the mean effective size increases, the sensitivity of $3.7\mu m$ radiance to mean effective size decreases. Figure 52 shows the precision of retrieved mean effective ice crystal sizes from the nighttime IR algorithm as a function of optical depth for two mean effective sizes (23.9 and $41.5\mu m$). The horizontal lines denote threshold (greater of 5 percent or $2\mu m$) and objective (2 percent) values. The precision of the retrieved mean effective ice crystal size for D_e=23.9μm meets the threshold requirement for optical depths between 1 and 10. The precision of the retrieved mean effective ice crystal size for D_e=41.5μm meets the threshold for optical depths between 1 and 8. Precision errors generally decrease with increasing optical depth.

Cirrus Cloud in US Standard Atmosphere with Sensor at Edge-of-Scan

Figure 53 shows the accuracy of retrieved mean effective size from the nighttime IR algorithm as a function of optical depth for three mean effective sizes (23.9, 41.5 and $93\mu m$). The horizontal lines denote threshold (greater of 10 percent or $4\mu m$) and objective (greater of 5 percent or $2\mu m$) values. The accuracy of the retrieved mean effective ice crystal size for D_e=23.9μm meets the threshold and objective requirements for optical depths from 1 to 10. The accuracy of the retrieved mean effective ice crystal size for D_e=41.5μm meets the threshold requirements for optical depths between 1 and 8. As the emissivity approaches unity, small errors in the retrieved emissivity will be amplified in the retrieved optical depth, and thus the accuracy of the retrieved mean effective size, which depends on the accuracy of the retrieved optical depth, is also amplified. On the other hand, as the emissivity approaches zero, errors in the retrieved cloud-top temperature increase. Therefore, the uncertainty of the retrieved mean effective size, which depends on the accuracy of the retrieved cloud temperature, becomes larger for smaller optical depths. Moreover, the range of optical depths for which the threshold and objective requirements are met becomes smaller for larger ice crystal mean effective size. This is because as the mean effective size increases, the sensitivity of $3.7\mu m$ radiance to mean effective size decreases. Figure 54 shows the precision of retrieved mean effective ice crystal sizes from the nighttime IR algorithm as a function of optical depth for two mean effective sizes (23.9 and $41.5\mu m$). The horizontal lines denote threshold (greater of 5 percent or $2\mu m$) and objective (2 percent) values. The precision of the retrieved mean effective ice crystal size for D_e=23.9μm meets the threshold requirement for optical depths between 1 and 6. The precision of the retrieved mean effective ice crystal size for D_e=41.5μm meets the threshold for optical depths between 0.5 and 4. Precision errors generally decrease with increasing optical depth.

Cirrus Cloud in Tropical Atmosphere, Sensor at Nadir

Figure 55 shows the accuracy of retrieved mean effective size from the nighttime IR algorithm as a function of optical depth for three mean effective sizes (23.9, 41.5 and 93μm). The horizontal lines denote threshold (greater of 10 percent or 4μm) and objective (greater of 5 percent or 2μm) values. The accuracy of the retrieved mean effective ice crystal size for D_e=23.9μm meets the threshold and objective requirements for optical depths up to 10. The accuracy of the retrieved mean effective ice crystal size for D_e=41.5μm also meets the threshold and objective requirements for optical depths up to 10. The accuracy of the retrieved mean effective ice crystal size for D_e=93μm meets the threshold and objective requirements for optical depths up to 6. Accuracy error increases for larger optical depth, mainly due to the indirect effects of the exponential relationship between the IR emissivity and the optical depth. As the emissivity approaches unity, small errors in the retrieved emissivity will be amplified in the retrieved optical depth, and thus the accuracy of the retrieved mean effective size, which depends on the accuracy of the retrieved optical depth, is affected. On the other hand, as the emissivity approaches zero, errors in the retrieved cloud-top temperature increases. Therefore, the accuracy error of retrieved mean effective size, which depends on the accuracy of the retrieved cloud temperature, becomes larger for smaller optical depths. Moreover, the range of optical depths for which the threshold and objective requirements are met becomes smaller for larger ice crystal mean effective size. This is because as the mean effective size increases, the sensitivity of 3.7μm radiance to mean effective size decreases. Accuracy for the tropical atmosphere is better than that for the US Standard Atmosphere, because the radiances are more sensitive to the cloud temperature and optical depth.

Figure 56 shows the precision of retrieved mean effective ice crystal sizes from the nighttime IR algorithm as a function of optical depth for one size (41.5μm). The horizontal lines denote threshold (greater of 5 percent or 2μm) and objective (2 percent) values. The precision of the retrieved mean effective ice crystal size for D_e=41.5μm meets the threshold for optical depths between 1 and 8. Precision error is minimized for the 2-6 optical depth range. This is possibly because for intermediate optical depth, the precision error for cloud temperature and for optical depth are both small, leading to smaller precision errors.

Water Cloud in US Standard Atmosphere, Sensor at Nadir

Figure 57 shows the accuracy and precision of retrieved droplet effective radius size from the nighttime IR algorithm as a function of optical depth for the no-noise case. These results are based on retrievals of combinations of effective droplet radii between 2 and 12μm. The straight line denotes threshold (greater of 10 percent or 4 m). The accuracy of the retrieved mean effective radius meets the threshold requirement for optical depths up to 8. For optically thick clouds, the IR emissivity approaches one, so that a small error in the retrieved emissivity can lead to a large error in optical depth. The precision of retrieved mean effective radius meets the threshold (greater of 5 percent or 2 m) requirement for optical depths up to 6. Precision becomes less satisfactory for larger optical depths, because of a lack of emissivity sensitivity toward optical depth.

3.5.1.3
Recommendations

- For daytime retrievals, the VIIRS noise model is generally suitable for retrieving cloud effective particle size using the 0.672 and 1.61μm channels.

- For nighttime retrievals using the IR algorithm, the VIIRS noise model is generally suitable for retrieving cloud effective particle size using the 3.7 and 10.7625μm channels.

Figure 49. Accuracy of Retrieved Effective Particle Size from the Cirrus Cloud IR Algorithm for US Standard Atmosphere for D_e=23.9μm (top), 41.5μm (middle) and 93μm (bottom), Sensor at Nadir.

Precision of Mean Effective Size for De = 23.9 um

Precision of Mean Effective Size for De = 41.5 um

Figure 50. Precision of Retrieved Effective Particle Size from the Cirrus Cloud IR Algorithm for US Standard Atmosphere for D_e=23.9μm (top) and 41.5μm (bottom), Sensor at Nadir.

Accuracy of Mean Effective Size for De=23.9um

Accuracy of Mean Effective Size for De=41.5 um

Accuracy of Mean Effective Size for De=93um

Figure 51. Accuracy of Retrieved Effective Particle Size from the Cirrus Cloud IR Algorithm for US Standard Atmosphere for D_e=23.9μm (top), 41.5μm (middle) and 93μm (bottom), Sensor pointing Off-Nadir.

Precision of Mean Effective Size for De = 23.9um

Precision of Mean Effective Size for De = 41.5um

Figure 52. Precision of Retrieved Effective Particle Size from the Cirrus Cloud IR Algorithm for US Standard Atmosphere for D_e=23.9μm (top) and 41.5μm (bottom), Sensor pointing Off-Nadir.

**Accuracy of Cirrus Mean Effective Size from IR Algorithm
for Mid-latitude Edge-of-Scan Scene (De=23.9um)**

**Accuracy of Cirrus Cloud Mean Effective Size from IR Algorithm
for Mid-latitude Edge-of-Scan Scene (De=41.5um)**
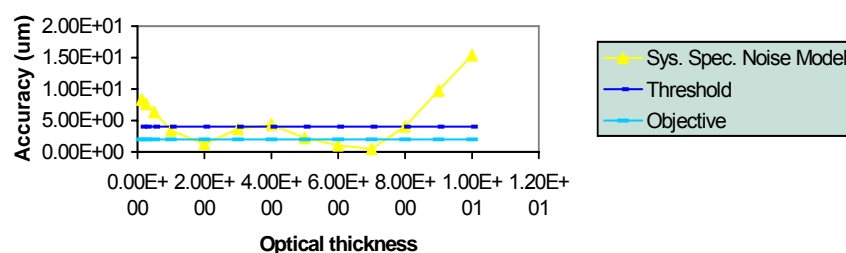
**Figure 53. Accuracy of Retrieved Effective Particle Size from the Cirrus Cloud IR Algorithm for US Standard Atmosphere for D_e=23.9μm (top) and 41.5μm (bottom), Sensor at
Edge-of-Scan.**

**Precision of Cirrus Cloud Mean Effective Size from Nighttime
IR Algorithm for a Mid-latitude Edge-of-scan Scene (De =
23.9um)**
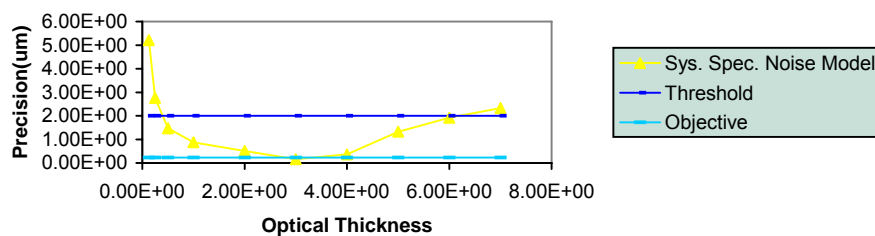
**Precision of Cirrus Cloud Mean Effective Size from IR
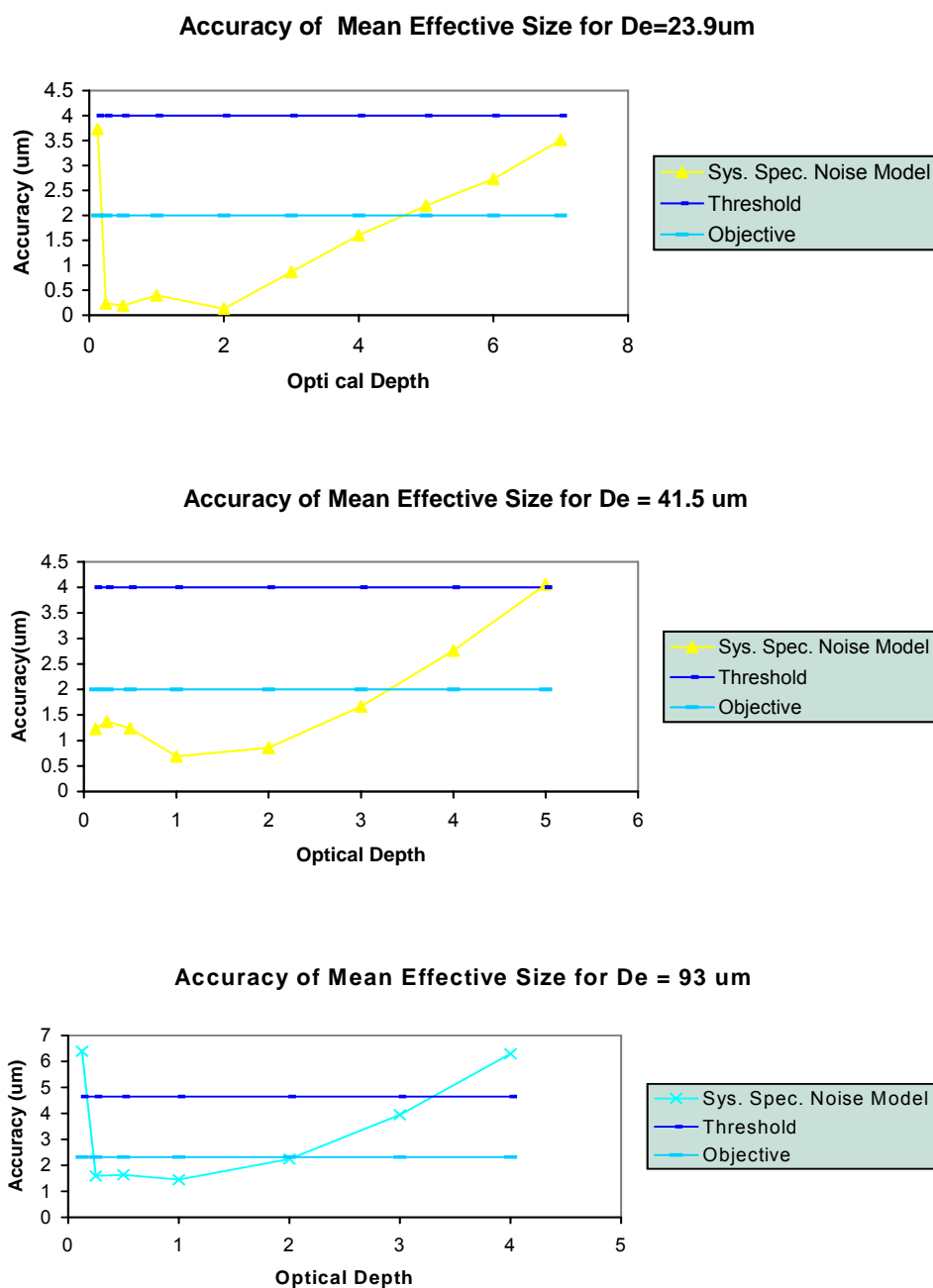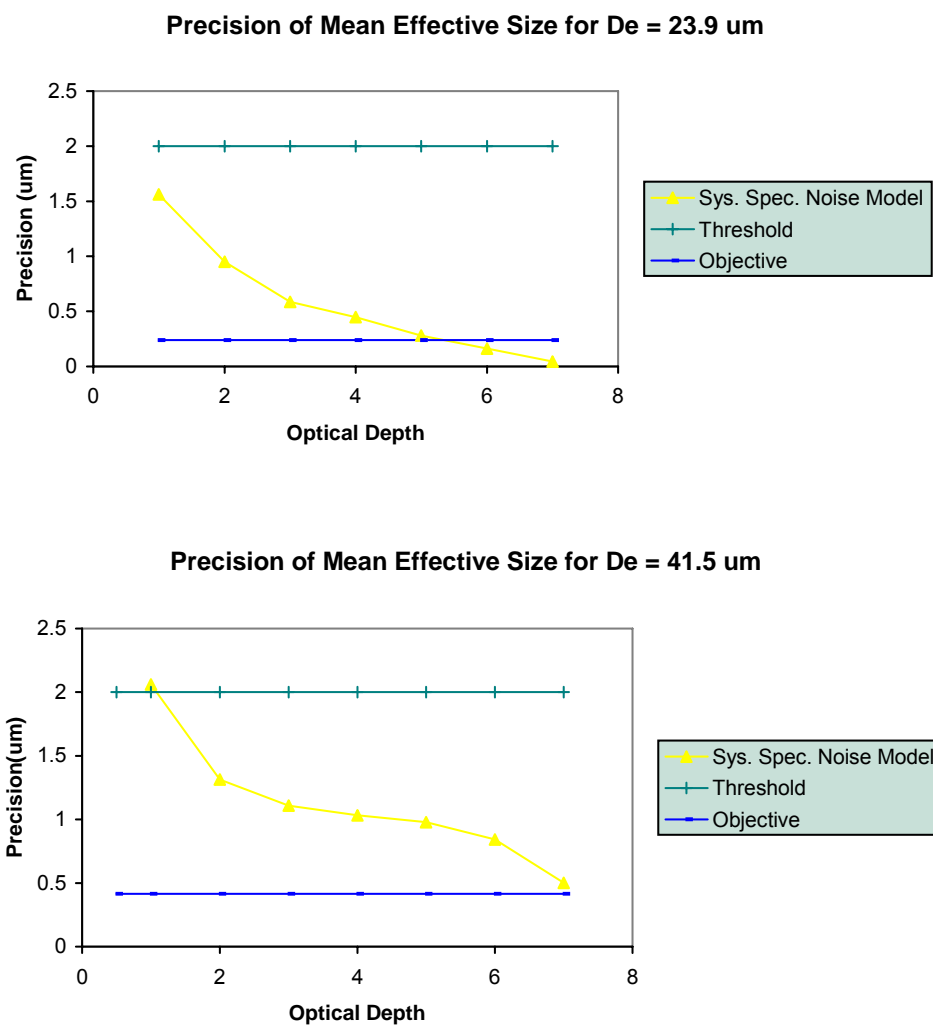Algorithm for Mid-latitude Edge-of-Scan Scene (De=41.5um)**
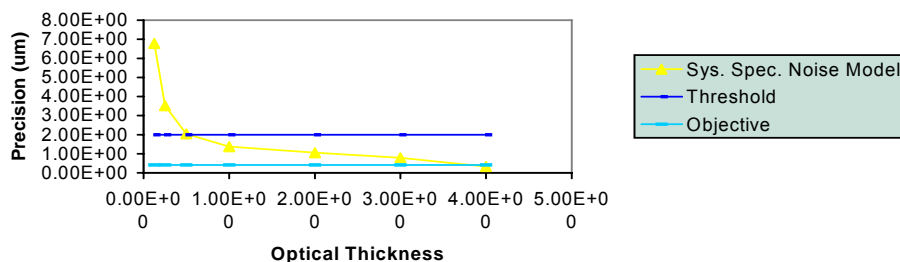
**Figure 54. Precision of Retrieved Effective Particle Size from the Cirrus Cloud IR
Algorithm for US Standard Atmosphere for D_e=23.9μm (top) and 41.5μm (bottom),
Sensor at
Edge-of-Scan.**

Accuracy ofMean Effective Size (De=23.9um)

Accuracy of Mean Effective Size (De=41.5um)
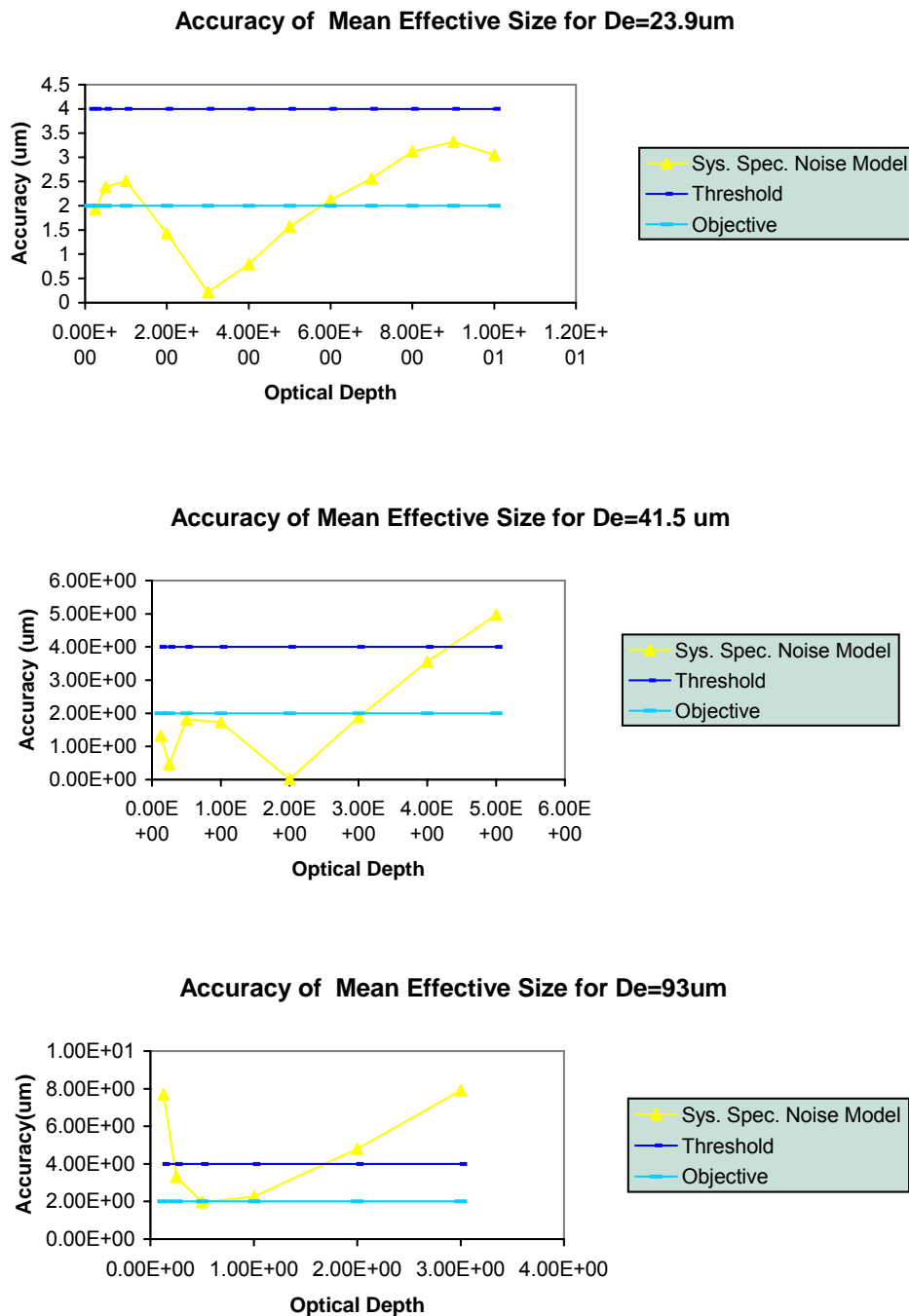
Accuracy of Mean Effective Size (De=93 um)
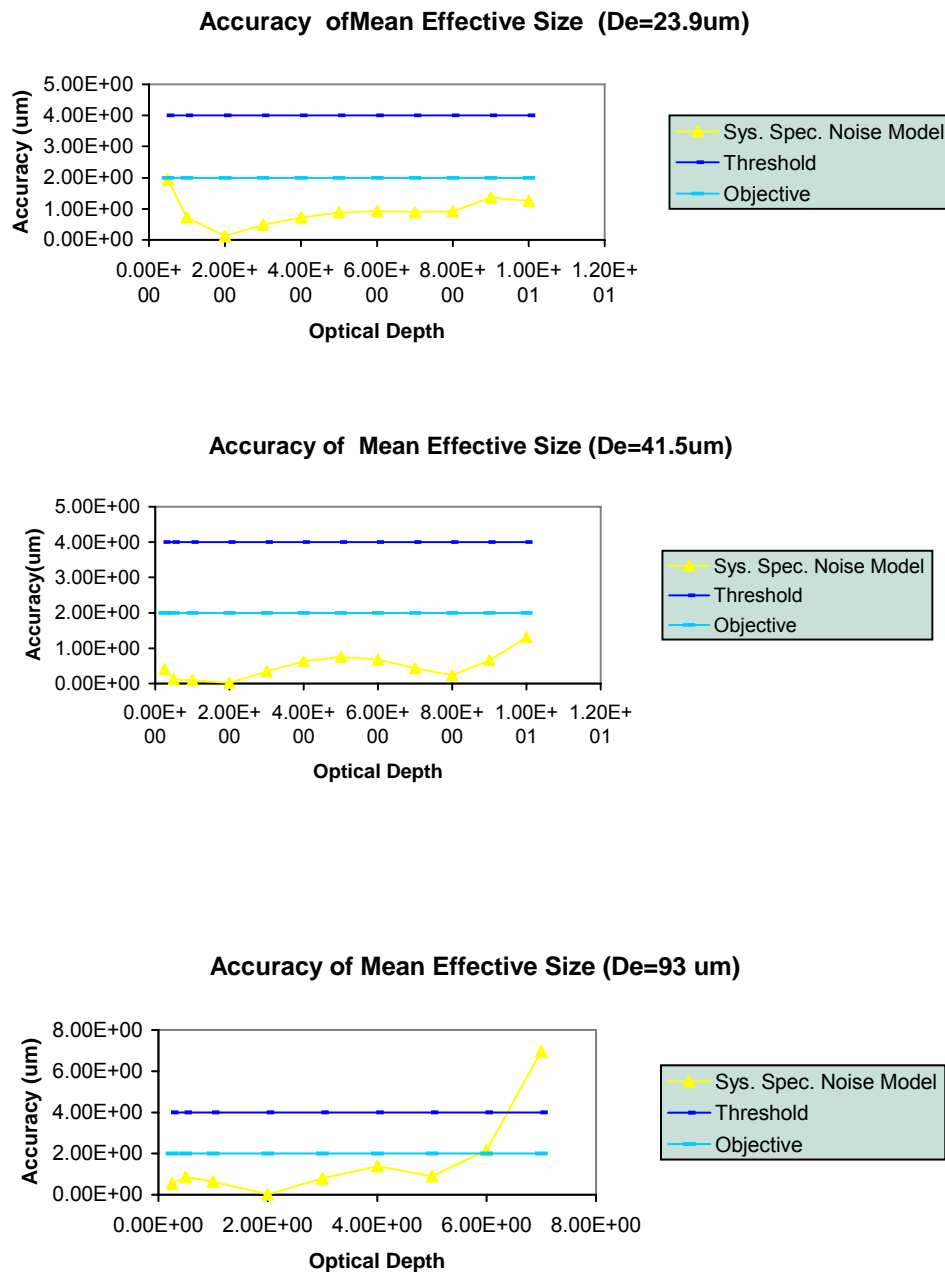
Figure 55. Accuracy of Retrieval Effective Particle Size for the Cirrus Cloud IR Algorithm for Tropical Atmosphere for D_e=23.9μm (top), 41.5μm (middle) and 93μm (bottom), Sensor at Nadir.
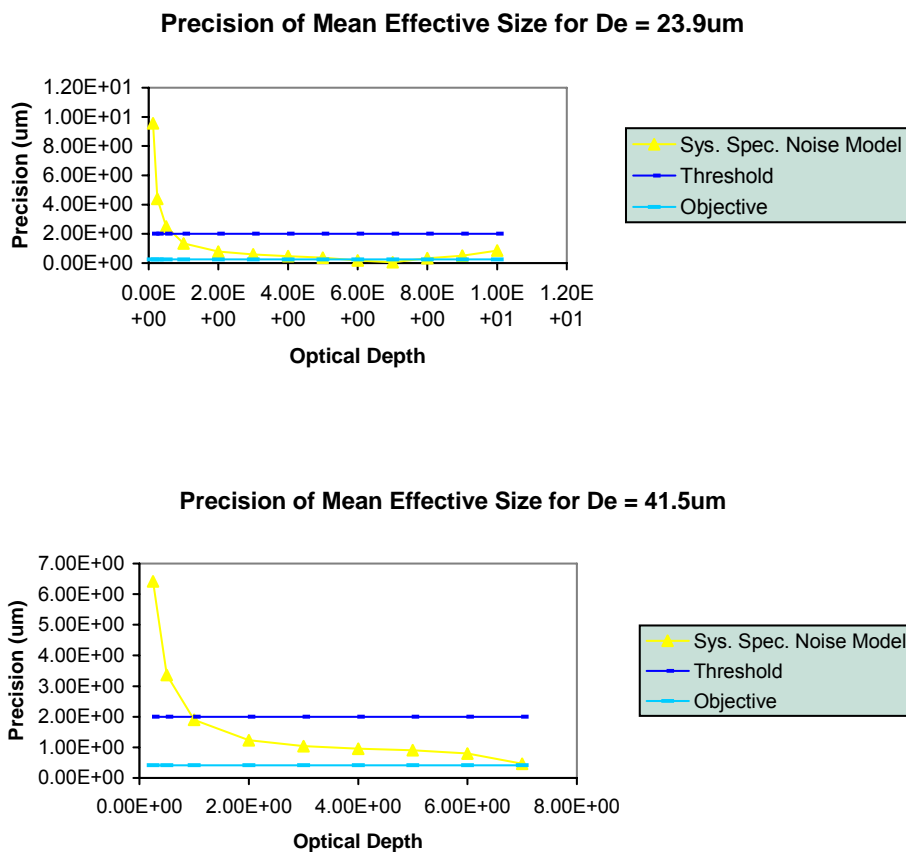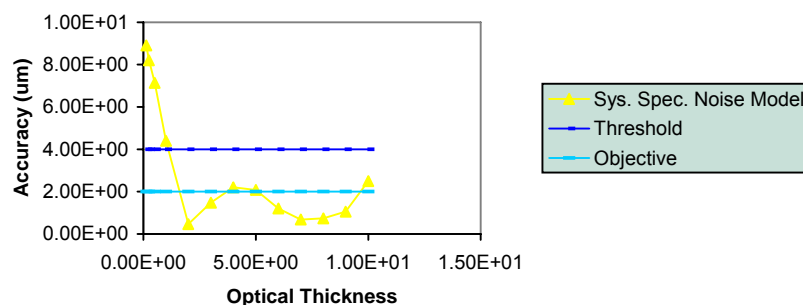
Precision o Mean Effective Size (De = 41.5um)
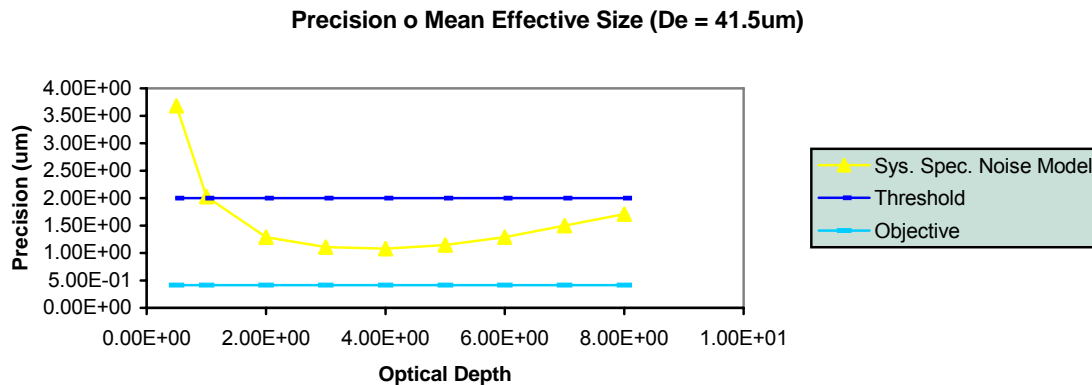
Figure 56. Precision of Retrieved Effective Particle Size from the Cirrus Cloud IR Algorithm for Tropical Atmosphere for D_e=41.5μm, Sensor at Nadir.

Accuracy of Nighttime IR Water EPS

Precision of Nighttime IR Water EPS
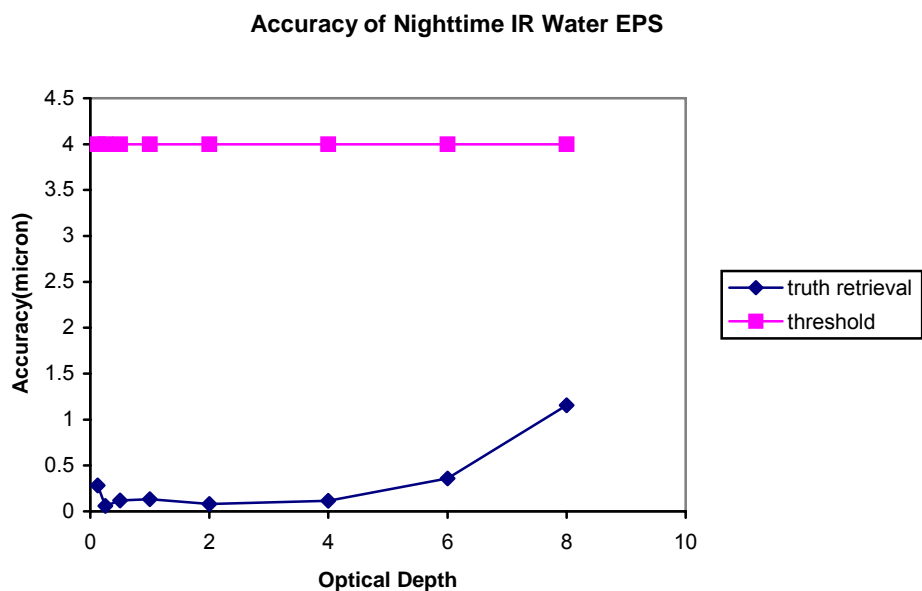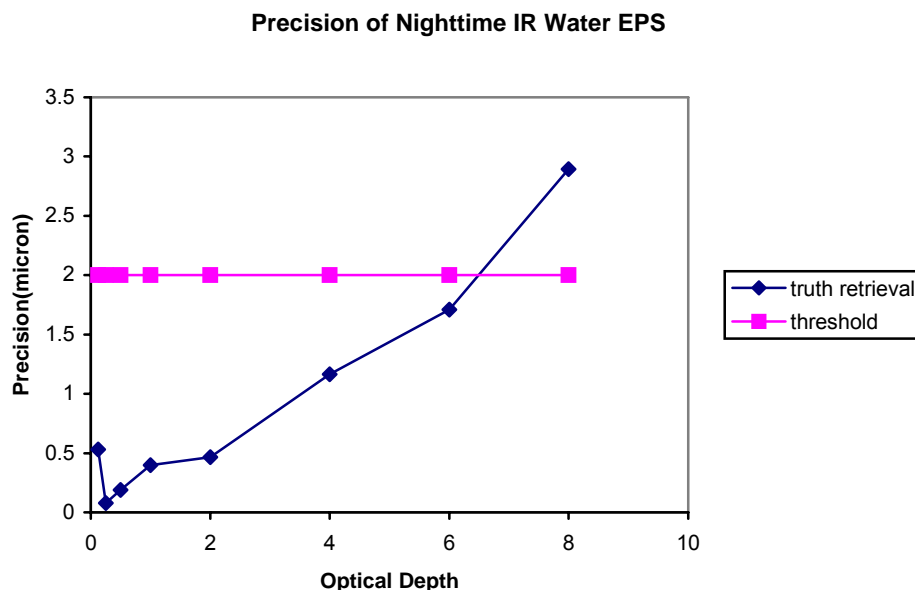
Figure 57. Accuracy (top) and Precision (bottom) of Retrieved Effective Particle Size from the IR Algorithm for Water Cloud, US Standard Atmosphere, No-Noise Retrievals, Sensor at Nadir.

3.5.2 Error Budget Studies

3.5.2.1 Algorithm Specific Errors in the Cloud Module

Algorithm specific errors, otherwise referred to as "intrinsic errors", for the cloud modules are discussed below. We define intrinsic errors as errors internal to the algorithms, related to algorithm assumptions or simplifications. Table 8.2-1 of the Error Budget Document gives various intrinsic error sources and their impacts on the retrievals. At this time, only truth retrieval errors are considered. Most of the other intrinsic errors have not been included in the EBs.

3.5.2.2 Input Error Sources

There are a number of input parameters to the cloud algorithms. We have attempted to quantify the impact of errors in input data sources on retrieval accuracy. Our approach has been to develop partial derivatives that quantify the change in a metric value (e.g., accuracy) to a small perturbation in the input parameter. These partial derivatives are then multiplied by a "standard error", which captures the anticipated rms error in that input parameter. The

product of the partial derivative with the standard error gives an estimate of an input parameter's contribution to the error budget for a given EDR. These error budgets have been developed by applying the retrieval algorithms to scenes. In general, these scenes cover approximately a 100km x 100km area. The spatial distribution of clouds within the area is determined through the use of TASC's Cloud Scene Simulation Model (CSSM). Processing of CSSM data yields a 2-D distribution of visible cloud optical thickness at 0.1km spatial resolution for a cloud layer. We assert an atmospheric scenario which includes sensor geometry, surface characteristics, atmospheric profiles, cloud base height, cloud top height and effective particle size. These atmospheric characteristics are used to develop LUTs for the scenario of VIIRS channel radiances as a function of cloud effective particle size and optical depth. The LUTs are used to create radiance images for the scene for each VIIRS channel used by the cloud algorithms, by associating a radiance value from the LUT with the optical depth value associated with each 0.1km data point. The 0.1km data are aggregated to the VIIRS pixel size. Perturbations to radiances, such as BBR, MTF, geolocation and calibration are applied to the 0.1km prior to aggregation. Perturbations to scenario parameters are affected by re-computing the radiance LUTs. The perturbed radiances are then applied to the scene. The unperturbed radiances are used to develop so-called truth retrievals. The retrievals using the perturbed radiances are used to compute SRD metrics and the partial derivatives.

Table 7.3-1 of the Error Budget Document provides a general list of input parameters used by the cloud algorithms. A given retrieval algorithm may not use all input parameters. The input parameters are divided into three groups: surface parameters, atmospheric profiles and EDRs and SDRs.

3.5.2.3 Sensor Error Sources

Several attributes of the sensor were assumed throughout the cloud EDR EBs. These are listed below:

- Sensor Noise Model: 3
- MTF Model: 5
- Band-to-Band Registration (BBR): 0.2 pixel shift
- Geolocation: 0.2 pixel shift
- Absolute Radiometric Calibration (ARA): 0.4% IR channels (down to a temperature of 270K; errors become larger for low temperatures), 2% solar channels
- Pixel sizes: nadir (753m, 1160m and 1600m)

The BBR and geolocation errors and MTF model were applied to the 0.1km radiance data prior to aggregation.

3.5.2.4   Specified and Predicted Performance

The Error Budgets for EPS are divided into four areas consistent with the specification and with the four algorithms used to produce this EDR: daytime water cloud, daytime ice cloud, nighttime ice cloud and nighttime water cloud.   The specifications and predicted performances based on Error Budget Analyses for these four cloud types are provided in Section 6.6.3 of the Error Budget Document (Raytheon Document Y3249.V3) and in Ou *et al.* (2003).

3.6 PRACTICAL CONSIDERATIONS

3.6.1 Numerical Computation Considerations

The retrieval algorithms shall be convertible into operational code that is compatible with a 20 minute maximum processing time. This maximum processing time is allocated not only to the cloud retrieval, but also to the retrieval of other VIIRS EDRs. The estimated processing time of this retrieval system is given as follows. For off-line processing, the generation of radiance tables would take a few CPU hours for all the cloud-retrieval channels and for each scenario. For on-line processing, the solar algorithm (<1 millisecond per retrieval) will be faster than the IR algorithm (~10 times longer than the solar algorithm).

In regard to the data storage, the following storage estimates are based on the simulated VIIRS orbit information. The sensor scanning rate is assumed to be 0.677 sec/scan. In one circular orbit (North Pole to North Pole), there are 8900 scan lines. Thus the period of the sensor is 0.677 x 8900 = 6025 sec or 100.4 minutes. With 3000 pixels in each scan line, the total pixel number in one day's flight is 3000 x 8900 x 1440 (min/day) / 100.4 (min/orbit) ~3.8 x 10^8 pixels.

The cloud effective particle size has values ranging between 0 to 100μm for cirrus clouds, and between 0 to 50μm for water clouds (droplet effective radius). The parameter value can be scaled by 10 to achieve necessary accuracy. Thus, it takes 10 bits to store the integer part of the parameter. Thus the data storage required per day is approximately 3.8 x 10^8 pixels x 10 bits / pixel = 3.8 x 10^9 bits = 475 Mbytes.

The cloud optical depth has values ranging between 0 to 10 for cirrus clouds, and between 0 to 64 for water clouds. The parameter value can be scaled by 10 to achieve necessary accuracy. Thus, it takes 6 bits to store the integer part of the parameter. The data storage required per day is approximately 3.8 x 10^8 pixels x 6 bits / pixel = 2.28 x 10^9 bits = 285 Mbytes.

3.6.2 Programming and Procedural Considerations

For the solar retrieval algorithms, comprehensive LUTs of reflectances as functions of sun-sensor geometry, surface albedo, atmospheric sounding, cloud EPS and COT will be developed for retrieval of cloud properties. For IR retrieval algorithms, parameterization of

extinction ratio in terms of EPS and COT for all possible atmospheric conditions will be executed.

3.6.3 Quality Assessment and Diagnostics

The assessment of the quality of retrievals will fall into four categories: Sensor Parameters; Environmental Scenario; Cloud Scenario; and Ancillary Data. Experience gained through simulations, and eventually by validation, will be captured and used to assess the quality of retrievals and provide guidance to the users of these products in the form of data quality flags. A list of parameters or situations that may influence data quality follows.

- *Sensor Parameters.* The qualities of sensor data include:

  - Sensor noise.

  - Radiance calibration.

  - Geolocation.

  - MTF.

  - Band-to-Band registration.

- *Environmental Scenario.* Particulars of the environmental scenario that may affect retrieval accuracy include:

  - Values of Environmental Parameters.

  - Atmospheric inversion.

- *Cloud Scenario.* The qualities or values of other cloud parameters that may affect retrieval accuracy include:

  - Cloud optical depth.

  - Cloud effective particle size.

  - Existence of multi-layer clouds. Multi-layer clouds are difficult to identify and have an impact on radiance measurements. Therefore, they will affect retrievals when a single layer cloud is assumed in the radiative transfer analysis or retrieval algorithm.

  - Solar position. Solar position influences UCLA IR cirrus parameter retrievals during daytime.

- *Ancillary Data*

  - In general, the quality of ancillary data affects the quality of retrievals.

The assessment of the quality of the retrievals is communicated through a set of Quality Flags. The values of these flags indicate the quality of the retrieved results. These flags were selected based on input from the user communities. The details of these flags can also be found in the "NPPEDRPR_V1.7_A3.doc" at NGST Eroom :

https://collab2.st.northropgrumman.com/eRoom/npoess/SystemEngineering/0_a959b

In brief, the quality flags for Cloud Optical Properties IP can be summarized in Table 9-10 as follow:

Table 9. COP Quality Flag Specifications

Quality Flag – Byte 0	Bit Field	Description/Source	Note
qf_cop_set	0	Overall pixel level flag	1: cop quality flag is set; 0: not
qf_cot_ice	1	Ice cot out of bound Day: (0.1-10) Night: (0.5-10)	1: out of bound; 0: not
qf_cot_water	2	Water cot out of bound Day: (0.1-64) Night: (0.1-12)	1: out of bound; 0: not
qf_de_ice	3	ice eps out of bound (1-50 micron)	1: out of bound; 0: not
qf_de_water	4	Water eps out of bound (1-50 micron)	1: out of bound; 0: not
qf_phs	5-7	Cloud phase	COP_PHASE_NOT_EXE 0x0 COP_PHASE_CIRRUS 0x20 COP_PHASE_OPQ_ICE 0x40 COP_PHASE_WATER 0x60 COP_PHASE_MIXED 0x80 COP_PHASE_MUL_LYR 0xA0
qf_residual_day_water	0	Iteration convergence	1: convergent; 0: not
qf_residual_day_ice	1	Iteration convergence	1: convergent; 0: not
qf_excl_day_water	2	water cot > 1 at daytime	1: yes; 0: not
qf_excl_day_ice	3	ice cot > 1 at daytime	1: yes; 0: not
qf_excl_night_water	4	water cot > 1 at nighttime	1: yes; 0: not

qf_excl_night_ice	5	ice cot > 1 at nighttime	1: yes; 0: not
qf_excl_sunglint	6	sun glint region	1: in sunglint; 0: not
qf_cld_confidence	7	probably/confidently cloudy	1: yes; 0: not

Table 10. CTT Quality Flag Specifications

Quality Flag – Byte 0	Bit Field	Description/Source	Note
qf_ctt_water	0	water ctt out of bound (250-300 Kelvin)	1: out of bound; 0: not
qf_ctt_ice	1	Ice ctt out of bound (213-253 Kelvin)	1: out of bound; 0: not
qf_residual_night_water	2	IR ice ctt convergence	1: convergence; 0: not
qf_residual_night_ice	3	IR ice ctt convergence	1: convergence; 0: not
qf_residual_ir_day_ice	4	IR ice ctt convergence	1: convergence; 0: not

Table 11. Granule Quality Flags

Name	Type	Description/Source	Units/Range
qf_granuleQF_good	uint16	converged / retrieved-pixels in percent	Including one digit after decimal point
qf_granuleQF_degrade	uint16	(nonconverged + out of bound + sunglint) / retrieved-pixels in percent	Including one digit after decimal point

3.6.4 Exception Handling

Clear and cloud-edge pixels identified by the cloud mask will not be used for cloud retrievals. Pixels with corrupted data will be scanned and filtered out.

3.7 ALGORITHM VALIDATION

Although the above algorithm sensitivity studies have demonstrated the applicability of remote sensing methods to the determination of cloud optical and microphysical properties, more experimental studies are required in order to assess the robustness and accuracy of these methods when applied to measurements on a global scale. Validation efforts are required in order to assess these methods, since many factors affect the successful retrieval of these parameters when applied to real data in a realistic atmosphere (e.g., Ou *et al.*, 1995). The following is a list of available data for validation.

a. MODIS data
MODIS (Moderate Resolution Imagining Spectroradiometer) is a scanning spectro-radiometer on board the polar orbiting TERRA(EOS/AM-1) satellite which was launched in December 1999. It possesses 36 channels ranging from 0.41   m to 14.2   m. In accordance with cirrus detection and retrieval, the 0.64   m band (channel 1), 0.85   m band (channel 2), 1.24   m band (channel 5), 1.37   m band (channel 26), 1.64   m band (channel 6), 2.1   m band (channel 7), 11.0   m band (channel 31), 12.0   m band (channel 32) and the 13.6   m band (channel 34) will be used. Channels 1, 2, 5, 6 and 7 have 500m resolution while the others have 1 km resolution. Level 1-B data are presently available.

b. AVHRR data
The AVHRR (Advanced Very-High Resolution Radiometer) scanning radiometer exists on board the NOAA 10, 14 and 15 satellites collecting data from five channels: 0.6   m, 0.9   m, 3.   m, 10.   m and 12.   m.

c. ARM data
A vertically pointing 35GHz Doppler radar along with a multi-pulsed lidar is operational at the Southern Great Plains Atmospheric Radiation Measurement (SGP ARM) site located in northern Oklahoma. Backscattered radiation from the radar can resolve cloud information in the vertical direction up to a height of 20km. Three Intensive Observation Periods (IOP) were made in conjunction with the overpass of an AVHRR instrument and in-situ measurements from aircraft: April 2-22, 1997; September 15-October 4, 1997; and April 27-May 17, 1998. In addition, surface polarization diversity lidar measurements in the 1998 IOP were made. Future IOP's are expected to take place in coordination with MODIS overpasses.

d. Microphysical data
In order to obtain a realistic representation of the particle size and shape observed in natural ice clouds, the mean effective size must be obtained. This parameter can be thought of as the number density weighted volume of the ice crystals divided by their number density weighted perpendicular cross sections averaged over the entire vertical column. During the Cloud IOP's at the SGP ARM site, the University of North Dakota Citation and King Air

performed in-situ microphysical measurements. These data are essential in the computation of the LUTs and for the validation of values retrieved from satellite observations.

4.0 ASSUMPTIONS AND LIMITATIONS

4.1 ASSUMPTIONS

There are several assumptions involved in the theoretical development of retrieval algorithms for cloud effective particle size and optical depth:

- For the retrieval of ice cloud parameters, representative ice crystal size distributions are based on *in situ* observations obtained during field experiments over mid-latitude areas. Ice crystals are assumed to be randomly oriented, and the ice crystal habits considered are solid columns and plates.

- For the retrieval of water cloud parameters, a gamma function is assumed to be the typical droplet size distribution, with water droplets assumed to be spherical in shape.

- Radiative transfer within the cloud is assumed to be plane-parallel.

4.2 LIMITATIONS

There are also a few limitations of the current algorithms:

- The solar and IR algorithms are applicable to a single-layer cirrus or water cloud. Use of these algorithms with multi-layer clouds will result in larger error than that for single-layer clouds.

- These algorithms do not adequately address mixed phase clouds which occur frequently around the globe. In that, the algorithm treats mixed phase clouds as ice clouds.

- The IR algorithms do not address situations in which the clear radiance is less than the cloudy radiance, which is prevalent during polar winter.

5.0 REFERENCES

Ambartzumian, V.(1936). The effects of the absorption lines on the radiative equilibuium of the outer layers of the stars. *Publ. Obs. Astron*. Univ. Leningrad, 6, 7-18.

Anderson, G. P., R. H. Picard, and J. H. Chetwynd (1995). Proceedings of the 17th Annual Review Conference on Atmospheric Transmission Models. Special Report No. 274, Phillips Laboratory/Geophysics Directorate, MA. May 1995, 332 pp.

Arking, A. and J. D. Childs (1985). Retrieval of cloud cover parameter from multi-spectral satellite images. *J. Clim. Appl. Meteor.*, 23, 322-333.

Arking, A. and K. Grossman (1972). The influence of line shape and band structure on temperatures in planetary atmospheres. *J. Atmos. Sci.,* 29, 937-949.

Auer, A. H., Jr. and D. L. Veal (1970). The dimension of ice crystals in natural clouds. *J. Atmos. Sci.*, 27, 919-926.

Baum, B.A., D.P. Kratz, P. Yang, S. Ou, Y. Hu, P.F. Soulenand S.-C. Tsay (2000). Remote sensing of cloud properties using MODIS Airborne Simulator imagery during SUCCESS.I. Data and models. J. Geophys. Res., 105, 11,767-11,780.

Berk, A., L. S. Bernstein, and D. C. Robertson (1989). MODTRAN: A Moderate Resolution Model for LOWTRAN 7. Report AFGL-TR-89-0122 (Air Force Geophysics Laboratory), Hanscom AFB, MA 01731.

Chylek, P., P. Damiano, N. Kalyaniwalla, and E. P. Shettle (1995). Radiative properties of water clouds: Simple approximations. *Atmos. Res.,* 35, 139-156.

Clothiaux, E. E., *et al*. (1995). An evaluation of a 94-GHz radar for remote sensing of cloud properties. *J. Atmos. Oceanic Technol.,* 12, 201-229.

Coakley, J. A., and F. P. Bretherton (1982). Cloud cover from high-resolution scanner data: detecting and allowing for partially filled fields of view. *J. Geophys. Res*., 87, C7, 4917-4932.

Curran, R. J., H. L. Kyle, L. R. Blaine, J. Smith, and T. D. Clem (1981). Multichannel scanning radiometer for remote sensing cloud physical parameters. *Rev. Sci. Instrum.,* 52, 1546-1555.

d'Almeida, G. A., P. Koepke, and E. P. Shettle (1991). Atmospheric Aerosols, Global Climatology and Radiative Characteristics. A. Deepak Publishing, Hampton, VA., 561pp.

Fu, Q. and K. N. Liou (1992). On the correlated k-distribution method for radiative transfer in nonhomogeneous atmospheres. *J. Atmos. Sci.*, 49, 2139-2156.

Fu, Q. and K. N. Liou (1993). Parameterization of the radiative properties of cirrus clouds. *J. Atmos. Sci.*, 50, 2008-2025.

Hansen, J. E. and J. B. Pollack (1970). Near-infrared light scattering by terrestrial clouds. *J. Atmos. Sci.,* 27, 265-281.

Hansen, J. E., and L. D. Travis (1974). Light scattering in planetary atmospheres*. Space Sci. Rev.*, 16, 527-610.

Heymsfield, A. J. and C. M. R. Platt (1984). A parameterization of the particle size spectrum of ice clouds in terms of the ambient temperature and ice water content. *J. Atmos. Sci.,* 41, 846-855.

Isaacs, R. G., W.-C. Wang, R. D. Worsham, and S. Goldenberg (1986). Multiple scattering Treatment for use in the LOWTRAN and FASCODE models. Report AFGL-TR-88-0073 (Air Force Geophysics Laboratory), Hanscom AFB, MA 01731.

Isaacs, R. G., W.-C. Wang, R. D. Worsham, and S. Goldenberg (1987). Multiple scattering LOWTRAN and FASCODE models. *Appl. Opt.,* 26, 1272-1281.

King, M. D., W. P. Menzel, P. S. Grant, J. S. Myers, G. T. Arnold, S. E. Platnick, L. E. Gumley, S. C. Tsay, C. C. Moeller, M. Fitzgerald, K. S. Brown, and F. G. Osterwisch, (1996). Airborne scanning spectrometer for remote sensing of cloud, aerosol, water vapor and surface properties*, J. Atmos. Oceanic Technology*, 13, 777-794.

King, M. D., S.-C. Tsay, S. E. Platnick, M. Wang, and K. N. Liou, (1996). Cloud retrieval algorithms for modis: Optical thickness, effective particle radius, and thermodynamic phase. MODIS Algorithm Theoretical Basis Document, No. ATBD-MOD-05.

Kneizys, F. X., G. P. Anderson, E. P. Shettle, and Coauthors (1988). User's guide to LOWTRAN 7. Air Force Geophysics Lab., Hanscom Air Force Base, MA., 136 pp.

Kratz, D. P., (1995) The correlated k-distribution technique as applied to the AVHRR channels. *J. Quant. Spectrosc. Radiat.* Transfer, 53, 501-517.

Larsen, N. (1994). Improved multiple scattering computations in a moderate resolution radiative transfer model. Geophysical Institute Report, UAG-R-321, U of Alaska, Fairbank, 168pp.

Liou, K. N., S. C. Ou, Y. Takano, F. P. J. Valero, and T. P. Ackerman (1990). Remote sounding of the tropical cirrus cloud temperature and optical depth using 6.5 and 10.5 μm radiometers during STEP. *J. Appl. Meteor.*, 29, 715-726.

Liou, K. N. (1992). Radiation and cloud processes in the atmosphere: Theory, observation and modeling. Oxford University Press, 487 pp.

Liou, K. N. and Y. Takano (1994). Light scattering by nonspherical particles: Remote sensing and climatic implications. *Atmos. Res.*, 31, 271-298.

Liou, K. N., P. Yang, Y. Takano, K. Sassen, T. Charlock, and W. Arnott (1998). On the radiative properties of contrail cirrus. *Geophys. Res. Lett.*, 25, 1161-1164.

Minnis, P., D. P. Garber, D. F. Young, R. F. Arduini, and Y. Takano (1998). Paramerizations of reflectance and effective emittance for satellite remote sensing of cloud properties. *J. Atmos. Sci.*, 55, 3313-3339.

Nakajima, T. and M. D. King (1990). Determination of the optical thickness and effective particle radius of clouds from reflected solar radiation measurements. Part I: Theory. *J. Atmos. Sci.*, 47, 1878-1893.

Ou, S. C., K. N. Liou, W. M. Gooch, and Y. Takano (1993a). Remote sensing of cirrus cloud parameters using advanced very-high-resolution radiometer 3.7- and 10.9 μm channels. *Appl. Opt.*, 32, 2171-2180.

Ou, S. C., K. N. Liou, N. X. Rao, W. M. Gooch, and Y. Takano (1993b), Remote sounding of cirrus cloud parameters using AVHRR data. Final Report PL-TR-93-2117, Phillips Laboratory, Directorate of Geophysics, Air Force Materiel Command, Hanscom Air Force Base, MA, 01731-3010.

Ou, S. C., K. N. Liou, Y. Takano, N. X. Rao, Q. Fu, A. J. Heymsfield, L. M. Miloshevich, B. Baum, and S. A. Kinne (1995). Remote sounding of cirrus cloud optical depths and ice crystal sizes from AVHRR data: Verification using FIRE II IFO composite measurements. *J. Atmos. Sci.*, 52, 4143-4158.

Ou, S. C., K. N. Liou, and B. A. Baum (1996). Detection of multilayer cirrus cloud systems using AVHRR data: Verification based on FIRE II IFO composite measurements. *J. Appl. Meteor.*, 35, 177-191.

Ou, S. C., K. N. Liou, and T. R. Caudill (1998). Remote sounding of multilayer cirrus cloud systems using AVHRR data collected during FIRE II IFO. *J. Appl. Meteor.*, 37, 241-254.

Ou, S. C., Y. Takano, K. N. Liou, G. J. Higgins, A. George and R. L. Slonaker (2003). Remote sensing of cirrus cloud optical thickness and effective particle size for the National Polar-orbiting Operational Environmental Satellite System Visible/Infrared Imager Radiometer Suite: sensitivity to instrument noise and uncertainties in environmental parameters. *Appl. Opt.*, 42, 7202-7214.

Rayleigh, Lord (1918). Light scattering by atmospheric molecules. Phil. Mag., 35, 373-390.

Rao, N. X., S. C. Ou, and K. N. Liou (1995). Removal of the solar component in AVHRR 3.7-μm radiances for the retrieval of cirrus cloud parameters. *J. Appl. Meteor.,* 34, 481-499.

Revercomb, H. E., H. Bujis, H. B. Howell, D. D. LaPorte, W. L. Smith, and L. A. Sromovsky (1988). Radiometeric calibration of IR Fourier transform spectrometers: Solution to a problem with the High-spectral resolution Interferometer Sounder. *Appl. Opt.*, 27, 3210-3218.

Rolland, P., K. N. Liou, M. D. King, S. C. Tsay, and G. M. McFarquhar (2000). Remote sensing of optical and microphysical properties of cirrus clouds using MODIS channels: methodology and sensitivity to physical assumptions. *J. Geophys. Res.,* (in press).

Spinhirne, J. D., R. Boers and W. D. Hart (1989). Cloud top liquid water from lidar observations of marine stratocumulus. *J. Appl. Meteor.*, 28, 81-90.

Stamnes, K., S.-C. Tsay, W. Wiscombe, and K. Jayaweera (1988). Numerically stable algorithm for discrete-ordinate method radiative transfer in multiple scattering and emitting layered media. *Appl. Opt.,* 27, 2502-2509.

Szejwach, G. (1982). Determination of semi-transparent cirrus cloud temperature from infrared radiances : Application to METEOSAT. *J. Appl. Meteor.,* 21, 384-393.

Takano, Y. and K. N. Liou (1989). Solar radiative transfer in cirrus clouds. Parts I and II. *J. Atmos. Sci.*, 46, 3-19, 20-36.

Takano, Y. and K. N. Liou (1993). Transfer of polarized infrared radiation in optically anisotropic media: application to horizontally oriented ice crystals. *J. Opt. Soc. Am. A*, 10, 1243-1256.

Takano, Y. and K. N. Liou (1995). Radiative transfer in cirrus clouds. Part III: Light scattering by irregular ice crystals. *J. Atmos. Sci.*, 52, 818-837.

Takano, Y., K. N. Liou, and P. Minnis (1992). Effects of small ice crystals on cirrus infrared radiative properties. J. Atmos. Sci.,49, 1487-1493.

Thekaekara, M. P. (1976). Solar irradiance: total and spectral and its possible variations. *Appl. Opt.*, 15, 915-920.

Twomey, S. and T. Cocks (1982). Spectral reflectance of clouds in the near-infrared: Comparison of measurements and calculations. J. Meteor. Soc. Japan, 60, 583-592.

Twomey, S, and T. Cocks (1989). Remote sensing of cloud parameters from spectral reflectance in the near-infrared. Beitr. Phys. Atmos., 62, 172-179.

Yang, P. and K. N. Liou (1995). Light scattering by hexagonal ice crystals: comparison of finite-difference time domian and geometric optics models. *J. Opt. Soc. Am. A.*, 12, 162-176.

Yang, P. and K. N. Liou (1996a). Geometric-optics-integral-equation method for light scattering by nonspherical ice crystals. *Appl. Opt.*, 35, 6568-6584.

Yang, P. and K. N. Liou (1996b). Finite-difference time domain method for light scattering by small ice crystals in three-dimensional space. *J. Opt. Soc. Am. A*, 13, 2072-2085.

APPENDIX A. SYSTEM SPECIFICATION REQUIREMENTS

This Appendix describes the threshold and objective requirements for cloud effective particle size and optical depth. The following tables are adopted from the VIIRS System Specification Document.

Cloud Optical Thickness (IORD Name: Cloud Optical Depth/Transmissivity)

Cloud optical depth is defined as the extinction (scattering + absorption) vertical optical thickness of all cloud layers in a vertical column of the atmosphere. Optical thickness ( ) is related to transmittance (t) by t= exp (-). Optical thickness is wavelength dependent and is to be measured in at least two narrow bands centered at 450 nm (TBR) and 850 nm (TBR), with TBD nm bandwidth. Table A-1 shows the system specification requirement relevant to the retrieval of cloud optical depth.

Units: Dimensionless

Table A-1. System Specification for the Cloud Optical Thickness EDR.

Requirement Number	Parameter	Requirement
SSV0235	EDR CLOPTH Moderate HCS worst case:	25 km
SSV0236	EDR CLOPTH Fine HCS at nadir:	5 km
SSV0237	EDR CLOPTH Horizontal Reporting Interval:	HCS
SSV0238	EDR CLOPTH Horizontal Coverage:	Global
SSV0240	EDR CLOPTH Measurement Range day water cloud:	0.1 to 64 units of
SSV0241	EDR CLOPTH Measurement Range day ice cloud:	0.1 to 10 units of
SSV0242	EDR CLOPTH Measurement Range night ice cloud:	0.5 to 10 units of
SSV0244	EDR CLOPTH Moderate Measurement Accuracy day water cloud, OD ≤ 1:	0.28 units of
SSV0787	EDR CLOPTH Moderate Measurement Accuracy day ice cloud, OD ≤ 1:	0.08 units of
SSV0788	EDR CLOPTH Moderate Measurement Accuracy night ice cloud, OD ≤ 1:	0.16 units of
SSV0789	EDR CLOPTH Moderate Measurement Accuracy day water cloud, OD > 1:	10.00%
SSV0790	EDR CLOPTH Moderate Measurement Accuracy day ice cloud, OD > 1:	5.00%
SSV0791	EDR CLOPTH Moderate Measurement Accuracy night ice cloud, OD > 1:	10.00%
SSV0245	EDR CLOPTH Moderate Measurement Precision day water cloud, OD ≤ 1:	0.100 units of
SSV0793	EDR CLOPTH Moderate Measurement Precision day ice cloud, OD ≤ 1:	0.023 units of
SSV0794	EDR CLOPTH Moderate Measurement Precision night ice cloud, OD ≤ 1:	0.025 units of

SSV0795	EDR CLOPTH Moderate Measurement Precision day water cloud, OD > 1:	4.00%
SSV0796	EDR CLOPTH Moderate Measurement Precision day ice cloud, OD > 1:	3.00%
SSV0797	EDR CLOPTH Moderate Measurement Precision night ice cloud, OD > 1:	5.00%
SSV0246	EDR CLOPTH Fine Measurement Uncertainty day water cloud, OD ≤ 1:	0.30 units of
SSV0799	EDR CLOPTH Fine Measurement Uncertainty day ice cloud, OD ≤ 1:	0.10 units of
SSV0800	EDR CLOPTH Fine Measurement Uncertainty night ice cloud, OD ≤ 1:	0.16 units of
SSV0801	EDR CLOPTH Fine Measurement Uncertainty day water cloud, OD > 1:	10.00%
SSV0802	EDR CLOPTH Fine Measurement Uncertainty day ice cloud, OD > 1:	10.00%
SSV0803	EDR CLOPTH Fine Measurement Uncertainty night ice cloud, OD > 1:	10.00%
SSV0247	EDR CLOPTH Measurement Long Term Stability	2 %
SSV0249	EDR CLOPTH Swath Width	3000 km

Cloud Effective Particle Size

Effective cloud particle size is defined as the ratio of the third moment of the droplet size distribution to the second moment, averaged over a layer of air within a cloud. Table A-2 shows the system specification requirement relevant to the retrieval of cloud effective particle size.

Units: μm

Table A-2. System Specification for the Cloud Effective Particle Size EDR.

Requirement Number	Parameter	Requirement
SSV0217	EDR CLEFFP Moderate HCS worst case:	25 km
SSV0218	EDR CLEFFP Fine HCS at nadir:	5 km
SSV0219	EDR CLEFFP HRI:	HCS
SSV0221	EDR CLEFFP Vertical Reporting Interval	Up to 4 layers
SSV0222	EDR CLEFFP Horizontal Coverage	Global
SSV0223	EDR CLEFFP Vertical Coverage	0 to 20 km
SSV0224	EDR CLEFFP Measurement Range	0 to 50 μm
SSV0228	EDR CLEFFP Moderate Measurement Accuracy, day water cloud, OD ≤ 1:	5.5 μm
SSV0771	EDR CLEFFP Moderate Measurement Accuracy, day ice cloud, OD ≤ 1:	8 μm
SSV0772	EDR CLEFFP Measurement Accuracy, day water cloud, OD > 1:	2 μm
SSV0773	EDR CLEFFP Measurement Accuracy, day ice cloud, OD > 1:	3.5 μm
SSV0774	EDR CLEFFP Moderate Measurement Accuracy, night ice cloud, OD > 1:	4 μm
SSV0775	EDR CLEFFP Moderate Measurement Accuracy, night water cloud, OD > 1:	4 μm
SSV0229	EDR CLEFFP Moderate Measurement Precision, day water cloud, OD ≤ 1:	1 μm
SSV0776	EDR CLEFFP Moderate Measurement Precision, day ice cloud, OD ≤ 1:	1.5 μm
SSV0777	EDR CLEFFP Moderate Measurement Precision, day water cloud, OD > 1:	1 μm

SSV0778	EDR CLEFFP Moderate Measurement Precision, day ice cloud, OD > 1:	1.5 µm
SSV0779	EDR CLEFFP Moderate Measurement Precision, night ice cloud, OD > 1:	2 µm
SSV0780	EDR CLEFFP Moderate Measurement Precision, night water cloud, OD > 1:	2 µm
SSV0230	EDR CLEFFP Fine Measurement Uncertainty, day water cloud, OD ≤ 1:	5.5 µm
SSV0781	EDR CLEFFP Fine Measurement Uncertainty, day ice cloud, OD ≤ 1:	12 µm
SSV0782	EDR CLEFFP Fine Measurement Uncertainty, day water cloud, OD > 1:	2.5 µm
SSV0783	EDR CLEFFP Fine Measurement Uncertainty, day ice cloud, OD > 1:	4 µm
SSV0784	EDR CLEFFP Fine Measurement Uncertainty, night ice cloud, OD > 1:	4 µm
SSV0785	EDR CLEFFP Fine Measurement Uncertainty, night water cloud, OD > 1:	4 µm
SSV0231	EDR CLEFFP Measurement Long Term Stability	2 %
SSV0233	EDR CLEFFP Swath Width	3000 km

APPENDIX B. ITERATIVE MATCHING OF REFLECTANCE PAIRS

This section presents an iterative numerical method for the optimal matching of the computed and measured reflectance pair (0.672–1.61μm).

Let the reflectances $r(\lambda=0.672\mu m)$ be r_1, and $r(\lambda=1.61\mu m)$ be r_2. Also, let a series of D_e and τ values be chosen: D_{e1}, D_{e2}, …, D_{en}, …, D_{eN}, and τ_1, τ_2, …, τ_m, …, τ_M, where N and M are the total number of selected mean effective sizes and optical depths, respectively. The superscript numeral within the parentheses indicates iteration number. The superscript sign, "+" or "-", indicates computed reflectances greater or less than that measured, respectively. We denote the subscripts 'comp' and 'meas' as the computed and measured values, respectively. Thus, radiance tables of $r_{1comp}(n, m)$ and $r_{2comp}(n, m)$ for all combinations of (D_{en}, τ_m) are obtained from LBLE. We start by searching for the index $m^{(0)}$, so that:

$$r_1^{-(0)} < r_{1meas} \le r_1^{+(0)} \tag{B.1}$$

where:

$$r_1^{-(0)} = r_{1comp}(3, m^{(0)}) \quad ; \ r_1^{+(0)} = r_{1comp}(3, m^{(0)} + 1)$$

The D_e index, n, is set to 3 as an initial guess. The iteration will find the correct index regardless of the guess. A value near the middle of the index range saves computation for most cases. Once $m^{(0)}$ is determined, we obtain $\tau^{(0)}$ as:

$$\tau^{(0)} = \tau_{m^{(0)}} + \frac{\tau_{m^{(0)}+1} - \tau_{m^{(0)}}}{r_1^{+(0)} - r_1^{-(0)}}(r_{1meas,i} - r_1^{-(0)}) \tag{B.2}$$

Then by using the index $m^{(0)}$, we search for the index $n^{(0)}$, so that:

$$r_2^{-(0)} < r_{2meas} \le r_2^{+(0)}, \tag{B.3}$$

where:

$$r_2^{-(0)} = r_{2comp}(n^{(0)} + 1, m^{(0)}); \qquad r_2^{+(0)} = r_{2comp}\left(n^{(0)}, m^{(0)}\right)$$

With $n(0)$ determined, we obtain $D_e^{(0)}$ as:

$$D_e^{(0)} = D_{e,n^{(0)}} + \frac{D_{e,n^{(0)}+1} - D_{e,n^{(0)}}}{r_2^{-(0)} - r_2^{+(0)}}(r_{2meas,i} - r_2^{+(0)}) \tag{B.4}$$

We then go back and search for the index $m^{(1)}$, so that:

$$r_1^{-(1)} < r_{1meas} \le r_1^{+(1)} \tag{B.5}$$

where:

$$r_1^{-(1)} = r_{1comp}(n^{(0)}, m^{(1)}) + \frac{r_{1comp}(n^{(0)}+1, m^{(1)}) - r_{1comp}(n^{(0)}, m^{(1)})}{D_{e,n^{(0)}+1} - D_{e,n^{(0)}}}[D_e^{(0)} - D_{e,n^{(0)}}]$$

$$r_1^{+(1)} = r_{1comp}(n^{(0)}, m^{(1)}+1) + \frac{r_{1comp}(n^{(0)}+1, m^{(1)}+1) - r_{1comp}(n^{(0)}, m^{(1)}+1)}{D_{e,n^{(0)}+1} - D_{e,n^{(0)}}}[D_e^{(0)} - D_{e,n^{(0)}}]$$

Once $m^{(1)}$ is determined, we obtain $\tau^{(1)}$ as:

$$\tau^{(1)} = \tau_{m^{(1)}} + \frac{\tau_{m^{(1)}+1} - \tau_{m^{(1)}}}{r_1^{+(1)} - r_1^{-(1)}}(r_{1meas,i} - r_1^{-(1)}) \tag{B.6}$$

Then by using the index $m^{(1)}$, we search for the index $n^{(1)}$, so that:

$$r_2^{-(1)} < r_{2meas} \le r_2^{+(1)} \tag{B.7}$$

where:

$$r_2^{-(1)} = r_{2comp}(n^{(1)}+1, m^{(1)}) + \frac{r_{2comp}(n^{(1)}+1, m^{(1)}+1) - r_{2comp}(n^{(1)}+1, m^{(1)})}{\tau_{m^{(1)}+1} - \tau_{m^{(1)}}}[\tau^{(1)} - \tau_{m^{(1)}}]$$

$$r_2^{+(1)} = r_{2comp}(n^{(1)}, m^{(1)}) + \frac{r_{2comp}(n^{(1)}, m^{(1)}+1) - r_{2comp}(n^{(1)}, m^{(1)})}{\tau_{m^{(1)}+1} - \tau_{m^{(1)}}}[\tau^{(1)} - \tau_{m^{(1)}}]$$

With $n^{(1)}$ determined, we obtain $D_e^{(1)}$ as:

$$D_e^{(1)} = D_{e,n^{(1)}} + \frac{D_{e,n^{(1)}+1} - D_{e,n^{(1)}}}{r_2^{-(1)} - r_2^{+(1)}}(r_{2meas,i} - r_2^{+(1)}) \tag{B.8}$$

The iteration continues until convergence.

APPENDIX C. ESTIMATING AND SMOOTHING CLEAR RADIANCES FOR OVERCAST SCENES FOR IR RETRIEVALS

This section describes the scheme implemented in the algorithm to estimate clear radiances for overcast scenes (1 deg by 1 deg scene) and to smooth the clear radiance distribution. This scheme has been applied to AVHRR data over the North America continent, eastern Pacific, and western Atlantic Oceans and reasonable clear radiance maps have been generated (Ou et al. 1993b, Rao et al. 1995). To estimate clear radiances for overcast scenes, we specify clear radiances for these scenes using the values from neighboring boxes. To smooth the resulting clear radiance distribution, we use the principle of spatial coherence method.

The clear radiance should be larger than the cloudy radiance according to Equation 43, because the emissivity is less than 1 and the cloud temperature is usually lower than the surface temperature. Given that an overcast scene is identified based on VIIRS cloud mask results, we determine its clear radiances iteratively. We first examine its neighboring scenes to the east and to the west. If both neighboring scenes are partly cloudy, the clear radiances are determined to be the average of those for the two neighboring scenes. If only one of them is partly cloudy, the clear radiances for that scene are used. However, if both neighboring scenes are identified as overcast, then no assigning or averaging process is performed. The above procedures are repeated for each scan line (roughly corresponding to the east-west direction). A schematic description of this scheme for the determination of clear radiances for overcast scenes is shown in Fig. E1.

The above neighboring-scene technique may not produce reasonable values when contiguous scenes are filled with thick clouds without clear pixels. To smooth out the clear radiance map, we use the principle of the spatial coherence method (Coakley and Bretherton 1982) to detect anomalously low clear radiance values. In this method, a small array (say, 2 x 2) of adjacent pixels is taken as a unit, from which averages of the clear radiances for the four scenes and associated standard deviations are computed. Because the clear radiance map is expected to be smoother than the cloudy radiance map, the standard deviation of the array is expected to be small. This is particularly true over oceans. Standard deviations for arrays over land may be larger than over oceans due to the inhomogeneity of land surface radiative properties and terrain topography. If the clear radiance for any scene is lower than a prescribed threshold value, that scene is classified as abnormal. Otherwise, it is flagged as normal. The threshold value is specified as:

$$R_{ac} = <R_a> - \quad . \qquad\qquad . \tilde{.}!$$

where R_{ac} is the threshold value, $<R_a>$ the array-average of clear radiance, the associated standard deviation, and an empirical scale factor. The parameter determines the degree of smoothing. Larger values causes less scenes to be flagged as abnormal, and therefore the smoothing is minimal. Based on a trial-and-error process using AVHRR data over North America and its surrounding oceans, we found that = 1.3 for ocean and = 1.475 for land are adequate values to produce realistic clear radiance maps. If a scene is flagged as

abnormal, its clear radiances are re-placed with the array-average values. This process is repeated until no scene is flagged as abnormal.
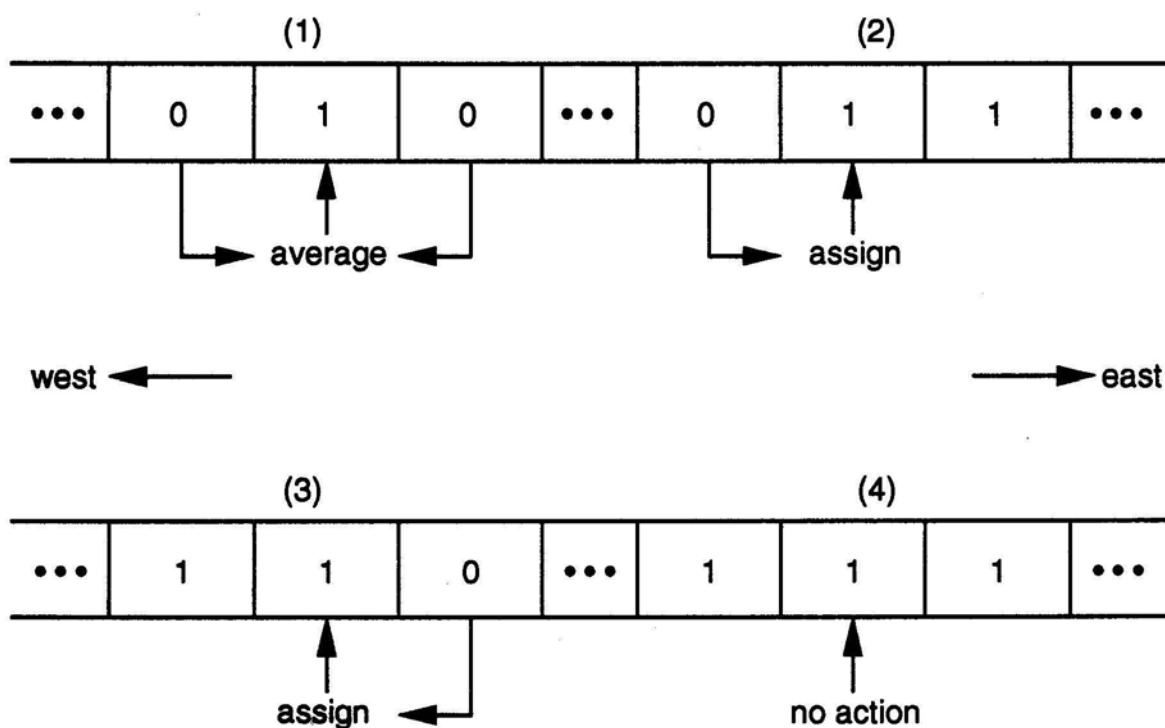
0 = partially cloudy or clear scene

1 = overcast scene

Figure E1. A schematic description of the determination of clear radiances for overcast scenes. The action taken in each case is explained as follows. (1) Both neighboring scenes are partially cloudy or clear. In this case, we take the average of the clear radiances for these scenes as the new value for the central overcast scene. (2) and (3) One of the neighboring scenes is partially cloudy or clear. In these cases, we assign the clear radiance for that scene to the central overcast scene. (4) None of the neighboring scenes is partially cloudy or clear. No action is taken in this case.